

Wright State University

CORE Scholar

[Browse all Theses and Dissertations](#)

[Theses and Dissertations](#)

2021

Development and Application of a Computational Modeling Scheme for Periodic Lattice Structures

Abdalsalam Fadeel
Wright State University

Follow this and additional works at: https://corescholar.libraries.wright.edu/etd_all



Part of the [Engineering Commons](#)

Repository Citation

Fadeel, Abdalsalam, "Development and Application of a Computational Modeling Scheme for Periodic Lattice Structures" (2021). *Browse all Theses and Dissertations*. 2493.

https://corescholar.libraries.wright.edu/etd_all/2493

This Dissertation is brought to you for free and open access by the Theses and Dissertations at CORE Scholar. It has been accepted for inclusion in Browse all Theses and Dissertations by an authorized administrator of CORE Scholar. For more information, please contact library-corescholar@wright.edu.

DEVELOPMENT AND APPLICATION OF A COMPUTATIONAL MODELING SCHEME FOR PERIODIC LATTICE STRUCTURES

A dissertation submitted in partial fulfillment of the
requirements for the degree of
Doctor of Philosophy

By

ABDALSALAM FADEEL

B.S., Omer Al Mukhtar University, Libya, 1999

M.M.S.E., Universiti Putra Malaysia, 2010

M.S.M.E., Wright State University, 2019

2021

Wright State University

WRIGHT STATE UNIVERSITY
GRADUATE SCHOOL

February 26, 2021

I HEREBY RECOMMEND THAT THE DISSERTATION PREPARED UNDER MY SUPERVISION BY Abdalsalam Fadeel ENTITLED Development and Application of a Computational Modeling Scheme for Periodic Lattice Structures. BE ACCEPTED IN PARTIAL FULFILLMENT OF THE REQUIREMENTS FOR THE DEGREE OF Doctor of Philosophy.

Ahsan Mian, Ph.D.
Dissertation Director

Brian Rigling, Ph.D.
Director, Ph.D. in Engineering Program

Barry Milligan, Ph.D.
Dean of the Graduate School

Committee on Final Examination

Ahsan Mian, Ph.D.

Raghavan Srinivasan, Ph.D.

Daniel Young, Ph.D.

Joy Gockel, Ph.D.

Golam Newaz, Ph.D.

Abstract

Fadeel, Abdalsalam. Ph.D., Engineering Ph.D. Program, Department of Mechanical Engineering, Wright State University, 2021. Development and Application of a Computational Modeling Scheme for Periodic Lattice Structures.

Sandwich structures are widely used for aerospace, marines and other applications due to their light-weight, strength, and strain energy absorption capability. The cores of the sandwich structure are typically fabricated by using high strength cellular materials such as aluminum and titanium alloys, or polymer foams, and honeycombs. Lattice cell structures (LCS) of different configurations such as body centered cubic (BCC), tetrahedron and pyramidal are being investigated as core material due to their design freedom and periodic nature. Due to the recent advent of additive manufacturing (AM), new research is being sought in the areas of designing and developing application-specific LCS configurations. However, experimental investigation of LCS is costly in time and materials. Therefore, in this dissertation, finite element models are developed using ABAQUS and validated according to previous experimental results to design application-specific LCS. First, an efficient and user-friendly tool was developed and this tool is called the Lattice Structure Designer (LSD). The LSD was developed from ABAQUS GUI and using Python scripting. This tool can be used to create the lattice models, define the materials, define the geometry, define the boundary conditions, apply loads, and submit the jobs to perform the computational analysis. The same tool can be used to access the database files and calculate any additional outputs. This ABAQUS plug-in has effectively helped to capture the responses beyond the plasticity levels and capture the failure mechanisms of the lattice structure. In this research, three types of lattices such as body

centered cubic (BCC), tetrahedron with horizontal struts (TetH), and pyramidal (Pyr) are considered. These models are used to understand the failure mechanisms and relation between post-yielding deformations and the topologies of the lattice. All of these configurations were tested under compression in the z direction under quasi-static conditions and are compared with the FEA results. The post-yielding behavior obtained from FEA match reasonably well with the experimental observations providing the validity of the FEA models.

Therefore, in this dissertation, finite element models are developed using ABAQUS and validated according to previous experimental results to design application-specific LCS. First, an efficient and user-friendly tool was developed and this tool is called the Lattice Structure Designer (LSD). The LSD was developed from ABAQUS GUI and using Python scripting. This tool can be used to create the lattice models, define the materials, define the geometry, define the boundary conditions, apply loads, and submit the jobs to perform the computational analysis. The same tool can be used to access the database files and calculate any additional outputs. This ABAQUS plug-in has effectively helped to capture the responses beyond the plasticity levels and capture the failure mechanisms of the lattice under compression and impact loads.

Contents

Chapter 1.	Introduction	1
1.1	Motivation	1
1.2	Literature Review.....	3
1.2.1	Background.....	3
1.2.2	The Lattice Structures Configurations: Recent Works	4
1.2.3	Quasi-Static and Low-Velocity Impact Tests	21
1.2.4	The Finite Element Analysis (FEA) Models	21
1.2.5	Specific Energy Absorption.....	36
1.2.6	Progressive Damage Mechanism.....	37
1.2.7	Additive Manufacturing (AM).....	39
1.3	The Research Scopes	40
1.3.1	Problem Statements	40
1.3.2	Dissertation Goals.....	41
1.4	The Dissertation Outline.....	42
Chapter 2.	The Finite Element Modeling of the Lattice Cell Structure	44
2.1	Overview.....	44
2.2	Mesh Generation	45
2.3	Material Properties	47
2.4	The Fracture Criteria.....	48
2.5	Model Verification using Tensile Samples	49
2.6	Modeling the Compression Tests of LCS	50
2.6.1	BCC 1st Layer Collapse (Experimental Vs FEM).....	51
2.6.2	BCCV 1st Layer Collapse (Experimental Vs FEM).....	53
2.6.3	BCCA 1st Layer Collapse (Experimental Vs FEM).....	54
2.7	The Low Velocity Impact Test Modeling Results.....	55
2.8	Impact Test Results	56
2.8.1	Finite Element Model for The Impact Test for BCC.....	56
2.8.2	Finite Element Model for The Impact Test for BCCV	57
2.8.3	Finite Element Model for The Impact Test for BCCA	57
2.8.4	Impact Specific Energy Absorption (SEA).....	57
2.9	Summary	60
Chapter 3.	Developing Python Code for Lattice Structure Designer (LSD)	62

3.1	Overview.....	62
3.2	ABAQUS /Python Graphical User Interface (GUI).....	63
3.3	Developing ABAQUS Plug-In Tool GUI to Create and Perform ABAQUS Modeling	64
3.4	The LSD Algorithm Flow Chart	65
3.5	The LSD Input Data and Characters	67
3.6	Python Interpreter	70
3.6.1	Creating the Geometry and Decomposition.....	71
3.6.2	Face Recognition	74
3.6.3	Cell Patterns and Union	77
3.6.4	Body Recognitions.....	84
3.6.5	Features Union.....	85
3.6.6	Creating the Rigid Plates	85
3.6.7	Assigning the Boundary Conditions	86
3.6.8	Creating Output Sets and Steps.	87
3.6.9	Applying the Mesh	88
3.6.10	Debugging of the Materials for Modeling	90
3.6.11	Creating the Job for the Submission	95
3.7	Summary	96
Chapter 4.	Application and Validation of LSD Tool.....	97
4.1	Overview.....	97
4.2	Tool Installation.....	97
4.3	LSD Tool Running.....	98
4.3.1	First Group (BCC, BCCV, and BCCA).....	99
4.3.2	Second Group (Tet and TetH)	103
4.3.3	Third Group (Pyr).....	103
4.4	Assigning the Materials.....	103
4.5	Submitting the Job	104
4.6	The LSD Outputs.....	107
4.6.1	Model Validation for the BCC Configuration	107
4.6.2	Model Validation for the BCCV Configuration	108
4.6.3	Model Validation for the BCCA Configuration	109
4.6.4	Model Validation for the Tetra Configuration.....	110
4.6.5	Model Validation for the Tetrahedron (TetH) Configuration.....	111

4.6.6	Model Validation for the Pyramidal Configuration.....	111
4.7	The LSD Tool Validation.....	112
4.7.1	Comparison of FEM with Experimental Results for ABS.....	112
4.7.2	Comparison with Published FEM Results for Titanium Alloy.....	113
4.8	Summery	115
Chapter 5.	Progressive Damage Analysis.....	116
5.1	Overview.....	116
5.2	Ashby and Gibson Failure Stages Model Background	116
5.3	Progressive Damage Analysis for BCCV.....	118
5.4	Progressive Damage Analysis for TetH.....	123
5.5	The Plateau Stages Validation for The BCCV and Tetrahedron.....	126
5.6	Evaluation of Plateau Stress, Absorbed Energy, and Efficiency	129
5.7	Summary	132
Chapter 6.	Summery and Future Work	133
6.1	The Research Contributions.....	135
6.2	Future Work	137
References	139
Appendix A:	Debugging The BCC with Geometric Decomposition	155
Appendix B:	Assigning the Ti-6Al-4V Alloy Debugging	162
Appendix C:	Assigning Undefined Materials Debugging	164
Appendix D:	Assigning the Boundary Conditions	165
Appendix E:	Assigning the Mesh.....	166
Appendix F:	Assigning the Job	167

List of Figures

Figure 1.1 (a)Tetra and (b)Tetrahedron	5
Figure 1.2 Pyramidal configuration	5
Figure 1.3 Tetra compression test result	6
Figure 1.4 Tetrahedron compression test result	6
Figure 1.5 Pyramidal compression test result	7
Figure 1.6 (a) BCC one cell, and (b) BCC lattice multi cells configuration.....	9
Figure 1.7 lattice structure notations (a) BCC (b) BCCV (c) BCCA , and(d) BCCG	9
Figure 1.8 Compression test preparation	10
Figure 1.9 BCC compression test results	11
Figure 1.10 BCCV compression test results	11
Figure 1.11 BCCA compression test results	12
Figure 1.12 Lattice BCC and BCC-Z (Smith’s work)	15
Figure 1.13 One unit cell for BCC and BCC-Z geometry decomposed	15
Figure 1.14 Modeling and experimental comparison	16
Figure 1.15 (a) Impactor machine ASTM 7136 (b) Impactor assembly with accelerometer (c) Four toggle clamps and four load cells.....	18
Figure 1.16 Specimen clamped with 4 toggle clamps.	19
Figure 1.17 BCC specimen for the impact test	19
Figure 1.18 Deformed Specimens after testing (a) BCC (b) BCCAV	20
Figure 1.19 Total Energy captured by AL Rifaie for 4 configurations	20
Figure 1.20 Finite element model for sandwich edge fracture	23
Figure 1.21 SolidWorks Associative Interface tools	25

Figure 1.22 ABAQUS Mesh library and control	27
Figure 1.23 Regular shapes structural meshable by ABAQUS	28
Figure 1.24 Geometric decomposition.....	28
Figure 1.25 Material properties along with the damage criteria adopted for the finite element models [78, 87].....	29
Figure 1.26 Full range of stress triaxility vs equivalent strain [67].....	31
Figure 1.27 Characteristic stress-strain behavior of progressive damage [78].....	36
Figure 1.28 Ashby and Gibson failure stages for the lattice form [7].	39
Figure 2.1 SolidWorks Associative interface tool to ABAQUS/CAE	45
Figure 2.2 (a)Lattice structure with tetrahedron mesh, and (b) The convergence curve ..	46
Figure 2.3 Experimental ABS stress strain for the tensile test	47
Figure 2.4 (a)Ductile Damage plug in ABAQUS, and (b) Shear Damage plug in ABAQUS	48
Figure 2.5 Standard ASTM 638 modeling and experimental results comparisons	49
Figure 2.6 Boundary condition assumption for the compression model	50
Figure 2.7 ABAQUS Boundary condition applied.	51
Figure 2.8 BCC modeling simulation and real experimental comparison.....	52
Figure 2.9 BCCV modeling simulation and real experimental comparison.....	53
Figure 2.10 BCCA modeling simulation and real experimental comparison.....	54
Figure 2.11 (a) Boundary condition of the entire model, and (b) boundary condition for one quarter	56
Figure 2.12 BCC impact results experimental and FEM (a) Impact simulation (b) Acceleration-time (c) energy-time, and (d) force-time.....	58

Figure 2.13 BCCV impact results experimental and FEM (a) Impact simulation (b) Acceleration-time (c) energy-time, and (d) force-time.....	59
Figure 2.14 BCCA impact results experimental and FEM (a) Impact simulation (b) Acceleration-time (c) energy-time,and (d) force-time.....	60
Figure 3.1 Tetrahedron and hexahedron characteristics comparisons	63
Figure 3.2 Initial Python flow chart.....	66
Figure 3.3 Proposed GUI programming	66
Figure 3.4 First input portion (a) ComboBox, and (b) List Item	68
Figure 3.5 Second Input for three groups of dimensions.....	68
Figure 3.6 Third input for the materials.....	69
Figure 3.7 BCC (a) Decompose one cell, and (b) Optimum brick mesh for entire BCC lattice.....	72
Figure 3.8 BCC Unit cell debugging	73
Figure 3.9 One cell partitioning debugging with 6 planes for each strut.....	73
Figure 3.10 Mesh test for one-cell BCC	74
Figure 3.11 BCC unit cell faces recognition for 8 faces on top side	75
Figure 3.12 For unit BCC face finding and tying with the rigid plate.....	76
Figure 3.13 Final stage of Faces Tie with the Rigid plates.....	77
Figure 3.14 Basic Linear pattern stages for the Lattice	79
Figure 3.15 performing linear pattern by using smart 3D vector debugging.....	80
Figure 3.16 Tetra and Tetrahedron arrays and arrangements	81
Figure 3.17 Top view of the Tetrahedron shows the flipped cells arrangements	82
Figure 3.18 Tetrahedron vertical arrays adjustments debugging.....	83

Figure 3.19 Body recognition technique debugging.....	84
Figure 3.20 Feature union debugging	85
Figure 3.21 Rigid plates creating and adjusting.....	86
Figure 3.22 Assigning the boundary conditions in the rigid plates	87
Figure 3.23 Debugging the output in the reference points at the rigid plates	88
Figure 3.24 Tetra with ideal brick mesh	89
Figure 3.25 Ideal meshed BCC lattice structure created by the GUI.....	90
Figure 3.26 Creating Material Library (a) ABAQUS model space, and (b) Python Code	92
Figure 3.27 Creating Material Homogeneous section (a) ABAQUS model space , and(b) Python Code.....	93
Figure 3.28 Assign the Material the Material section to the Model (a) ABAQUS, and (b) Python	94
Figure 3.29 Material frame for any other Materials (a) GUI frame, and (b) Python code	95
Figure 3.30 Python code for assigning the Job	96
Figure 4.1 Run the LSD tool.....	99
Figure 4.2 Fadeel tool interface main menu	100
Figure 4.3 The Tool interface details	101
Figure 4.4 BCC result from Fadeel Tool, (a) Entire lattice ,and (b) one cell	102
Figure 4.5 BCCV result from Fadeel Tool, (a) Entire lattice and (b) one cell	102
Figure 4.6 BCCA result from Fadeel Tool, (a) Entire lattice (b) one cell and (c) Alternative Vertical strut.....	102
Figure 4.7 Tetra with ideal mesh result from Fadeel Tool, (a) top view (b) side view, and (c) One-unit cell	104

Figure 4.8 Tetrahedron with ideal mesh result from Fadeel Tool, (a) top view (b) side view, and (c) One-unit cell.....	105
Figure 4.9 Pyramidal with ideal mesh result from Fadeel Tool, (a) Entire Lattice and (b) One-unit cell.....	106
Figure 4.10 Assigning the materials (a) name (b) density (c) Elasticity, and(d) Plasticity	106
Figure 4.11 Submission and running the Job.....	107
Figure 4.12 BCC model for post-yielding and experimental comparison	108
Figure 4.13 BCCV model for post-yielding and experimental comparison	109
Figure 4.14 BCCA model for post-yielding and experimental comparison	110
Figure 4.15 Tetra model for post-yielding and experimental comparison.....	110
Figure 4.16 Tetrahedron model for post-yielding.....	111
Figure 4.17 Pyramidal model for post-yielding and experimental comparison.....	112
Figure 4.18 FEM model for the Titanium model.....	114
Figure 4.19 Ti-6Al-4v models by LSD and Kadhodapour comparison.....	114
Figure 5.1 schematic Ashby and Gibson failure stages for the lattice form for the compressive stress strain behavior.....	118
Figure 5.2 BCCV initial stage with (a) Side view (b) Location in the curve (c) Top plan (d) Section x, and (e) Section y.....	119
Figure 5.3 BCCV stage(1) with (a) Side view (b) Location in the curve (c) Top plan (d) Section x ,and (e) Section y.	120
Figure 5.4 BCCV stage(2) with (a) Side view (b) Location in the curve (c) Top plan (d) Section x ,and (e) Section y.	120

Figure 5.5 BCCV stage(3) with (a) Side view (b) Location in the curve (c) Top plan (d) Section x ,and (e) Section y.	121
Figure 5.6 BCCV stage(4) with (a) Side view (b) Location in the curve (c) Top plan (d) Section x ,and (e) Section y.	121
Figure 5.7 BCCV stage(5) with (a) Side view (b) Location in the curve (c) Top plan (d) Section x ,and (e) Section y.	122
Figure 5.8 BCCV stage(6) with (a) Side view (b) Location in the curve (c) Top plan (d) Section x ,and (e) Section y.	122
Figure 5.9 BCCV stage(7) with (a) Side view (b) Location in the curve (c) Top plan (d) Section x ,and (e) Section y.	123
Figure 5.10 BCCV stage(9) with (a) Side view , and (b) Location in the curve	123
Figure 5.11 Tetrahedron initial stage with (a) Side view (b) Location in the curve (c) Top plan (d) Section x ,and (e) Section y.	124
Figure 5.12 Tetrahedron stage(1) with (a) Side view (b) Location in the curve (c) Top plan (d) Section x ,and (e) Section y.	125
Figure 5.13 Tetrahedron stage(2) with (a) Side view (b) Location in the curve (c) Top plan (d) Section x ,and (e) Section y.	125
Figure 5.14 Tetrahedron stage(3) with (a) Side view (b) Location in the curve (c) Top plan (d) Section x ,and (e) Section y.	126
Figure 5.15 Tetrahedron stage(4) with (a) Side view (b) Location in the curve (c) Top plan (d) Section x ,and (e) Section y.	126
Figure 5.16 The BCCV Plateau progressive FEM vs Experimental at strain of 0.06	127

Figure 5.17 The Tetrahedron Plateau progressive FEM vs Experimental at strain of 0.06	128
Figure 5.18 The BCCV Plateau progressive FEM vs Experimental at strain of 0.26	128
Figure 5.19 The Tetrahedron Plateau progressive FEM vs Experimental at strain of 0.36	128
Figure 5.20 identifying the Plateau parameters for BCCV (a) Stress-strain and efficiency, and (b) Peak stress vs Absorb energy W	131
Figure 5.21 identifying the Plateau parameters for TetH (a) Stress-strain and efficiency, and (b) Peak stress vs Absorb energy W	131

List of Tables

Table 2.1 the convergence of the maximum displacement due to the time scaling value	46
Table 2.2 Printed polymeric ABS properties	48
Table 2.3 SEAs comparisons FEM vs experiment for the Impact test	60
Table 3.1 Second input data parameters	69
Table 3.2 Material parameters for the Third input.....	70
Table 3.3 Elasticity and density parameters for the ABS	91
Table 3.4 First and Last point for Plasticity stage for the ABS	91
Table 3.5 Elasticity and density parameters for the Ti-6AL-4V [123, 30].....	91
Table 3.6 First and Last point for Plasticity stage for the Ti-6AL-4V [123, 30].....	92
Table 4.1 Comparison of FEA results with the experimental counterpart along with associated Errors	113
Table 5.1 The Plastic plateau parameters and energy absorption for the ABS lattice configurations.	130

Acknowledgements

I would like to take this opportunity to thank my advisor Dr. Ahsan Mian for his mentoring and guidance throughout my graduate studies. His guidance and experience encouraged me to work hard and have helped me to grow as an academician, a researcher, and as a person and instilled the confidence to continue to pursue my goals in the field of engineering and technology.

I would also like to thank the members of my dissertation committee: Dr. Raghavan Srinivasan, Daniel Young, Joy Gockel, and Golam Newaz. They were more than generous with their expertise and have immense knowledge that helped me in my PhD studies and research. Their insightful comments have no doubt increased the quality of this work.

The faculty and staff at Wright State University (WSU) also deserve a great deal of credit for my success. I would like to extend my special thanks to WSU's ONEIL Center for Research Communications for considering and taking the time to revise the manuscript of this research.

I also could not have completed this work without my friends and colleagues in the Advanced Manufacturing Research Lab at WSU. I thank Abdulhadi, Alwattar, and Hamad for their support and discussions. I wish them all the best in their future endeavors.

Finally, I would like to thank my family for their confidence in me and unwavering support throughout my years in higher education. I will be forever grateful for sacrifices that they have made in order to help me reach this goal.

Dedicated to my late mom (Afia) and to my Dad (Ibrahim)
*And to my late Grandfather (Fadeel) who loved the knowledge more than
ever that can be said*
Also, To my wife and my kids

Chapter 1. Introduction

1.1 Motivation

Lattice cell structure (LCS) based cellular materials have become important field of research due to many reasons. Many applications, such as marine and aerospace, demand optimal materials that are light weight, strong, able to absorb strain energies. LCS are currently being studied as a core material for sandwich structures. Despite much published research in the field, there is a lack of efficient numerical schemes to computationally model the LCS based cellular materials. The computational approach can be used to study and optimize the sandwich structure based on the geometrical design. It may be mentioned that sandwich materials are promising materials that can be upgraded and enhanced according to the geometrical design. Development of new manufacturing techniques, such as three-dimensional (3D) printing, has helped create complex geometrical shapes, such as LCS, efficiently with lower cost. In 2009, a study at the University of Liverpool [1] showed that the metallic LCS structure can compete with the aluminum foam and aluminum honeycomb structure. This encourages researchers to focus their attention on engineering LCS. Since the overall mechanical properties of LCS depend on the type of raw materials and the geometrical topology, much of the research has been focused on creating and experimentally characterizing the LCS. For example, the LCS cores made of aluminum alloys have shown excellent mechanical behavior under compression and shear [1].

Recently, the 3D printing technology, such as extrusion based fused deposition modeling (FDM), has been explored to create complex geometric parts such as LCS [2-5]. Acrylonitrile butadiene styrene (ABS) is a widely used filament in FDM 3D printers. According to the recent experimental research, it has been proven that the ABS lattice can provide good strain energy absorption. For example, the body centric cubic (BCC), tetrahedral, and pyramidal configurations made of ABS have been designed, fabricated, and tested under compression and impact loads. For example, the BCC configuration has been upgraded by adding and distributing vertical struts. The tetrahedron lattice has been modified by adding horizontal struts. Through this work, it was determined that the material behavior is sensitive to the geometric design more than any other factors. This is an encouraging point to study and optimize the geometrical design of LCS to get the best possible desired properties. However, fabricating many LCS designs with different design variables, e.g. lattice configuration, cell and strut sizes, and type of raw material is time consuming and expensive. For this reason, the demand for the use of computational approaches to predict the mechanical behavior of LCS is the preferred method. However, creating efficient computational model for LCS is not trivial and there is limited work done in the field of finite element modeling (FEM) technique to effectively analyze different LCS designs. Therefore, developing effective FEM schemes for modeling wide range of LCS designs will impact the design community tremendously and is the main focus of this study.

1.2 Literature Review

1.2.1 Background

Many studies have been conducted with a focus on sandwich materials due to their promising mechanical behavior [6-12]. The main aim of these studies is to seek designs with more stiffness and energy absorptions as well as less weight [6, 13-17]. For these reasons, sandwich materials have been used for many applications such as automobile and aerospace structures. The core of such structure is made of cellular materials. Because of the ability of honeycomb structure to absorb the energy, many studies have been involved with the honeycomb core sandwich structures [2-4, 18-24] in the last decade. The main application of sandwich structures, especially in the field of crashworthiness, requires high energy absorption capabilities and light shock absorption [6, 18, 25].

Also, the cellular materials can offer many benefits such as thermal resistance, durability, low density, and lower cost [9, 26- 31]. Cellular materials are typically designed to absorb energy by recoverable elastic deformation. Cellular materials are also designed to provide good stiffness and absorb more energy [9, 32- 34]. According to Mines and others, a metallic lattice structure, developed at Liverpool, can compete with aluminum foam and aluminum honeycomb [1]. Also, according to Kooistra et al 2008 [35], the tetrahedron lattice structure can compete with the shear stiffness of LCS with honeycomb topology. Moreover, it can offer benefits such as higher specific energy and strength [35]. Since the LCS is capable of a low density core with acceptable stiffness and energy absorption, many researchers have focused on this lattice design [5, 32, 36-43]. However, due to the complexity of manufacturing the lattice by the traditional manufacturing methods, additive manufacturing is currently being explored to create the LCS samples

[44-50]. This research will focus on the LCS engineering using a FEM computational technique because the properties of cellular materials heavily depend on the raw material from which it is made and the cell geometrical shape and size cells.

1.2.2 The Lattice Structures Configurations: Recent Works

Some of the recent LCS work performed at Wright State University (WSU) and elsewhere are explained in brief in the following subsections.

1.2.2.1 Sangle's Work at WSU

According to Sangle 2017 [51], five types of 3D printed lattice configurations were tested under compression load. The configurations were (a) BCC without vertical struts, (b) BCC with alternative vertical struts, (c) tetra (Figure 1.1(a)), (d) tetrahedron with horizontal struts (Figure 1.1 (b)), and (e) pyramidal as shown in Figure 1.2 [51]. According to Sangle's [42] experimental results and analyses, the tetrahedron with horizontal struts shows the highest specific energy absorption (SEA) capability. Load displacement behaviors of tetra, tetra with horizontal struts, and pyramidal LCS are shown in Figures 1.3, 1.4, and 1.5, respectively. Fabrication and test procedures used in this case were similar to the methodologies used by Al Rifaie [52] and are explained in the next subsection.

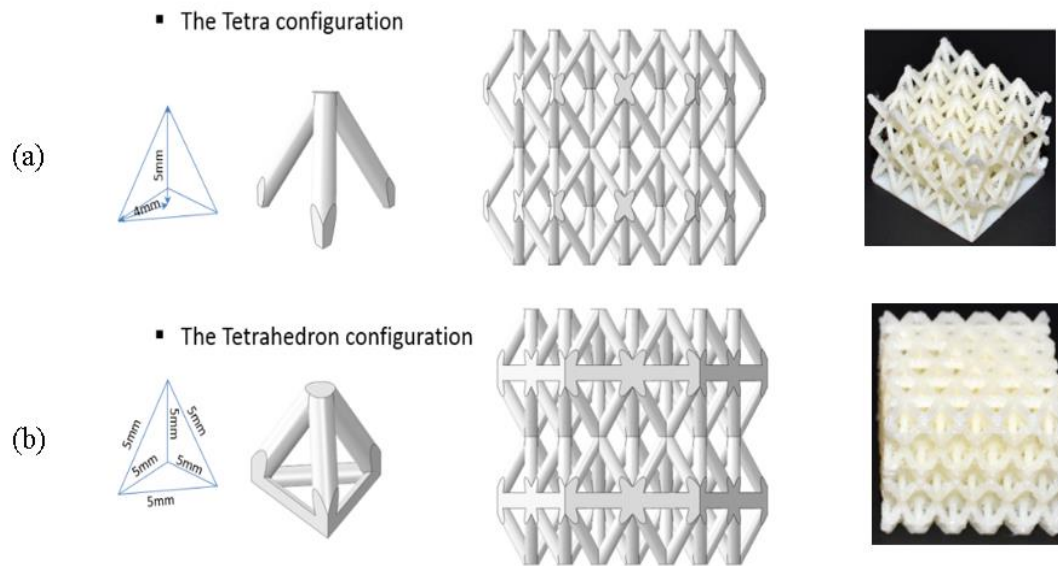


Figure 1.1 (a)Tetra and (b)Tetrahedron

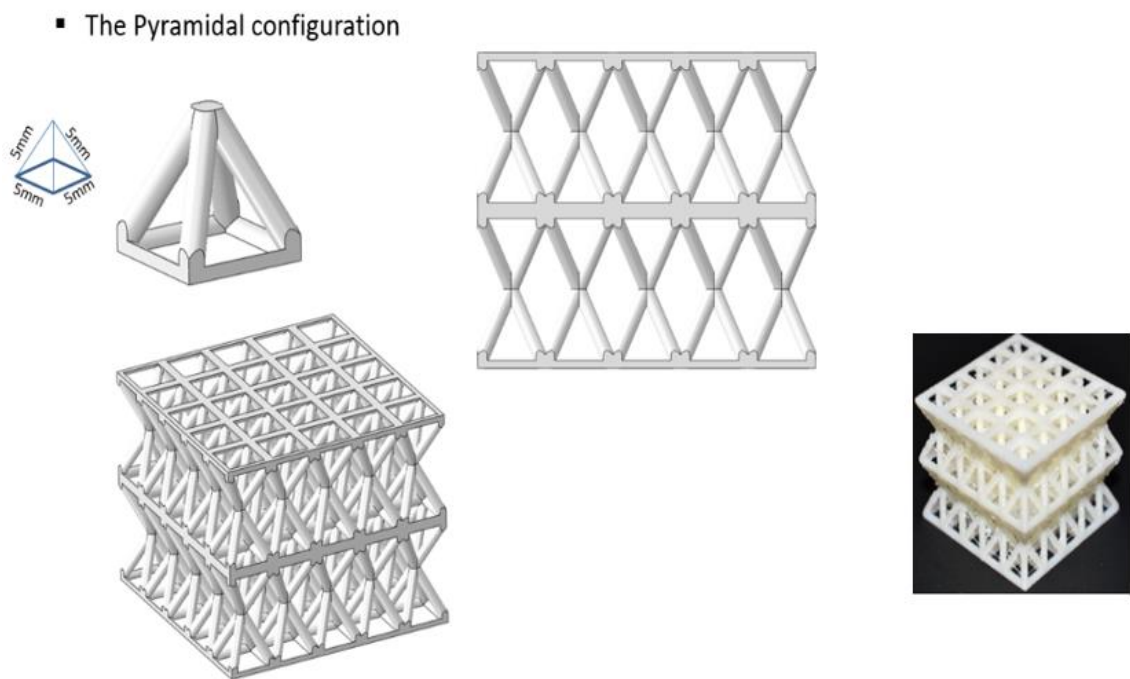


Figure 1.2 Pyramidal configuration

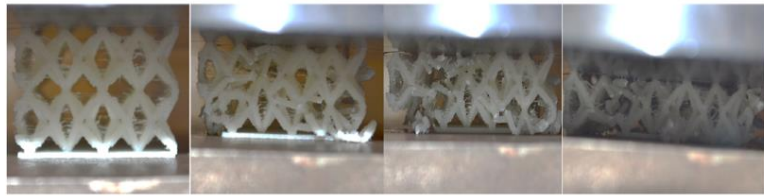
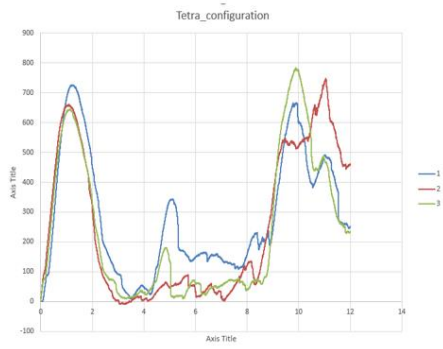


Figure 1.3 Tetra compression test result

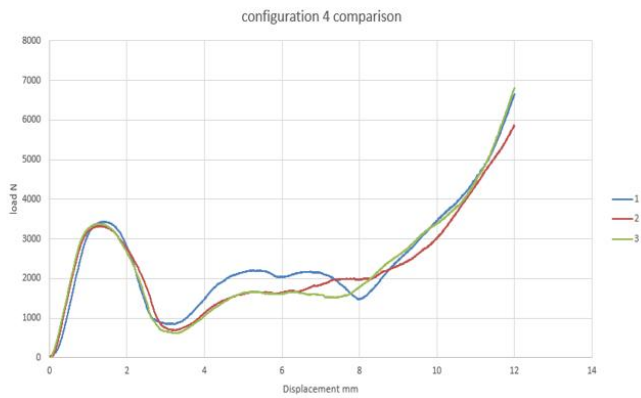


Figure 1.4 Tetrahedron compression test result

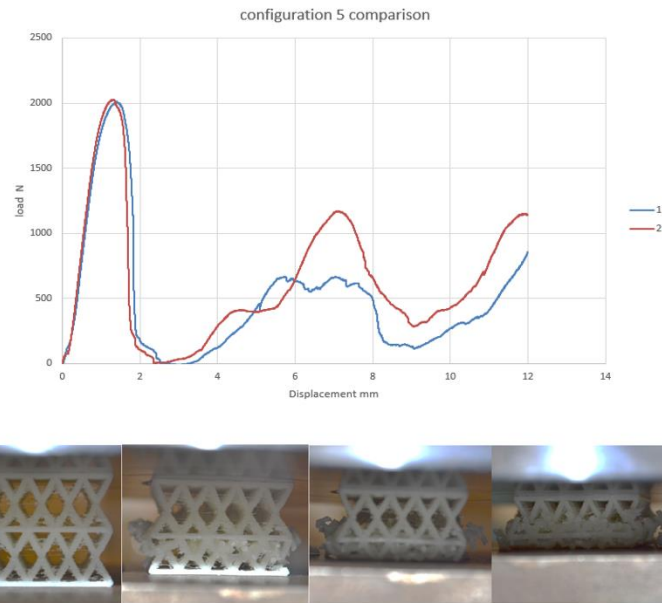


Figure 1.5 Pyramidal compression test result

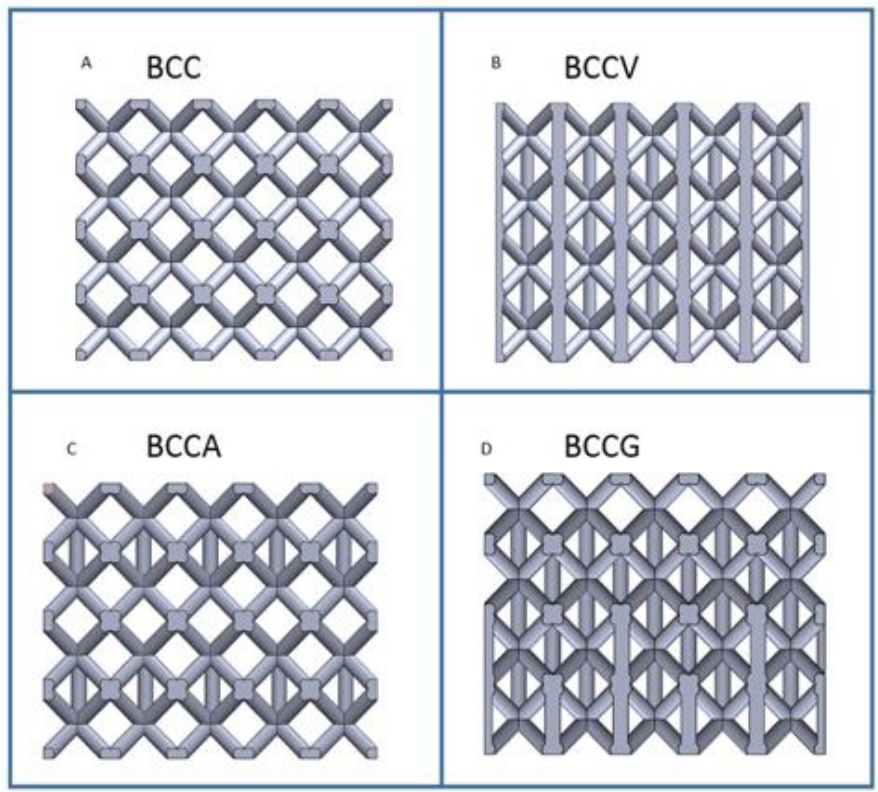
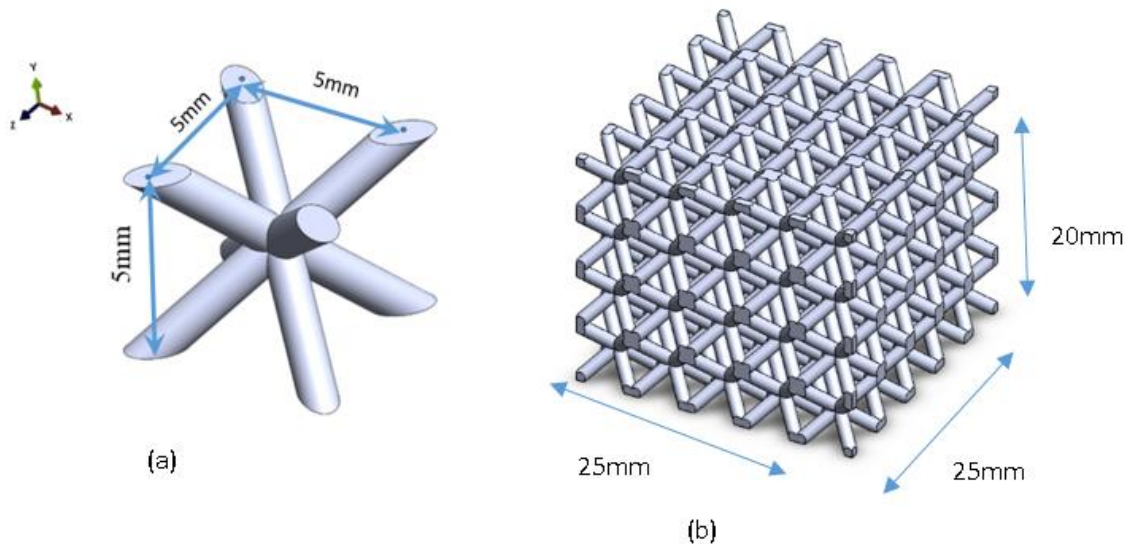
1.2.2.2 Al Rifaie's Work at WSU

In 2017, Al Rifaie investigated four types of 3D printed lattice configurations under compression load [52]. First configuration was basically BCC. The second configuration was by adding the vertical struts at every node and was denoted as BCCV. The third configuration was created by distributing the vertical struts alternatively layer by layer that was denoted as BCCA. The last configuration increased the number of vertical struts in the thickness direction creating gradient properties in the thickness direction and this was denoted as BCCG. According to the results and conclusion, the highest SEA was captured was with BCCV [52].

Sample Design and Fabrication

The four LCS models were designed using the CAD software SolidWorks® [52]. A body centered cubic (BCC) unit cell, shown in Figure 6(a) has dimensions of 5 mm x 5

mm x 5mm. The unit cell structure was arrayed 5 times each in the x and y directions and 4 levels in the z direction to create 25 mm x 25 mm x 20 mm lattices, as shown in 2D in Figures 1.7(a)-(b) for BCC, Other configurations such as BCCV, BCCA, and BCCG, respectively are shown in Figure (1.8 a,b,c,d). The study focused on the effect of vertical struts arrangements on the elastic/plastic behavior of different LCS. Here, the only variable considered was number of vertical struts and their arrangements. Thus, the cell size of 5 mm was kept fixed assuming that the similar arrangements of vertical struts would result in the similar change in compression behavior. The CAD files were converted to STL format and were further processed with the 3D printer software CatalystEX by Stratasys. A fused deposition modeling (FDM) 3D printer Stratasys uPrint SE Plus with a nozzle diameter of $2.54 \mu\text{m}$ was used to fabricate all four lattice structures using a production-grade thermoplastic (ABSplus-P430) provided by Stratasys [53]. Three samples for each configuration were printed. After removal of support structures, the average mass of the samples was 3.0 grams, 3.9 grams, 3.1 grams and 3.4 grams for BCC, BCCV, BCCA, and BCCG, respectively [52].



Compression Test

All the samples were tested by using Instron 5500R universal testing machine with a load capacity of 150 kN as shown in Figure 1.8 [52]. The tests were performed under displacement control of 0.5 mm/min. Instron's Bluehill2 software was used for controlling the data acquisition [52]. According to the results, there were progressive failures due to the configuration designs as shown in the Figures (1.9, 1.10, and 1.11). The results further show that there are multiple peaks having elasticity-plasticity stages and depend on the geometrical design and progressive failure of the sample.

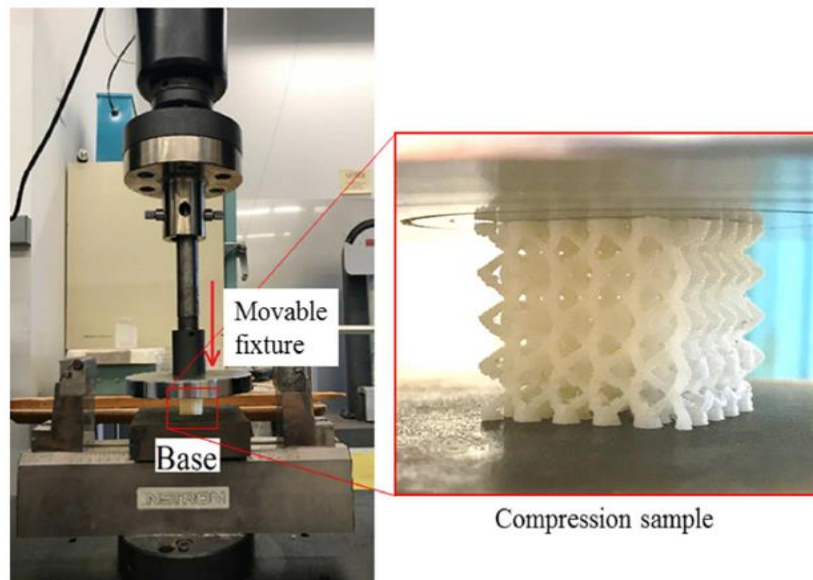


Figure 1.8 Compression test preparation

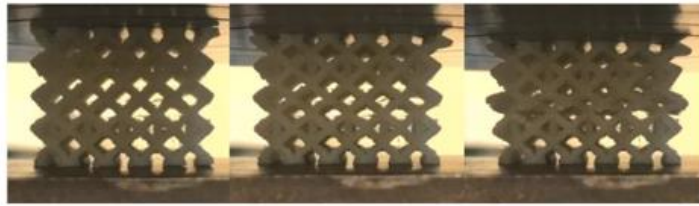
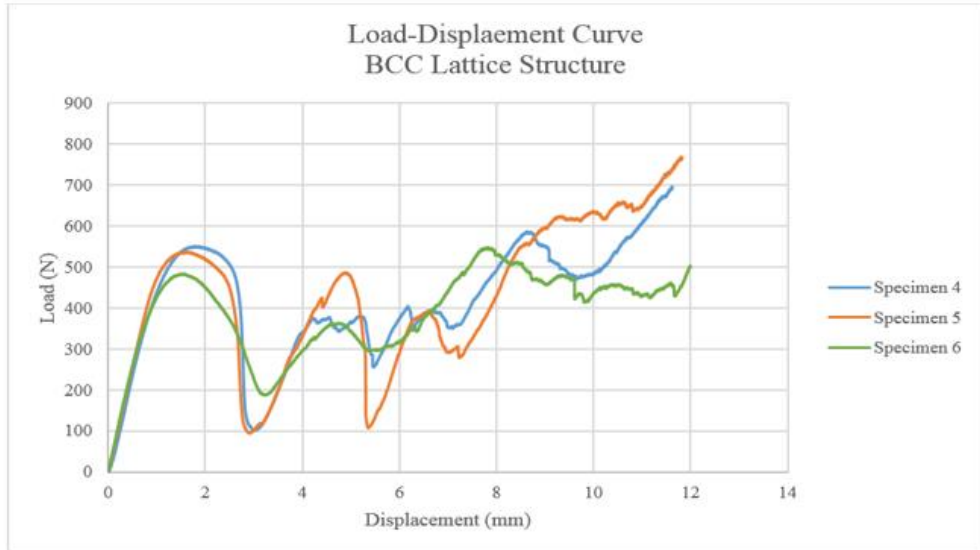


Figure 1.9 BCC compression test results

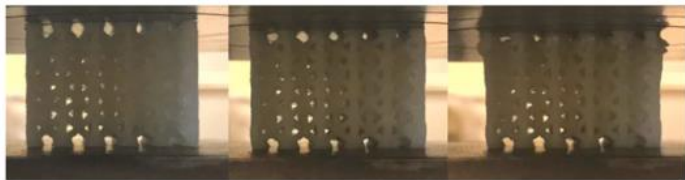
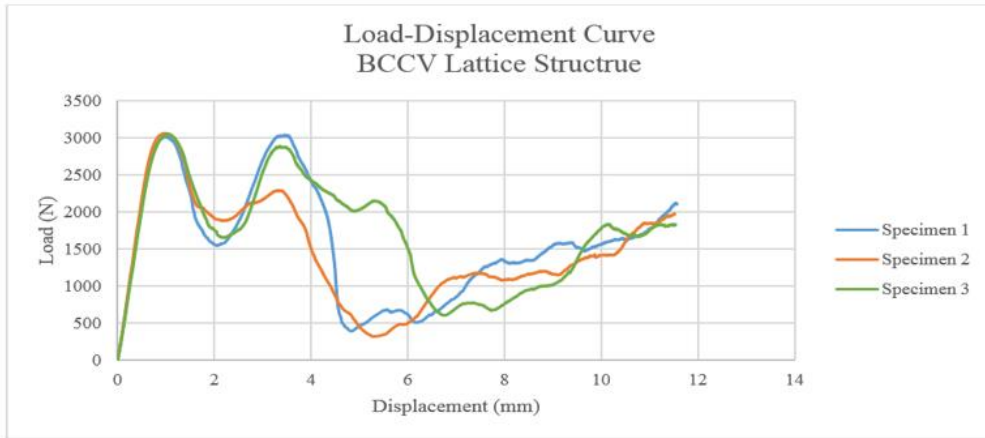


Figure 1.10 BCCV compression test results

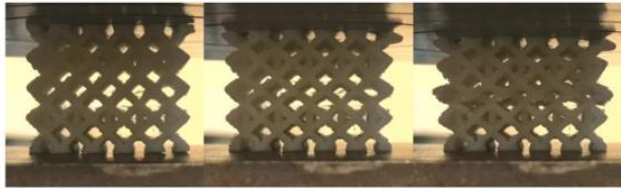
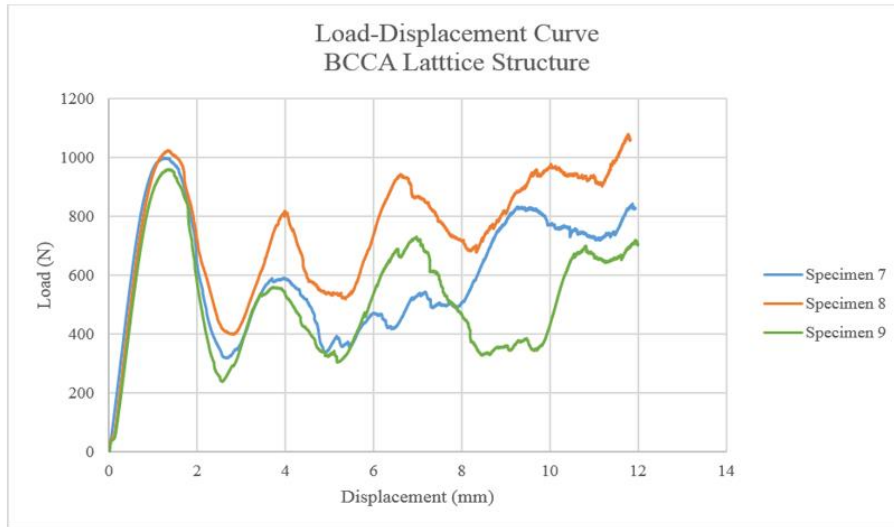


Figure 1.11 BCCA compression test results

1.2.2.3 Yadlapati's Work at WSU

Yadlapati, 2018, investigated the BCC lattice using different parameters of 3D printing [54]. These parameters were: the layer thickness (0.010 and 0.013 inches), angle of orientation to build (0, 45 and 90 degree), and two different infill densities (Sparse High Density and Solid). All the specimens were tested under quasi-static compression and tension. The stiffness, failure loads, and energy absorption were identified and compared based on the print parameters. According to his study, the printed orientation influences the yielding stress. In addition, reducing the layer thickness reduces the yielding stress by 33%. It was also noted that the infill density does not influence the failure stress for the LCS with 1 mm strut diameter [54].

1.2.2.4 Karmooz and other's Work

Karamoze and Kadkhodaei [41] developed a computational model for one strut and expanded that model for one cell. The model was developed to capture effect of the cross-sectional variations of 3D printed struts. In other words, the model was designed to consider the changing in diameters and pores due to the manufacturing process. They analyzed the struts using a Scanning Electron Microscope (SEM). SEM images were used to estimate and evaluate the struts geometry [41, 55, 56]. The simulations were repeated and evaluated many times until the results agreed with experimental findings. However, this model is effective for only one cell, and this model was built according to manufactured results for a specific case [41]. Also, this model worked within elastic limit, and the yielding limits, plasticity and fracture criteria were not considered [41, 55, 56]. Therefore, this model is not general purpose and was not recommended for any further study.

Also, Karamooz, Kadkhodaei, and Rezaei [56] developed FEM models for LCS using beam and solid elements. They observed that the beam element is stiffer than the solid element because the beam element cannot capture the effect of stress concentration at the points of diameter variation [56]. This model is good for describing the elastic modulus and collapse stress [56]. The strut diameter variations were calculated based on measurement of many points on each strut and using the probability theory [55, 56]. The material properties were identified based on the compression test of the bulk material [56]. The results show that the beam elements need at least ten or twelve intervals to get reasonable results, while the solid needs only one interval [56]. The results show that the models created and run using solid element are more accurate than the beam. However, the beam models were quicker to calculate [56].

1.2.2.5 Smith's Work

Smith, Guan and Cantwell (University of Liverpool 2014) [57] have demonstrated the compressive response of diamond BCC and diamond BCCZ lattice structures made by selective laser melting (SLM) and by FEM as shown in Figure 1.12. They used two methods to define the elements, 8-node continuum (3D brick) (linear Hexahedron mesh) and 2-node beam elements. Only one cell was modeled to avoid difficulties of dealing with the 8-node continuum (3D brick) element (Hexahedron meshes). Another reason for modeling only one cell was to reduce the computational time (see Figure 1.13) [57]. The model was treated many times and a lot of partitioning was done to make regular shapes which can be meshed with hexahedron elements. The effective diameter was identified based on a reverse engineering procedure. It was observed that both the element types were able to capture the elastic plastic stages with different accuracies. The 2-node beam element was able to capture the elastic-plastic stages, while the post-yielding was ambiguous. On the other hand, the 8-node (3D brick) element captured all the stages as seen in Figure 1.14. The collapse of the BCC-Z structure was different from that observed in the BCC structure, which is due to the localized buckling the vertical bars [57].

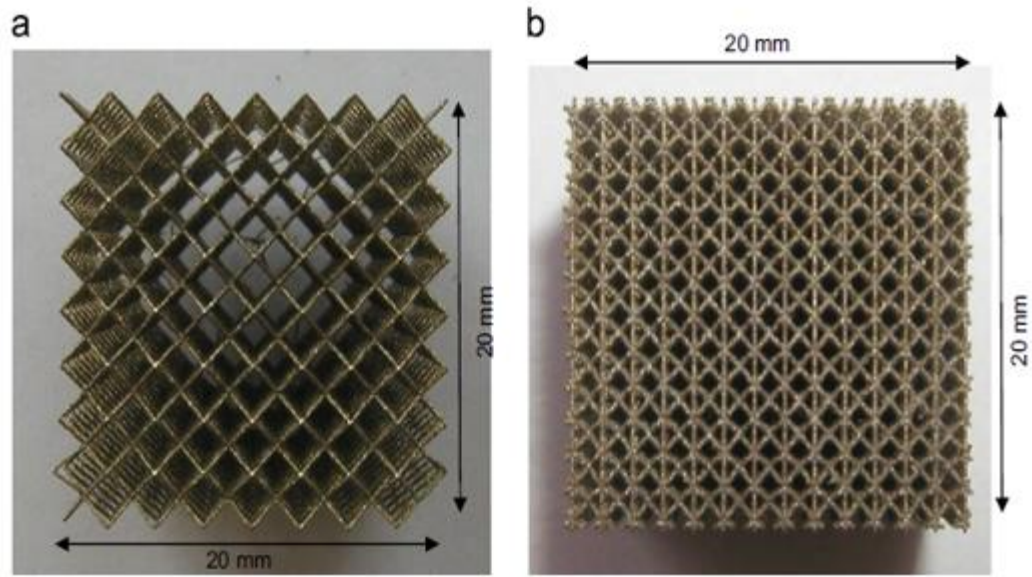


Figure 1.12 Lattice BCC and BCC-Z (Smith's work)

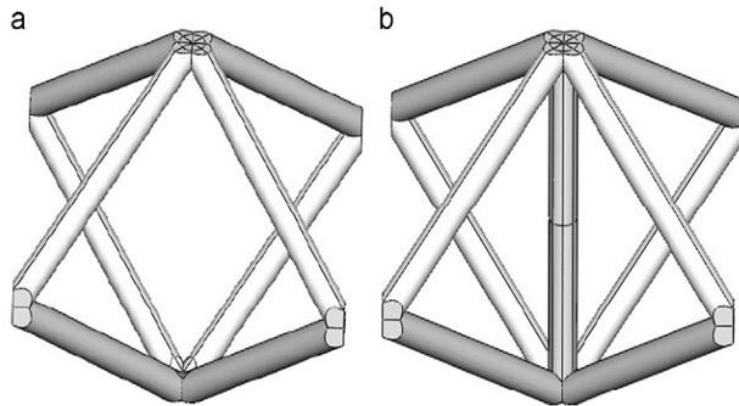


Figure 1.13 One unit cell for BCC and BCC-Z geometry decomposed

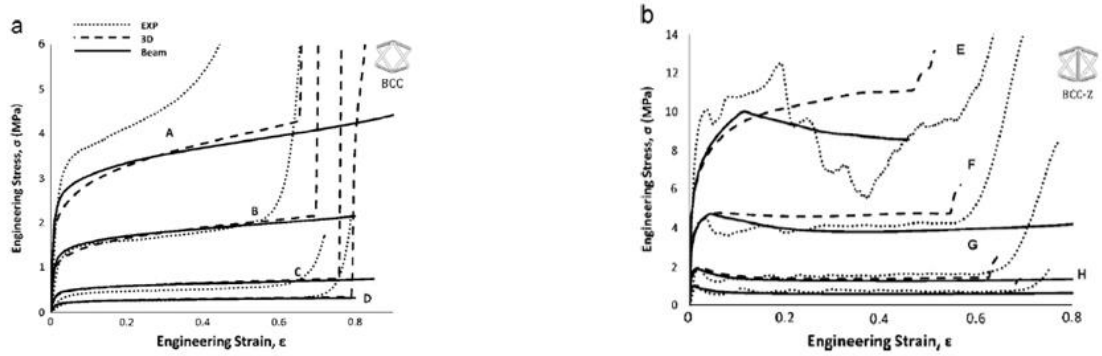


Figure 1.14 Modeling and experimental comparison

1.2.2.6 The Impact Test (Andrew Turner's Works) at WSU

In 2016, Turner [58] investigated the 3D printed lattice with low-velocity impact tests. The impactor machine was designed and fabricated according to ASTM D-7136 as shown in Figure 1.15(a). The maximum drop high was 0.65 m which corresponding to the initial velocity of 3.921m/s according to the equation (1).

$$v = \sqrt{2gh} \quad (1.1)$$

This machine was able to capture the acceleration using an accelerometer as shown in Figure 1.15 (b), and the reaction forces using four load cells as shown in Figure 1.15(c). All these sensors were adapted with the NI SignalExpress 2015 which captured and stored the data into DMT files. MATLAB code was developed to access the DMT file and to provide all the plots for the velocity-time, displacement-time, and energy absorption-time. The specimens can be clamped by 4 toggle clamps as shown in Figure 1.16. The specimens have been fabricated form core of 3D printed lattice structure adhered with 4 layers of Kevlar sheets on the top of the core as shown in Figure 1.17. Turner has tested 10 lattice structure specimens, 1 to 5 were BCC (Body centric cubic), and from 6 to 10 were BCCAV

(Body centric cubic with all vertical bars). Due to the impact tests, there were fatal damage the Kevlar sheet and the lattice polymer as shown in Figure 1.18. The tests also have shown there are multiple levels of energy absorption due to the specimen design. According to Turner's results the BCCAV has shown higher energy absorption at higher energy levels [58].

Additionally, according to Turner's apparatus for the low velocity impact test, Al Rifaie used it to investigate the impact response for the configurations of BCC, BCCV, BCCA, and BCCG [25]. The impactor mass was 2.439 kg, which created the impact kinetic energy level of 14.89 J. Turner captured the results according to the plots of acceleration-time, velocity-time, displacement-time, force-displacement. The analyses were based on the specific energy absorptions (SEA). Turner concluded that the BCCV has the highest energy absorption, whereas the BCCA has the highest specific energy absorption as shown in Figure 1.19.

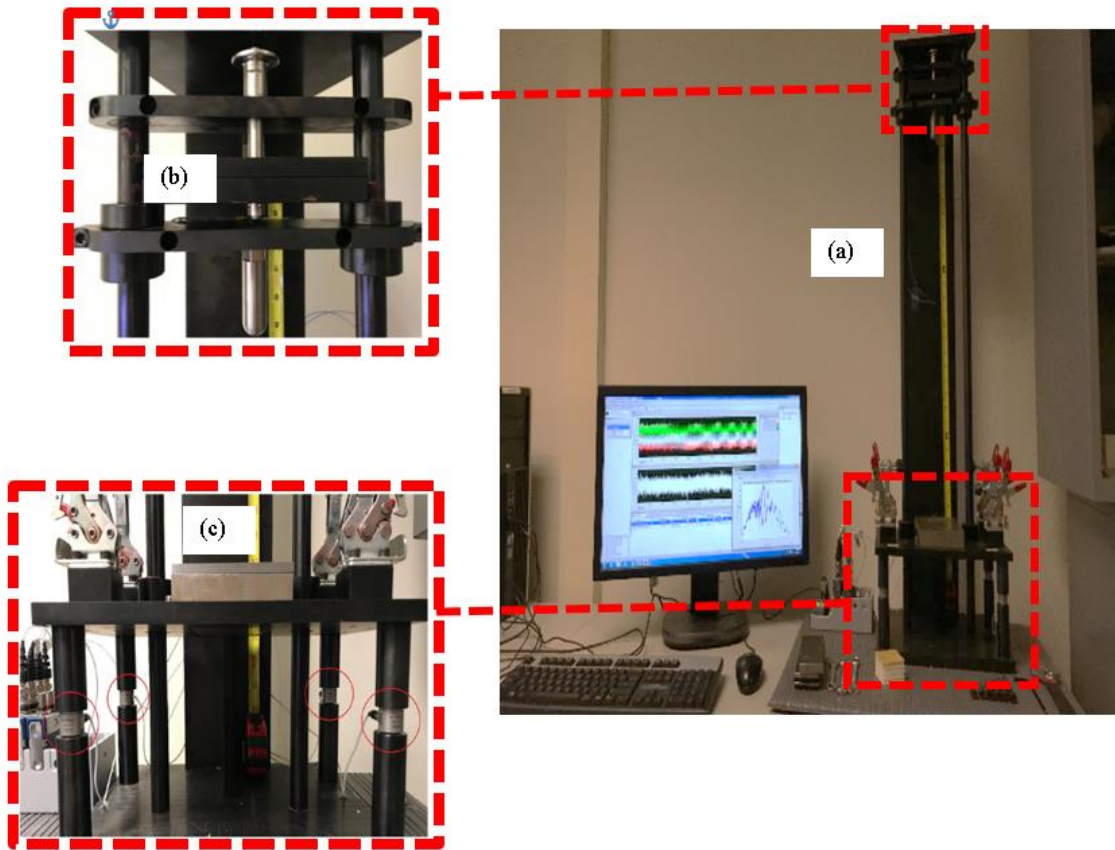


Figure 1.15 (a) Impactor machine ASTM 7136 (b) Impactor assembly with accelerometer (c) Four toggle clamps and four load cells

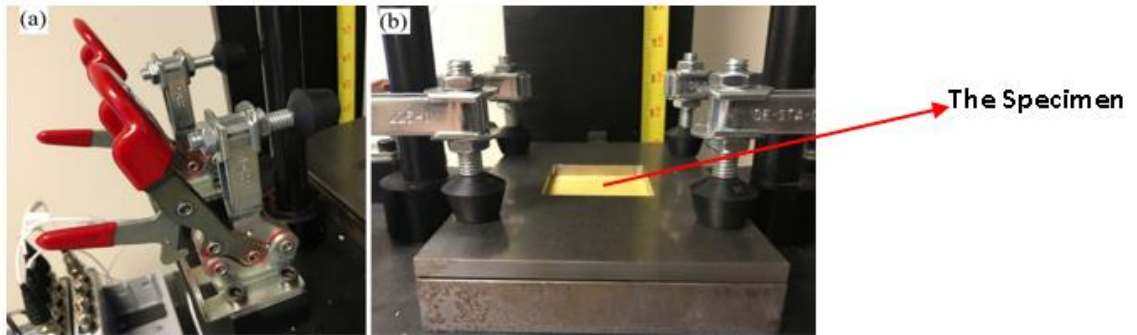


Figure 1.16 Specimen clamped with 4 toggle clamps.

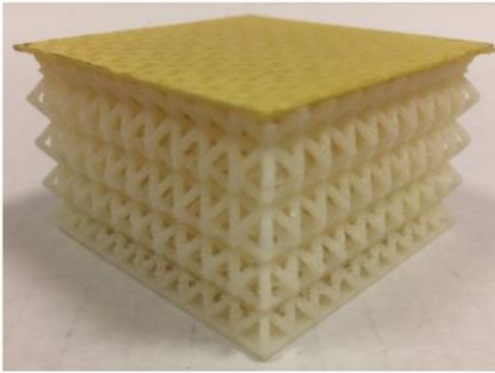


Figure 1.17 BCC specimen for the impact test

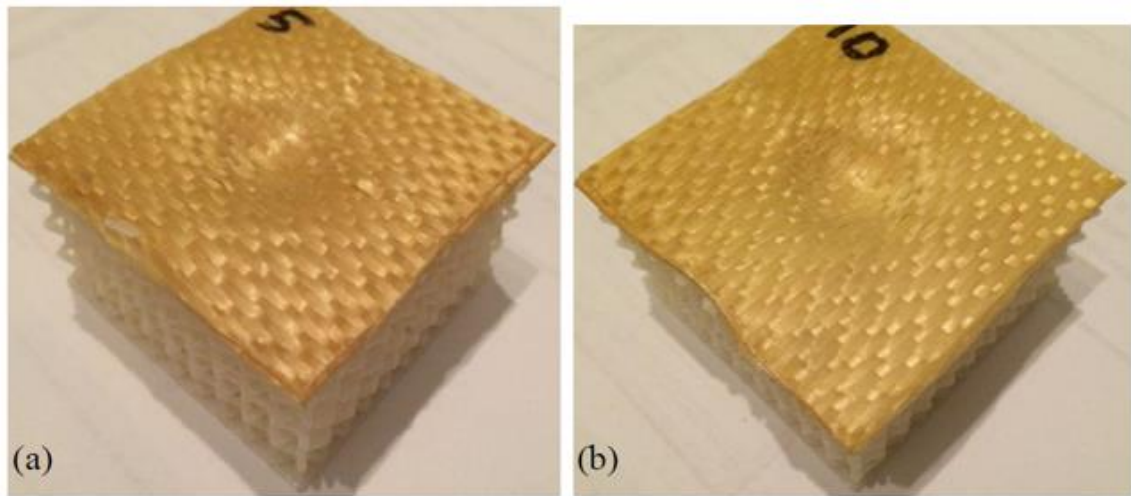


Figure 1.18 Deformed Specimens after testing (a) BCC (b) BCCAV

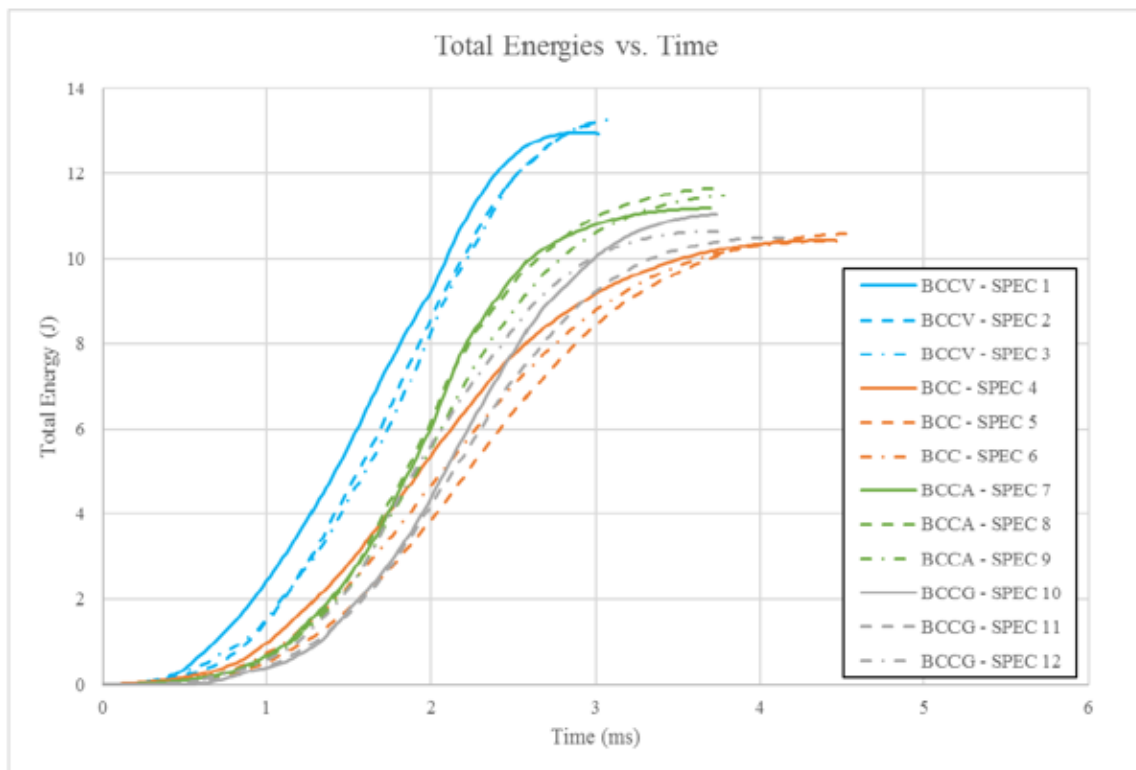


Figure 1.19 Total Energy captured by AL Rifaie for 4 configurations

1.2.3 Quasi-Static and Low-Velocity Impact Tests

Low velocity impact and quasi-static compression tests have been performed on LCS by several researchers [18, 25, 58-61]. To understand the materials behaviors, compression tests have been conducted on LCS with different materials and geometrical designs. The specific energy absorption (SEA) was used to compare between the samples [25, 58, 62]. According to previous studies, the SEA behavior is different for different core types. For example, foams and auxetic foams, honey comb, and lattice structure have different behaviors due to their geometric shapes [63]. The compression test was carried out to evaluate the mechanical strength of the lattice [25, 64]. It was observed that the specific strength is influenced by cell and strut sizes [64]. However, there were few studies that tested optimizing the lattice structures design based on the stiffness and strength [2]. Also, the impact tests can offer good sign of the material performance when the crash behavior of the LCS is desired [1,7].

1.2.4 The Finite Element Analysis (FEA) Models

Numerical approximation techniques have been developed to solve a variety of engineering problems. These include finite element, finite volume and finite difference techniques. They have been used to solve heat transfer, structural, fluid dynamics and so on [56]. However, according to Castabie [6], Jagtap [65] and Hashemi [66], the dynamic behavior models are more difficult than the static models due to how much computational time they use and the finite elements used. [6, 65, 66]. The FEA simulation is helpful to obtain progressive behaviors under dynamic loads. According to Castabie, Jagtap, Hashmi and Bao, the FEA software ABAQUS has proven capabilities to provide good approximation and correlation of the experimental data [6, 65, 67]. To get greater precision,

the behavior of the material must be defined precisely and correctly [26, 66]. Wang and Sanker [26] have modeled cellular materials based on the experimental observations. The experimental tests have shown that the struts are isotropic and linearly elastic, for these reasons they assumed the materials are homogeneous and isotropic materials. Consequently, they have developed the model by using the finite element software ABAQUS instead of using Euler-Bernoulli beam finite elements. Next, Wang and Sanker identified the best element type and size for high accuracy and reduction of the computational time [66]. To get better results, in agreement with the experimental data, the mesh should be practical and refined [68]. For this reason, the mesh should be chosen according to the mesh convergent results discovered in the data [68]. Also to improve the effectiveness of the FEA model, the micromechanics method has been developed to simulate the BCC LCS using ABAQUS [68]. It may be mentioned here, ABAQUS has been used widely to simulate and capture the mechanical behaviors of structures in many engineering applications.

1.2.4.1 Feasibility of ABAQUS to Capture Mechanical Behaviors

ABAQUS has been proven an efficient FEA software for capturing the mechanical behaviors [20, 22, 67-72]. Lê Van Sy 2009 [73] have modeled of metal and polymeric sheet. Although the model had faced some difficulties with long computational time, the FEM simulation captured the prediction of mechanical damage with explicit integration of finite elements [22, 73]. The mesh densities, mass scale, and precision of the material properties were seen to impact the prediction of the mechanical damage for the model. Identifying the material properties precisely help the model agree with the experimental results [73].

Kayode 2011 [74] studied the effect of defects and reverse bending on the properties of tensile armor wires [74]. The commercial finite element software ABAQUS was used to simulate the models. According to the results, the FEM model by ABAQUS successfully captured the tensile and shear failure mechanisms. The FEA predicted dent depth was approximately similar to the experimental measurement [74].

Saeid 2016 [75] modeled the progressive damage of sandwich T-joints. Different designs of composite sandwich T-joints were modeled and investigated under tension and bending loads [75-77]. The FEA model provided insights into the core failure and delamination. The combinations of elastic-plastic deformation the fracture criteria were able to predict good correlations with the experimental works as shown in Figure 1.20. The onset failure in the experimental results was first shown in the FEA model. The FEA models also accurately calculated all the mechanical properties of the structure such as stiffness and Young's modulus. Thus, the FEA model can help to design new sandwich T-joints with any other parameters [75].

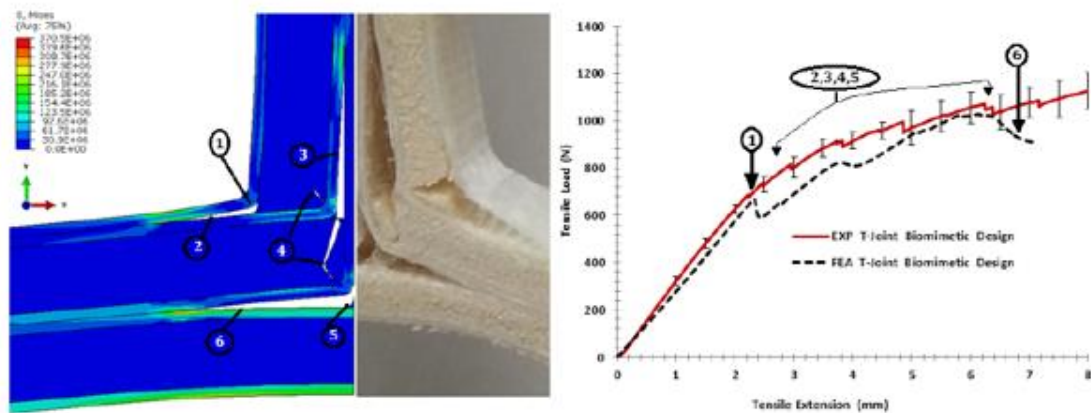


Figure 1.20 Finite element model for sandwich edge fracture

1.2.4.2 SolidWorks Associative Interface Tools

Due to the geometrical complexity of some models, it is often difficult to create them in ABAQUS. In such case, it is recommended to use any computer-aided design (CAD) software such as SolidWorks to create the model that can be exported into ABAQUS via the tool SolidWorks Associative Interface (SAI) as shown in Figure 1.21 [78]. This tool allows the transfer of parts or assemblies from SolidWorks to ABAQUS/CAE easily without losing any geometrical information [78]. Also, it is easy to change any dimensions or designs in SolidWorks and subsequently in ABAQUS. The model is updated without losing any analytical features such as partitions, boundary conditions, sets, and surfaces [78]. However, it might be required to regenerate the mesh for the model with the same conditions. For example, if the model mesh was with specific size and number of elements, it would not be changed. Moreover, it is necessary to retain the units of the model for consistency. For example, if millimeters (mm) is used for the displacements units, and Mega Pascal (MPa) for the stress units, the mass has to be in Tons (1000kg) and the density has to be plugged in as Tons/mm³.

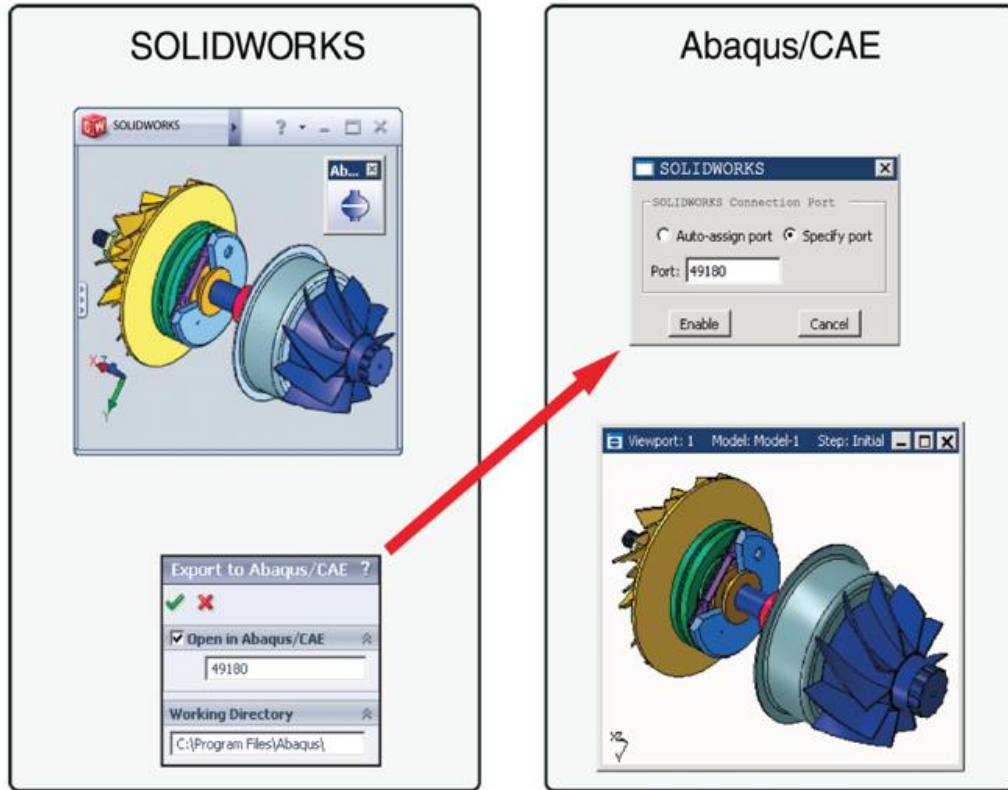


Figure 1.21 SolidWorks Associative Interface tools

1.2.4.3 Mesh Generation

The computer codes have been widely expanded and developed. These codes can automate mesh generation. One of its features is to find the most appropriate mesh element type for the elastic and elastic-plastic analyses. It uses automated meshing algorithms to reduce the amount of time needed to generate the model [79]. However, it is necessary to decompose the geometries having complex and difficult shapes [79]. The elements in the ABAQUS library have been enhanced and developed by Simulia according to a series of criteria called a family, degree of freedom, number of nodes, formulation, and integration as shown in Figure 1.24 ABAQUS [80]. The family is used to identify the element type based on the applications, i.e., solid, fluid, truss, shell, or infinite. The degree of freedom is the main aspect to be considered during the analysis. ABAQUS considers the degree of

each node to identify the stress/displacement simulation or rotation [80]. The number of nodes for each element is the indicator to identify the linearity or nonlinearity of the element [80]. Formulation refers to the mathematical theory used to define an element's behavior. Also, there are integration and combination of the elements that make up the LCS [80]. For the lattice structure modeling, tetrahedron and hexahedron elements can be used.

The tetrahedral mesh and hexahedral mesh have been compared based on the eigenvalues of elements stiffness matrices, linear static displacement, stresses, and also dynamic modal frequencies, plastic flow values, and also linear incompressibility conditions [81]. The accuracy and computational time are also used to compare the efficiency of the meshes [81]. According to some finite element books and many studies, it is necessary to consider the convergence characteristics. Convergence characteristics refers to the progressive limitation of the size of the elements of the mesh through the different iterations. It is key to refine convergence to ensure the FEA results do not change if the size of the mesh changes. The factors used to measure the FEA elements are basic type, element distortion, polynomial order, integration technique and material incompressibility [81, 82]. Quadrilateral elements are preferred for many reasons, including better accuracy and efficiency [81]. Linear tetrahedron shapes (LT) can produce maximum error while linear hexahedron (LH) can provide less error for bending applications [81, 82]. However, the quadratic elements generally have additional mid-side nodes that helps improve the precision. Quadratic hexahedrons (QH) shows slightly better performance than quadratic tetrahedron (QT) [81].

In dynamic models, the QH element is more acceptable than the LT element but both are used for incompressible materials [81]. The tetrahedron mesh is suitable for

complex geometrical shapes while the hexahedron elements are thought to work better for solid mechanics problems [83]. The reasons behind generating hex-dominant mesh is to control the results direction and avoid ill-shaped meshes [84]. Hexahedral meshes can be more feasible than the tetrahedral meshes for high elastic and plastic structures due to reduced errors [79]. However, hexahedral meshes are difficult to be automated. Hexahedron are preferred than tetrahedron due to reduced computational time [79]. For high deformation, tetrahedron is stiffer than hexahedron due to degree of freedom [79].

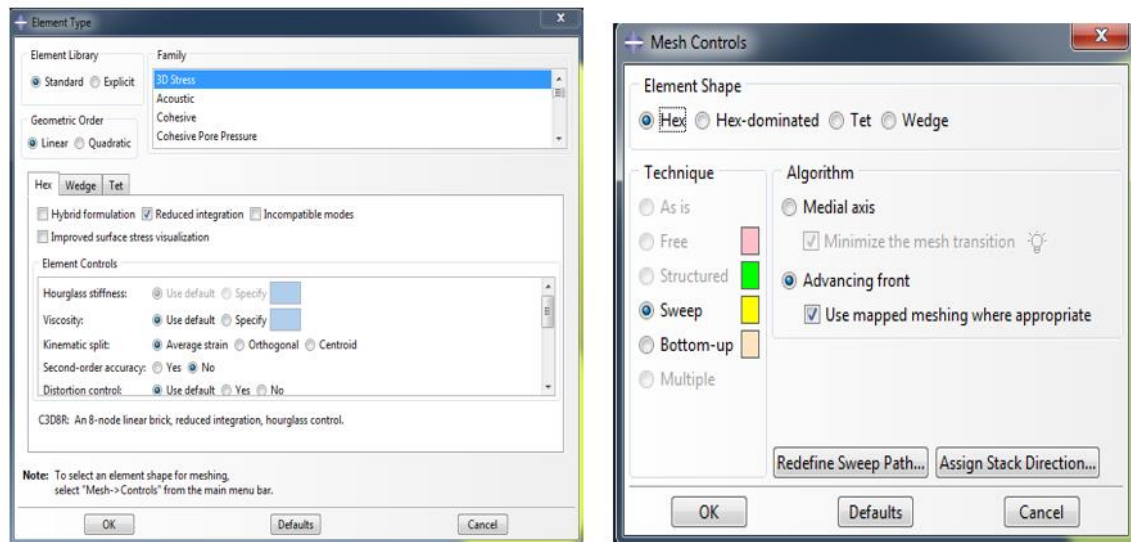


Figure 1.22 ABAQUS Mesh library and control

According to the Simulia 2018 [80], ABAQUS, several geometrical can be meshed using automatic mesh generation by hexahedron elements as shown in Figure 1.23 [80]. Otherwise ABAQUS will generate free form mesh with tetrahedron elements as default. To solve this problem, it is required to decompose the geometry into structural meshable shapes as shown in Figure 1.24. Usually a lot of tedious manual partitioning processes known as geometric decomposition are required as shown in Figure 1.24 [80].

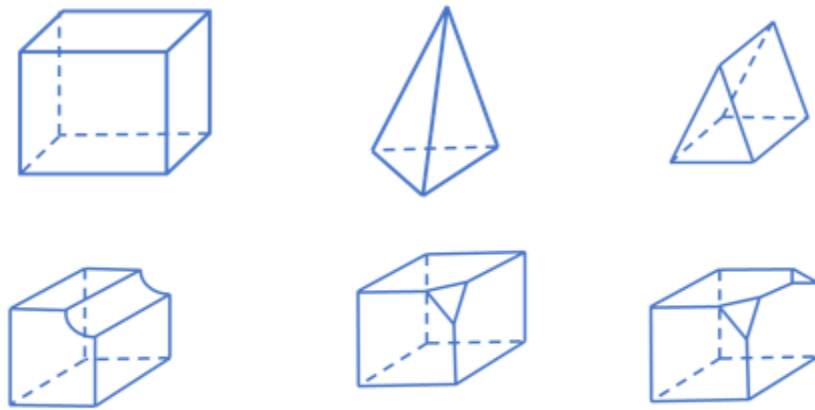


Figure 1.23 Regular shapes structural meshable by ABAQUS

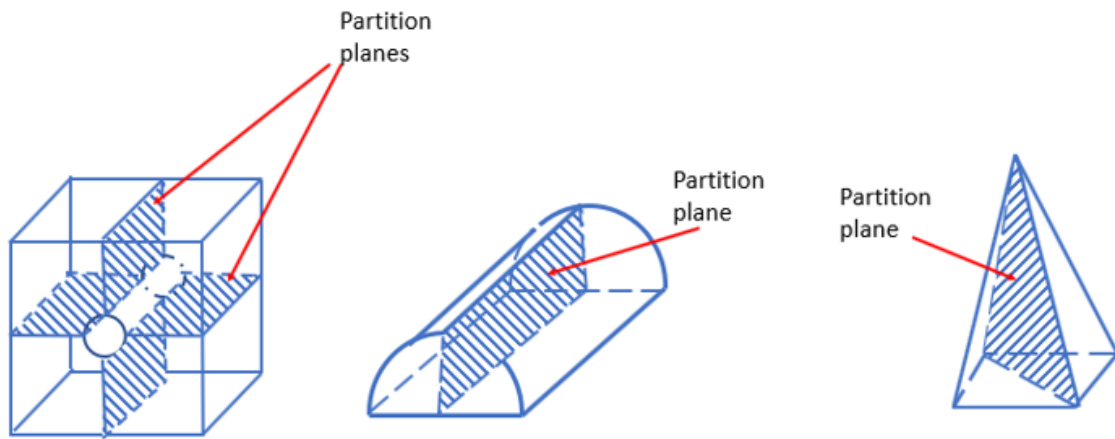


Figure 1.24 Geometric decomposition

1.2.4.4 Properties of 3D Printed Materials

According to many researchers, the properties of 3D printed materials are influenced by many factors. Cantrell, et al., 2016 and Zou, et al., 2016 [85, 86] have tested

and studied the effects of the printed orientations to the mechanical properties. Experimentally it has been proven that the orientation does not affect the Young's modulus and Poisson's ratio, whereas it shows anisotropy when comparing ultimate strength, strain at failure and strain energy density of the printed part [85- 87]. The most effect appears at the shear yield and shear modulus. Because the 3D printed materials are made layer by layer, the behaviors will be anisotropic [86, 88] . The 3D printed materials can be assumed isotropic when neglecting the orientation; however, for increasing precision of measuring the properties, the anisotropic properties can be taken into account [85-87]. For example, Smith and Karmooz [55, 57] assumed the material as isotropic for the models, and they obtained reasonable results.

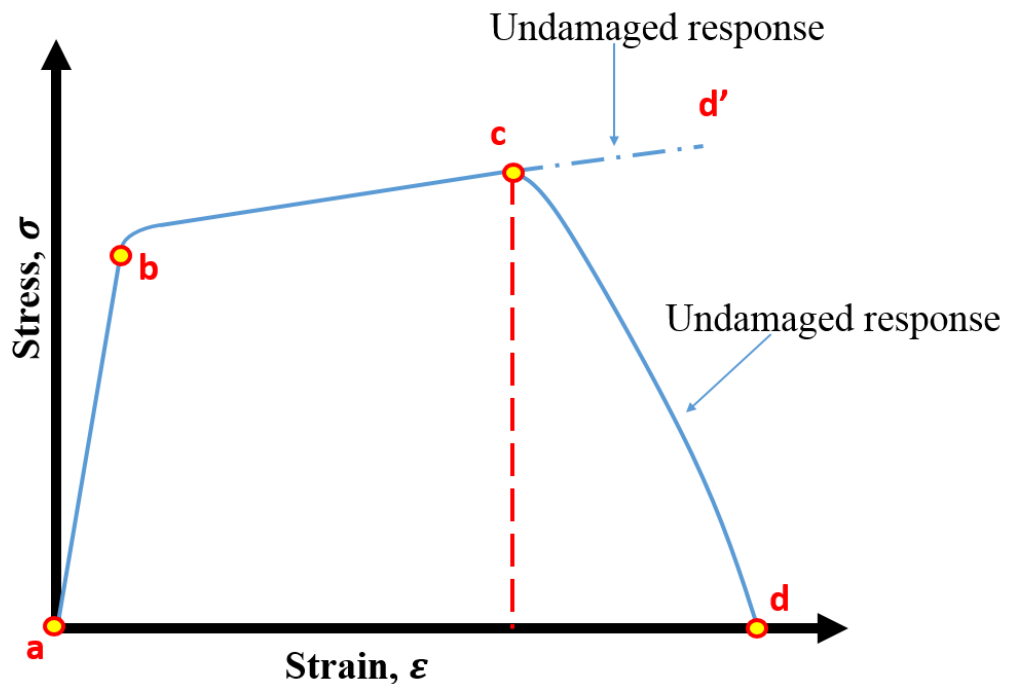


Figure 1.25 Material properties along with the damage criteria adopted for the finite element models [80, 89]

The material properties required to choose appropriate material model in FEM is shown in Figure 1.25. According to the figure, the elastic stage can be captured at part (a-b) [58, 60, 80, 90, 91]. The Young's modulus and Poisson's ratio are required for isotropic linear elastic materials. The plastic stage can be captured based on (b-c) that requires the plastic strain and yield stress [80]. The progressive damage criteria, the part (c-d) is to be defined and logged based on the appropriate damage criteria identified through experiment.

1.2.4.5 Progressive Damage Criteria and Modeling in FEA (ABAQUS)

According to Hooptra and Gese 2004 and Simulia 2018 [69, 80] , there are two types of damage initiation such as ductile damage and shear damage that can be specified [69, 80]. For the ductile damage, it is required to identify the stress triaxiality, fracture strain and strain rates [92] . The stress triaxiality is the main factor to describe the plastic strain that material may undergo before ductile failure occurs [69, 92] . Moreover, the FEM software is able to integrate the damage behavior for both the ductile and shear damage [80] . To specify the ductile damage, it is required to identify the fracture strain, stress triaxiality η , and strain rates $\dot{\epsilon}$ [80] . The fracture strain can be computed according to the stress-strain curve. The stress triaxiality can be determine from equation (1.2) [80].

$$\eta = -\frac{p}{q} = \frac{-1/3 (\sigma_1 + \sigma_2 + \sigma_3)}{q} \quad (1.2)$$

Where η is the stress triaxiality, p is hydrostatic pressure, and q is the von Mises stress, and $\sigma_1, \sigma_2, \sigma_3$ are the principal stresses such that [80]

$$\sigma_1 \geq \sigma_2 \geq \sigma_3$$

It has been shown in many studies that the stress triaxiality ranges between

$$-\frac{1}{3} \leq \eta \leq \frac{2}{3}$$

According to Hooputra, Gese, Dell, & Werner, 2004; Sy, 2009; Kayode, 2011 [69, 73, 74], the curve of stress triaxiality and plastic strain can be divided into 3 regions as shown in the following Figure 1.26. They are high stress triaxiality (1/3 to 2/3), intermediate stress triaxiality (0 to 1/3), and negative stress triaxiality that is identified from the compression test (-1/3 to 0).

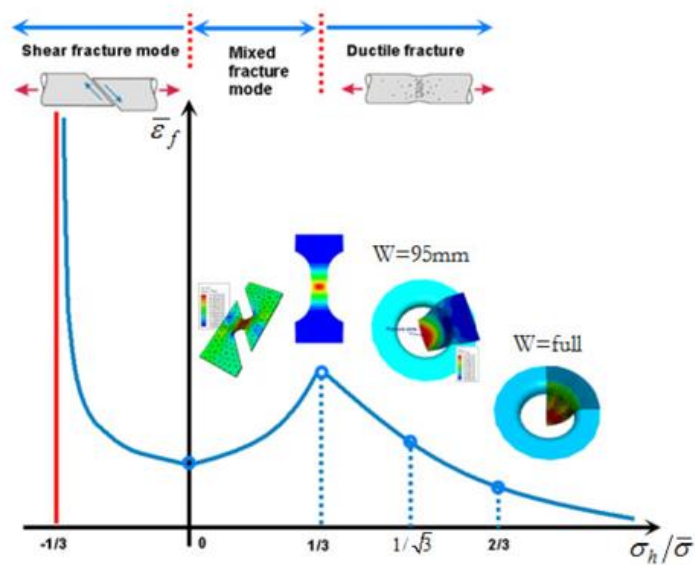


Figure 1.26 Full range of stress triaxiality vs equivalent strain [69]

This model predicts the onset of damage due to shear growth [69, 80]. The model assumes that the equivalent plastic strain at onset of damage $\bar{\epsilon}_s$ is a function of shear stress ratio and strain rates $\bar{\epsilon}_s(\theta_s, \dot{\epsilon})$.

where

$$\theta_s = \frac{q + k_s p}{\tau_{max}} \quad (1.3)$$

Where θ_s is the shear stress ratio, p is hydrostatic pressure, and q is the Mises stress, and k_s is the material parameter [80] . The criterion for damage initiation is met when the following condition is satisfied equation (1.4):

$$\int \frac{d\bar{\epsilon}}{\bar{\epsilon}_s(\theta_s, \dot{\bar{\epsilon}})} = 1 \quad (1.4)$$

The approximation method developed by Gese and Hooputra [69] , can identify the values for the stress triaxiality and shear ratio according to the equivalent plastic strain. It used to predict the damage according to ductile and shear fracture which can be applied to the lattice structure.

1.2.4.6 Ductile Fracture Model by Hooputra and Gese Approach

For the plane stress condition, the equivalent strain to fracture is assumed to depend only on the stress triaxiality. Hooputra et al have given simplified analytical expressions, the equivalent plastic strain is given in the following function of the stress triaxiality and strain rates [69] :

$$\bar{\epsilon}_d(\eta, \dot{\bar{\epsilon}}) = \frac{\epsilon_T^+ \sinh[k_d(\eta^- - \eta)] + \epsilon_T^- \sinh[k_d(\eta - \eta^+)]}{\sinh[k_d(\eta^- - \eta^+)]} \quad (1.5)$$

Where ϵ_T^+ and ϵ_T^- correspond to the equivalent plastic strain at ductile damage initiation for equi-biaxial tensile and equi-biaxial compressive deformation, respectively.

For isotropic yield rule, the stress triaxiality in equi-biaxial tensile deformation state, η^+ , is $2/3$, equi-biaxial compressive deformation state, η^- , is $-2/3$.

For the 3D condition the stress triaxiality η is no longer unique. An additional parameter used to describe the stress state is the ratio $\tilde{\sigma} = \sigma_1 / \bar{\sigma}$ of the first stress and von Mises equivalent stress. Ductile fracture occurs only if the first principle stress σ_1 is positive [69].

1.2.4.7 Shear Fracture Model by Hooputra and Gese Approach

In the shear dominated zone, the fracture strain is postulated to depend both on the hydrostatic and deviatoric state of the materials [69].

$$\bar{\varepsilon}_f^s = d_0 e^{-c\theta_s} + d_1 e^{-c\theta_s} \quad (1.6)$$

Where c , d_0 , and d_1 are three material constants, the new fracture parameter, θ_s , is defined by:

$$\theta_s = \frac{\bar{\sigma}}{\tau_{max}} (1 - 3k_s \eta) \quad (1.7)$$

And the maximum shear stress can be identified by [91, 90]:

$$\tau_{max} = \frac{\sigma_1 - \sigma_3}{2} \quad (1.8)$$

Because θ_s depends on the stress triaxiality and ratio τ_{max}/σ_e , it can be used for both plane stress-strain and general 3D stress conditions. Also, it gives a simplified analytical expression of the equivalent plastic strain for shear fracture with respect to θ_s is given as the following [69]:

$$\eta \bar{\varepsilon}_s(\theta_s, \bar{\varepsilon}) = \frac{\varepsilon_s^+ \sinh[k_d(\theta_s - \theta_s^-)] + \varepsilon_s^- \sinh[k_d(\theta_s^+ - \theta_s)]}{\sinh[k_d(\theta_s^+ - \theta_s^-)]} \quad (1.9)$$

Where ε_s^+ and ε_s^- corresponding to the equivalent plastic strain at shear damage initiation for equi-biaxial tensile and equi-biaxial compressive deformation, respectively.

The parameters θ_s^+ and θ_s^- corresponding to the value of θ_s at $\eta = \eta^+$ and $\eta = \eta^-$ respectively. The value of θ_s can be corresponding to the ranges of values [69] :

$$\begin{cases} \theta_s = \frac{\sqrt{24}(3k_s\eta - 1) - \sqrt{3}\eta\sqrt{4 - 9\eta^2}}{9\eta - 2 - \sqrt{3}\eta\sqrt{4 - 9\eta^2}} & \text{for } 0 \leq \eta \leq 0.33 \\ \theta_s = \frac{\sqrt{24}(3k_s\eta - 1) - \sqrt{3}\eta\sqrt{4 - 9\eta^2}}{9\eta - 4 + \sqrt{3}\eta\sqrt{4 - 9\eta^2}} & \text{for } 0.33 \leq \eta \leq 0.67 \end{cases} \quad (1.10)$$

The model was clearly developed for industrial applications but involves seven degrees of freedom. The shear fracture model acknowledges the joint effect of stress triaxiality and the deviatoric state through the definition of parameter θ_s . Both fracture models are based on a fracture locus of the equivalent plastic strain and stress triaxiality η . In case of linear strain, this function can be used directly as fracture criterion [80]. However, in cases of nonlinear strain it is necessary to use the following equation [69]

$$\int_0^{\bar{\varepsilon}^f} \frac{d\bar{\varepsilon}}{\bar{\varepsilon}_s^f(\eta)} = 1 \quad (1.11)$$

1.2.4.8 Damage Evolution and Fracture Criteria

For damage in ductile materials, ABAQUS/Explicit assumes that the degradation of stiffness associated with each active failure mechanism can be modeled using a scalar

damage variable. During the analysis the stress tensor in the material is given by the scalar damage equation [80] as in equation (1.12)

$$\sigma = (1 - D)\bar{\sigma} \quad (1.12)$$

where D is the overall damage variable and $\bar{\sigma}$ is the effective (or undamaged) stress tensor computed in the current increment, σ is the stress that would exist in the material in the absence of damage. As shown in the Figure 1.27, the damage at D is with respect to the yield stress σ_y and equivalent plastic strain $\bar{\epsilon}$ [80]. The overall damage variable reaches the value $D = 1$ at $\bar{\epsilon}_f$, is the equivalent plastic strain at failure and the material has lost its load carrying the capacity. The value of the equivalent plastic strain at failure, $\bar{\epsilon}_f$, depends on the characteristic length of the element and cannot be used as a material parameter for specification of the damage evolution law. Instead, the damage evolution law is specified in terms of equivalent plastic displacement, \bar{u}^{pl} , or in terms of fracture energy dissipation, G_f . By default, an element is removed from the mesh if all of the section points at any one integration location have lost their load- carrying capacity [80].

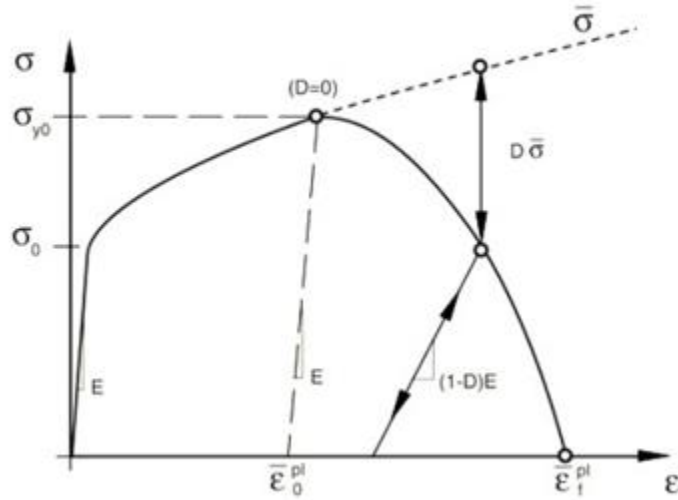


Figure 1.27 Characteristic stress-strain behavior of progressive damage [80]

1.2.5 Specific Energy Absorption

It is very important to understand the relation between the process and material properties [93]. The main aim of the impacting test is to see the effectiveness of the design to the dynamics deformation [93]. It is recommended to do the test in terms of optimizing the geometrical shapes [93]. The Specific energy absorption (SEA) and specific energy efficiency (SEE) are used to measure the feasibility of the design through an impact test [93]. For this reason, the energy absorption is considered the main aspect for the successful design of any lattice configuration [1]. For example, aerospace and marine applications require energy absorption components which can absorb the dissipated energy during uncertain stages of unintentional overloads. The most important indicator of the energy absorption is to calculate the energy per unit mass [94]. This value is called Specific Energy Absorption (SEA), and it can be expressed as:

$$SEA = \frac{W}{m} = \frac{\int F dx}{m} \quad (1.13)$$

where F is the applied load, x is the displacement, and m is the mass of the component [95, 96, 97].

According to the equation 1.13 it is necessary to increase the mass terms of reducing the SEA. Since most of the application is supposed to be impacted, the impact test will be used to determine the optimal configuration based on the Specific Energy Absorption (SEA).

1.2.6 Progressive Damage Mechanism

According to Ashby and others, there are three possible collapse regions. The Gibson model is defined by dividing the micro-mechanical structure of lattice into 3 regions: linear elastic, plateau region, and densification [98, 99] . However, because the Gibson model includes the density, the drawback of the Gibson model is with detailed information on the microstructure of a foam structure [98] . In overall, Gibson and Ashby have summarized the stages of the lattice failure into three stages. Linear elastic, Plastic collapse (Plateau stress), and densification regime as shown in the Figure 1.28 [100, 101]. Therefore, it is necessary to find model to understand the relation between the cellular topologies and the mechanical responses.

Over 20 years, many different fracture models have been developed and three main aspects of fracture such as structure, material constitutive equations, and better numerical control have been investigated [102, 103]. Numerical simulation is preferred for these studies more than the experimental for many reasons such as low cost, and practicable

outcome [102]. For this reason, the numerical analysis is used to compare deformation mechanism and mechanical property against observed during experimental work. However, in terms of getting higher accuracy, the higher order of the formulation and small-time frame for computation can improve quality of the results [104] . The numerical model has helped to observe how the Young's moduli and the mechanical properties can vary or change due to the influence of the topologies and boundary conditions [13] . Because modeling of the fracture is very sensitive to the elements, the elements formulation has to be chosen and validated carefully [105, 106] . Also, the mesh orientation has to be taken into account. The effect of the crack pattern also impacts the resolution of the simulation [106, 107]. It was proven that the brick elements are more efficient than the tetrahedral elements for many reasons, including higher degree of freedom, higher degree of the formulation [22, 82] .

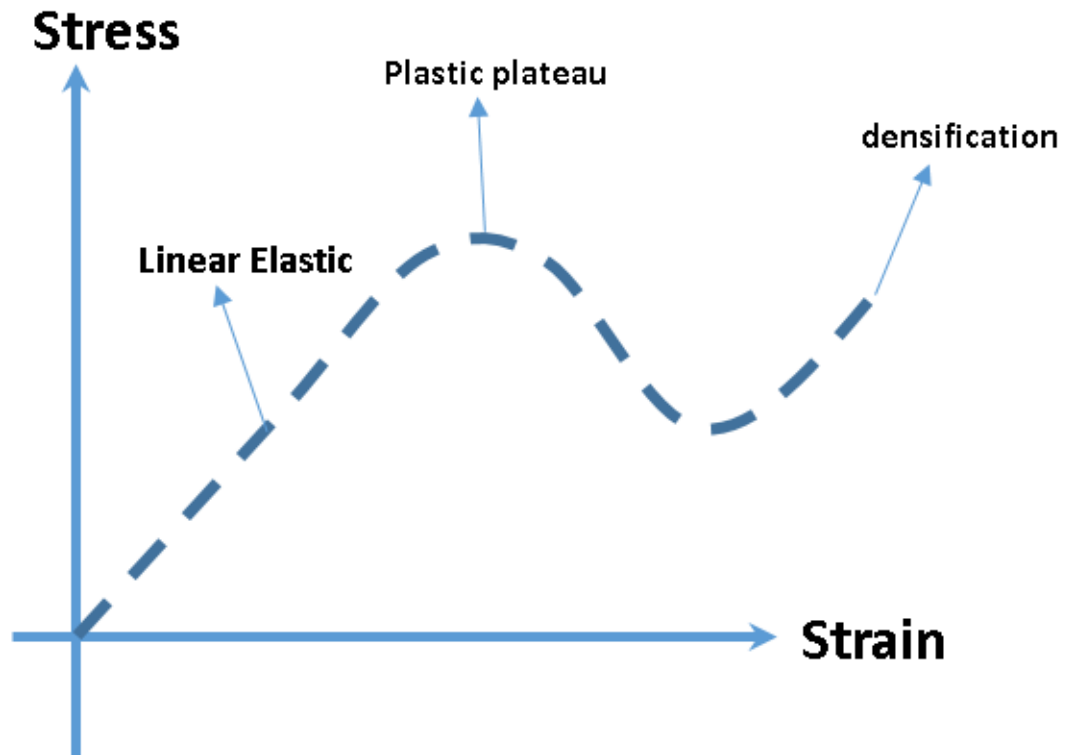


Figure 1.28 Ashby and Gibson failure stages for the lattice form [7].

1.2.7 Additive Manufacturing (AM)

Additive manufacturing (AM) has helped to rapidly develop and manufacture a variety of complex geometrical designs of the lattice structure [93]. It also helps to raise process capabilities and lower the cost of testing [22, 93]. The AM has been enhanced to fabricate metallic cellular materials [5, 22, 25, 37, 52, 63, 93]. The selective laser melting (SLM) method has allowed AM of metals including stainless steel, and titanium alloys [3, 93]. By using SLM, designers have a higher degree of flexibility to design the parts. The SLM is stable enough to create the cellular parts with micrometer range [64]. Moreover, many complex configurations have been made by additive manufacturing (AM) which is 3D printing technology [85, 86, 93]. The most common 3D printing technique is fused

deposition modeling (FDM). It works with heated nozzles extruding molten polymer layer by layer [85, 86] . 3D printing has been widely used to create a variety of complex configurations [85, 86, 96, 108]. However, the processes of fabricating the specimens by 3D printing is costly in materials and time in some cases.

1.3 The Research Scopes

In this dissertation, the work focuses mainly to develop an effective FEM based computational modeling scheme and apply it to investigate the effect of different designs of the periodic LCS. This model will be validated according to the previous experimental results. The LCS configurations used in this were BCC family, Tetra family, and Pyramidal with distributed vertical and horizontal struts. The model will be first developed for ABS polymer, and it will be subsequently expanded for any other possible printed materials. The ASHBY model for progressive damage will be used to evaluate the feasibility of the design. Therefore, the finite element model of this research can be used to predict the behaviors of the different struts diameters and different cell dimensions in the LCS.

1.3.1 Problem Statements

Additive manufacturing (AM) helps to rapidly develop and manufacture a variety of complex geometrical designs and structures, including an LCS [93 , 96 , 108]. However, the processes of fabricating using additive manufacturing is costly in materials and time. Finding optimal and best geometrical design using computational methods, which is fast and less expensive, is a good area of research.

- There is a lack of study on the mechanical properties for the 3D printed lattice polymer such as stiffness, strength, and elasticity modulus.

- Even though several studies have covered FEM in elastic-plastic stages, there is a lack of modeling beyond the plastic limits.
- Creating efficient finite element models for the lattice structure to capture the post-yield behavior and progressive damage is limited especially for the polymetric lattice structure.

1.3.2 Dissertation Goals

The objective of the study is to develop a FEM scheme to efficiently create and run periodic LCS under different loading conditions, especially, under compressive and impact loads. This model will be validated and tested based on the experimental data. The main difference between this study and previous studies is its emphasis on using FEM to analyze different types of periodic LCS with different parameters such as cell and lattice dimensions and materials. This software will help to study and optimize the best lattice structure design. The essential objectives of this dissertation are to:

- (i) Develop finite element model by commercial finite element software ABAQUS for all the configurations and then use it to investigate the behavior through the elastic-plastic deformations due to the quasi compression tests.
- (ii) Create numerical model to investigate different effects under a low velocity impact tests.
- (iii) Create a numerical model to capture the post-yield stages of the lattice structure in the compression test and validate the model with the experimental data from the previous studies.

- (iv) Create user friendly GUI for ABAQUS plugin tool hereby called as the lattice structure designer (LSD) so that any periodic LCS can be generated, modeled, and run by users with no high-level knowledge.
- (v) Install the LSD tool developed in the part (iv) in ABAQUS and validate it with different types of the lattice structures.
- (vi) Based on the LSD results from the part (v), analyze and evaluate the relation between the topology and the post-yield behaviors.

1.4 The Dissertation Outline

Chapter 1: Literature Review

Chapter 2: The Finite Element Model (FEM). This chapter will cover how to model the different LCS by using the commercial FEM software ABAQUS, how to identify optimal mesh convergence, incorporate material properties, fracture criteria, etc. using tetrahedron or hexahedron mesh, and linear or quadratic mesh. The FEM modeling scheme will be validated through the experimental findings by WSU researchers.

Chapter 3: ABAQUS GUI. This chapter will discuss the development of python code with ABAQUS as GUI for the plug-ins and its role in improving the FEM to capture the results beyond the plasticity limits of the sample.

Chapter 4: The LSD application and validations. This chapter is to discuss how to install LSD and apply with different types of the lattice structures. Also, discuss validating the LSD results with previous experimental works.

Chapter 5: BCCV and TetH models Post-yield: Analyze and discuss the fracture mechanisms and evaluating based on the energy absorption efficiency and plateau stress.

Chapter 6: Recommendations for Future Work

Appendices:

Appendix A: Debugging the BCC with Geometric Decomposition

Appendix B: Assigning the Ti-6Al-4V Alloy Debugging

Appendix C: Assigning Undefined Materials Debugging

Appendix D: Assigning the Boundary Conditions

Appendix E: Assigning the Mesh

Appendix F: Assigning the Job

Chapter 2. The Finite Element Modeling of the Lattice Cell Structure

2.1 Overview

Because ABAQUS 6.16 Explicit CAE 2016 has the ability to simulate static and dynamic systems involving complex geometrical parts' features, it will be used to investigate four types of the sandwich structure configurations. As mentioned before, the models are designed by SolidWorks and exported to ABAQUS/CAE via the tool of SolidWorks Associative Interface. This tool provides immediate connection between ABAQUS/CAE and SolidWorks as shown in Figure 2.1. It is easy to change the dimensions and design through SolidWorks and, consequently, the model will be upgraded in ABAQUS/CAE. However, the tetrahedron elements are the only choice of mesh that can be generated by ABAQUS using free mesh technique for these models.

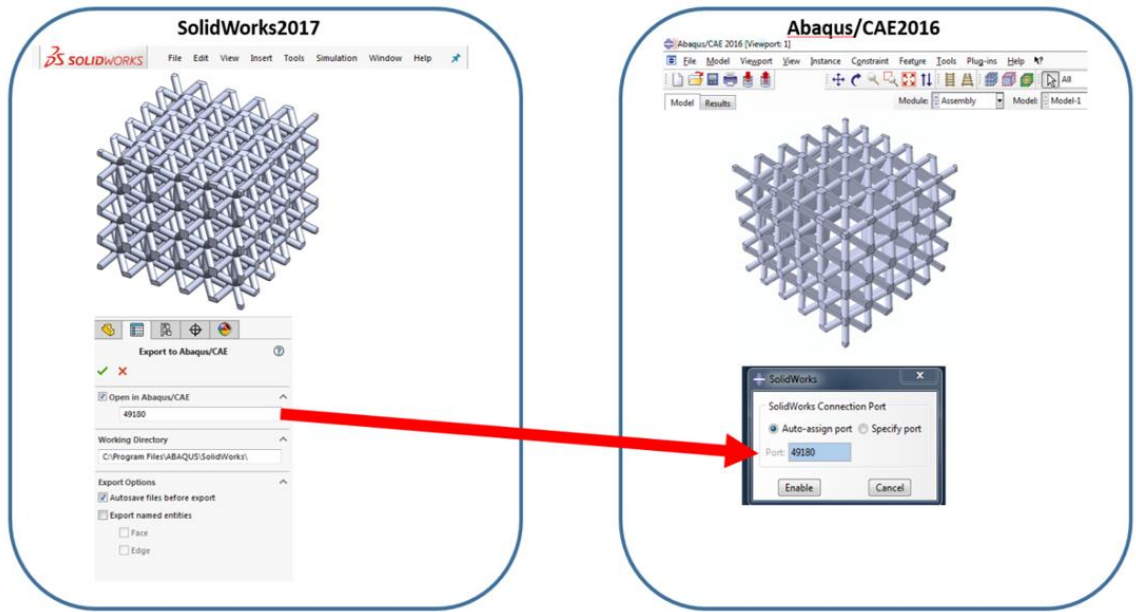


Figure 2.1 SolidWorks Associative interface tool to ABAQUS/CAE

2.2 Mesh Generation

Identifying the optimal mesh is necessary to provide better results due to the sensitivity of the FEA models on mesh size and type. It was found that the model only accepts the Tetrahedron mesh (element type C3D4) because of the complexity of the geometrical shape as shown in Figure 2.2 (a). Subsequently, the optimum number of the elements are identified according to the mesh type C3D4 [80]. To determine the optimum element size, the model is first run with the default number of elements and observed the maximum displacement and the force. The model was then rerun many times with different numbers of the elements until convergence. Figure 2.2 (b) shows the number of the mesh vs. yielding force for the BCC configuration. It is observed that the minimum number of elements was 550,000 elements beyond which the yielding force does not change. The next

parameter to be identified is the optimum value of mass scaling factor to minimize the computational time [65, 80, 89, 109]. The mass scaling is a factor to control the incrementing of the time based on the density of the specific elements. Thus, the mass scaling is useful to reduce the computational time. In the same way, the mass scaling was identified by rerunning the model and observing the maximum displacement until the convergence is satisfied as shown in the Table 2.1.

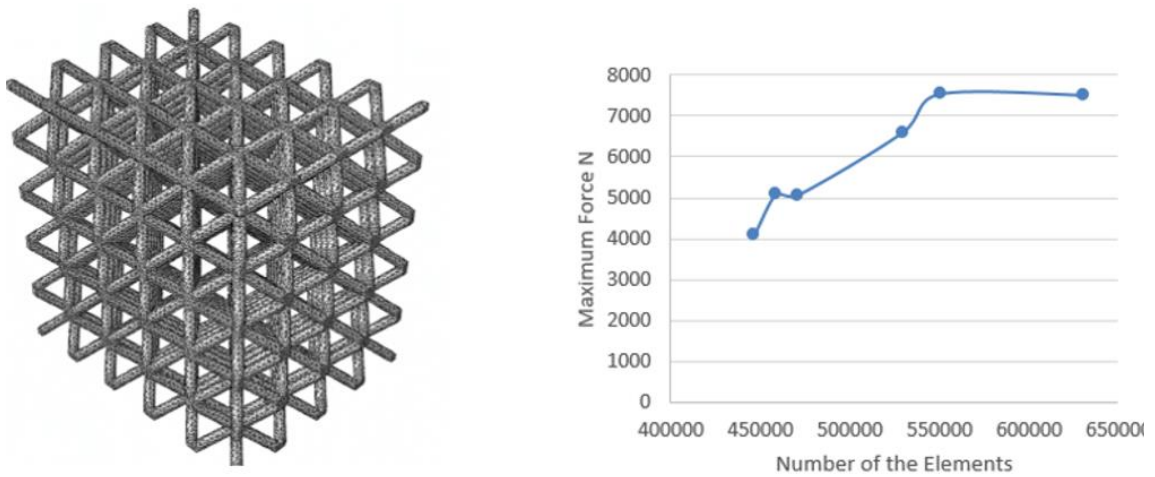


Figure 2.2 (a) Lattice structure with tetrahedron mesh, and (b) The convergence curve

Table 2.1 the convergence of the maximum displacement due to the time scaling value

Time scaling value	Maximum displacement	Time scaling value	Maximum displacement
0.01	2.560	1E-6	7.221
0.001	5.02	1E-7	7.786
0.0001	6.112	1E-8	7.795
1E-5	6.850	1E-9	7.801

2.3 Material Properties

For all the FEA simulations, ABS was modeled with an elastic plastic failure mode with ductile and shear damage criteria. All the properties were identified experimentally for the printed material. A sample with ASTM 632 [110] was printed and tested under tensile loading. All the mechanical properties have been identified based on the tensile test result which is shown in Figure 2.3.

The density and Poisson's ratio of the sample were identified as 792 kg/m^3 and 0.35, respectively [89, 109]. The mechanical properties, such as modulus of elasticity, plasticity, yield point, and failure strength were experimentally measured using separate tensile and compressive tests of the printed samples. The mechanical properties which are used for all the FEA simulations are shown in Table 2.2 for the ABS material printed using the uPrint printer.

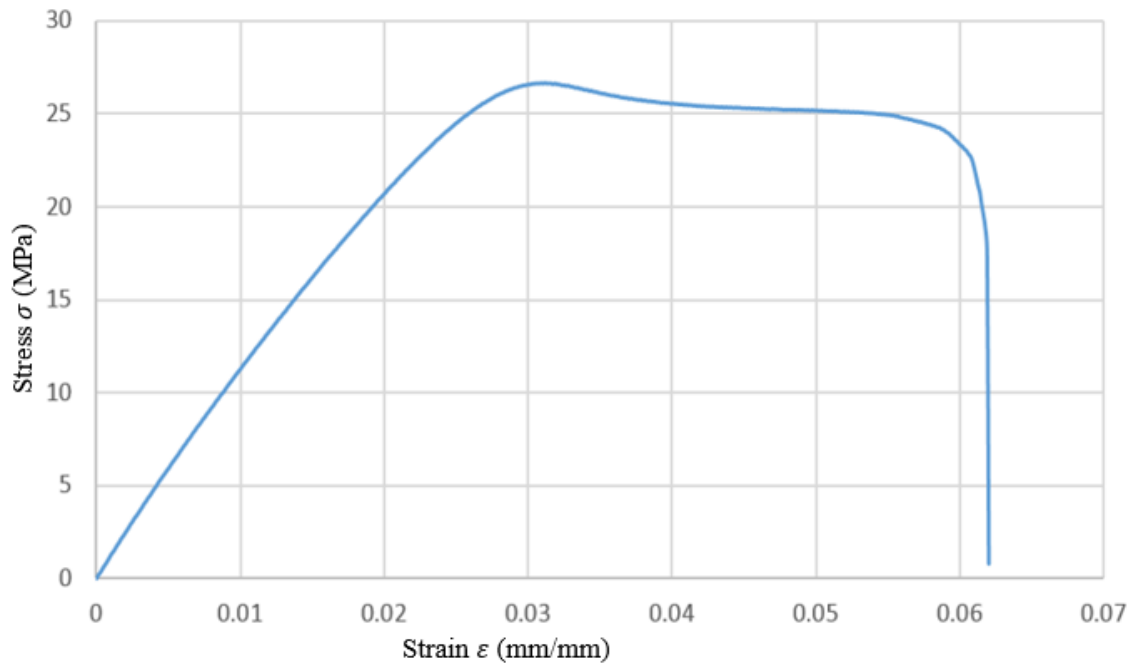


Figure 2.3 Experimental ABS stress strain for the tensile test

Table 2.2 Printed polymeric ABS properties

The Young modulus (MPa)	The Yield Strength (MPa)	The plastic strain	ultimate failure strength (MPa)
861.5	25.77	0.0455	33.32

2.4 The Fracture Criteria

As mentioned in sections 1.2.4.6 and 1.2.4.7 and according to Simulia [80], the stress triaxiality and equivalent plastic strain were calculated, and these values were logged in ABAQUS as shown in Figure 2.4 (a). Similarly, to identify the shear damage the shear stress ratio was calculated by the same approach as shown in Figure 2.4(b). The failure due to the buckling is not considered on these models because the slenderness ratio (L/r) is too small and there is no chance for buckling to occur [90].

	Fracture Strain	Stress Triaxiality	Strain Rate
1	0.004849	0	0.016
2	0.005856	0.005368108	0.016
3	0.007548	0.01022973	0.016
4	0.007625	0.012132973	0.016
5	0.008	0.039579459	0.016
6	0.008148	0.063874595	0.016
7	0.008218	0.100517838	0.016
8	0.008243	0.116105405	0.016
9	0.008247	0.119156757	0.016
10	0.008252	0.122176216	0.016
11	0.008257	0.129007568	0.016
12	0.00826	0.146187027	0.016
13	0.008263	0.162915676	0.016
14	0.008268	0.176302162	0.016
15	0.008271	0.194018378	0.016
16	0.008275	0.219813514	0.016

(a)

	Fracture Strain	Shear Stress Ratio	Strain Rate
1	0.004849	2.055555556	0.016
2	0.005856	2.058865889	0.016
3	0.007548	2.061863889	0.016
4	0.007625	2.063037556	0.016
5	0.008	2.079962889	0.016
6	0.008148	2.094944889	0.016
7	0.008218	2.117541556	0.016
8	0.008243	2.127153889	0.016
9	0.008247	2.129035556	0.016
10	0.008252	2.130897556	0.016
11	0.008257	2.135110222	0.016
12	0.00826	2.145704222	0.016
13	0.008263	2.156020222	0.016
14	0.008268	2.164275222	0.016
15	0.008271	2.175200222	0.016
16	0.008275	2.191107222	0.016

(b)

Figure 2.4 (a) Ductile Damage plug in ABAQUS, and (b) Shear Damage plug in ABAQUS

2.5 Model Verification using Tensile Samples

Before any further modeling, it is needed to test the quality of the FEM scheme. This procedure will help to see the capabilities of the simulations in capturing the data numerically. The tensile sample of standard ASTM 3646 was tested first and load-displacement response of three samples were recorded first. The same sample configuration was created and modeled in ABAQUS. In this case, the failure theorems discussed in previous section were logged in ABAQUS. The FEM results were compared with the experimental results as shown Figure 2.5. According to the results, the numerical model and the experimental model are in good agreement. Thus, the model can be developed for further analysis of the lattice structure.

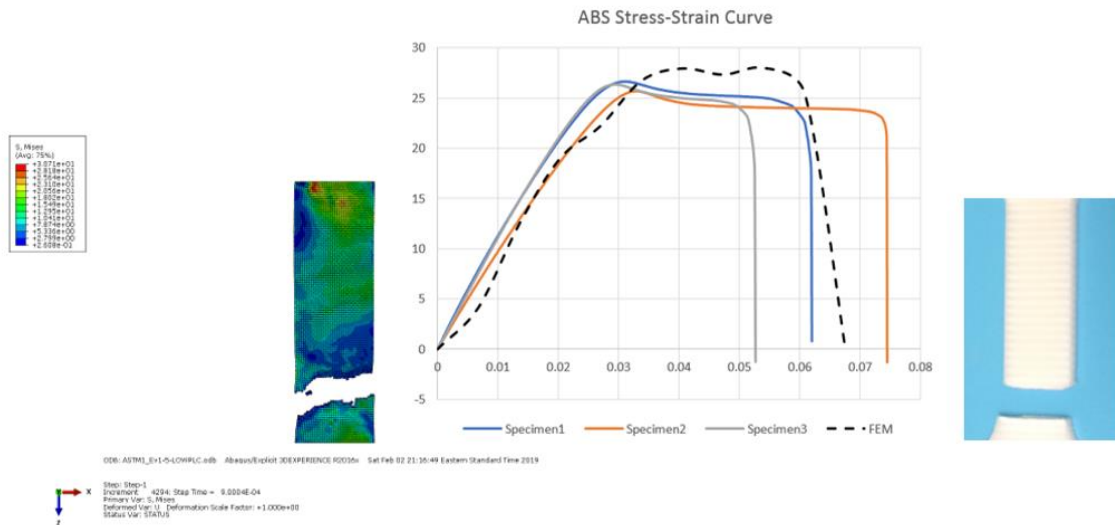


Figure 2.5 Standard ASTM 638 modeling and experimental results comparisons

2.6 Modeling the Compression Tests of LCS

In this section, the validation of FEA modeling for all the four LCS configurations such as BCC, BCCA, BCCV, and BCCG under compression is presented. The validation is done by comparing the experimental load-displacement curve with FEA results. For the FEA models, the clamped-clamped boundary conditions for the top and bottom faces were applied through two extreme unyielding planes, as shown in the Figure 2.6. The bottom plate was fixed while the top plate was displaced downward to match the experimental displacement rate. Also, the maximum applied displacement in FEA simulation was the displacement at first failure observed during experiment.

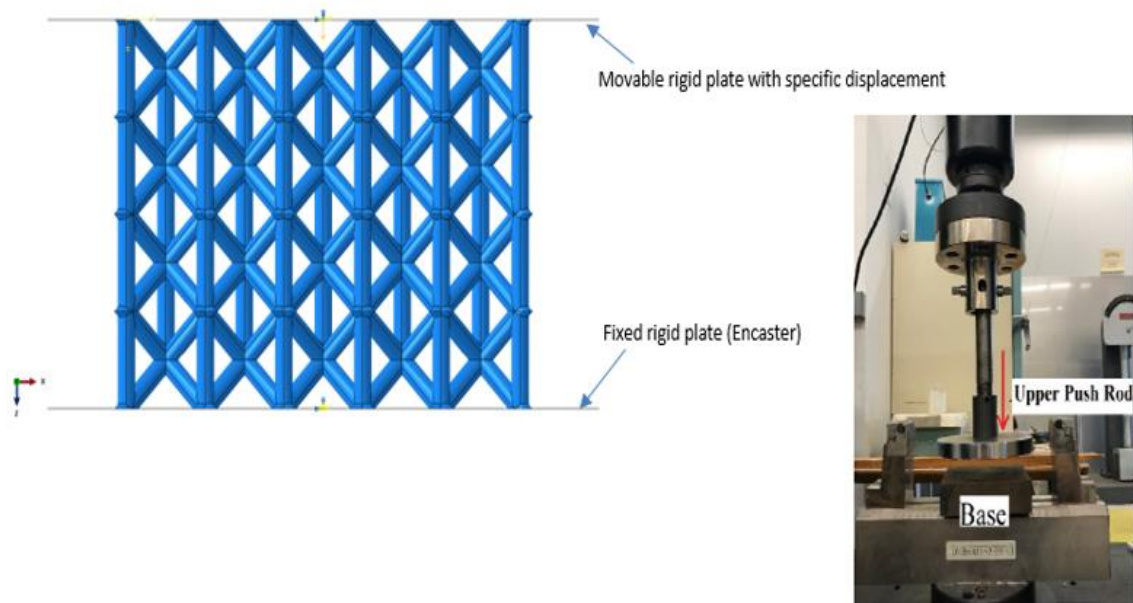


Figure 2.6 Boundary condition assumption for the compression model

Because of the limited capabilities of the tetrahedron elements from capturing the behavior beyond the elasticity stages, the finite element models were done until the first level of collapse. Assuming appropriate boundary conditions plays an important role of effective modeling [89]. As shown in Figure 2.7 the specimens are placed between the

base and upper movable plate during compression testing. Hence, the boundaries were considered to be unyielding rigid plates in FEM with a fixed rigid plate at the bottom surface and movable rigid plate on the top surface as shown in Figure 2.7 [89]. Also, the maximum applied displacement in the FEA simulation was considered to be the displacement at first failure observed during experiment. For example, the first failure for the BCC configuration was observed at a displacement of 1.6 mm (see Figure 2.8 in section 2.7.1). Since explicit finite element modeling was used, the displacement loading was applied through the top rigid plate by moving it down monotonically with the amplitude rate of 0.0002/sec until a displacement of 1.6 mm was reached.

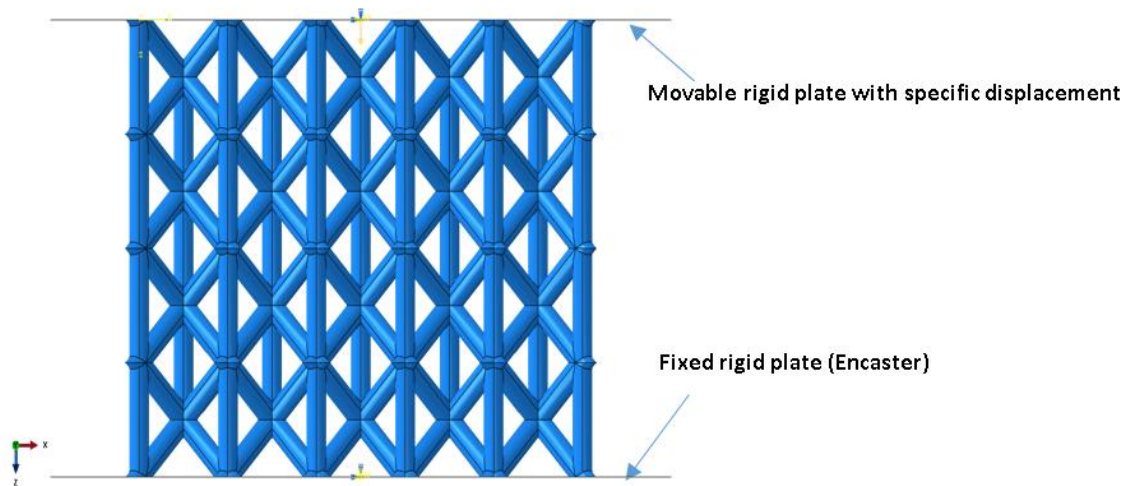


Figure 2.7 ABAQUS Boundary condition applied.

2.6.1 BCC 1st Layer Collapse (Experimental Vs FEM)

Figure 2.8 shows the comparison of load-displacement behaviors of BCC samples obtained from FEM and experiment. The first collapse of the printed sample was captured at 1.6 mm displacement. The finite element model and the experimental model show that

the failure started on the top and bottom layers simultaneously as appeared in Figure 2.8 [89].

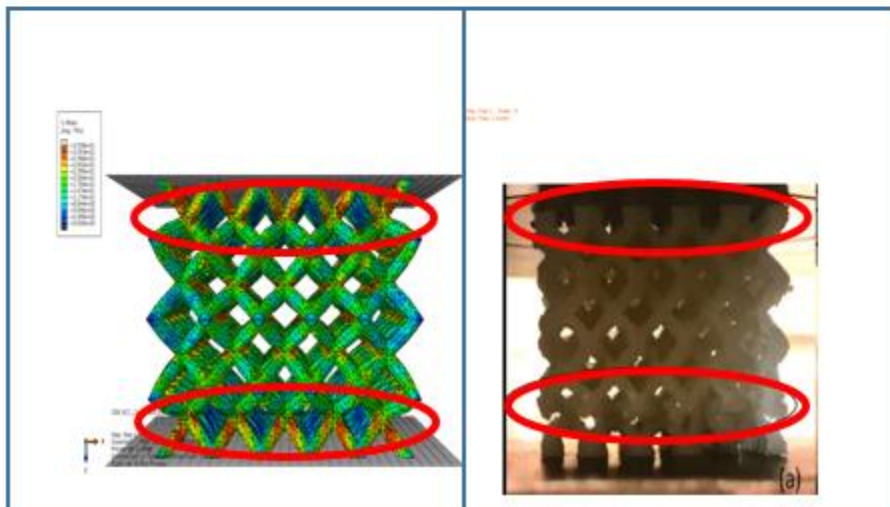
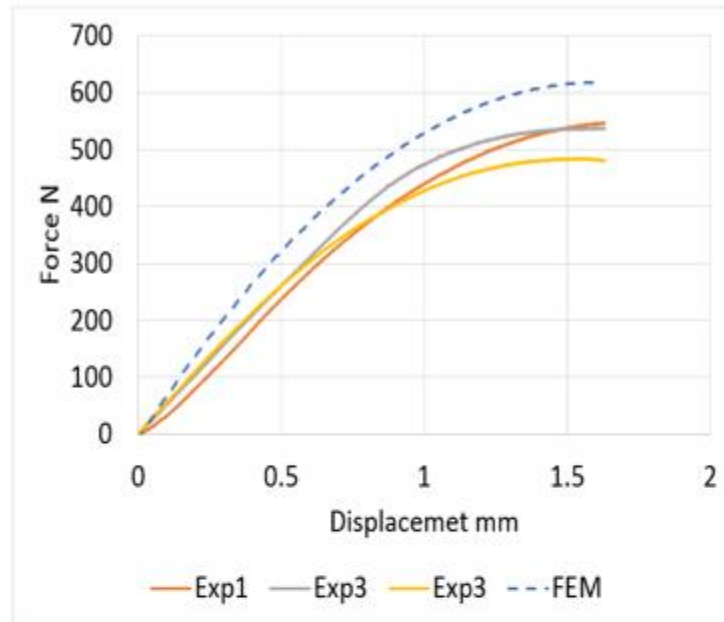


Figure 2.8 BCC modeling simulation and real experimental comparison

2.6.2 BCCV 1st Layer Collapse (Experimental Vs FEM)

For the BCCV, the first collapse was captured at 0.06 mm displacement. The finite element model and the experimental models show that the failure has started in the top layer as shown in Figure 2.9 [89].

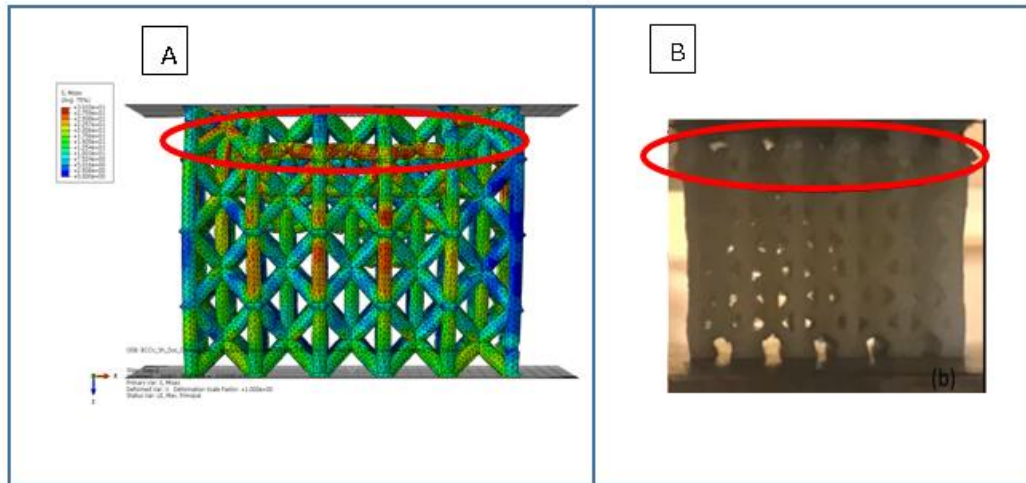
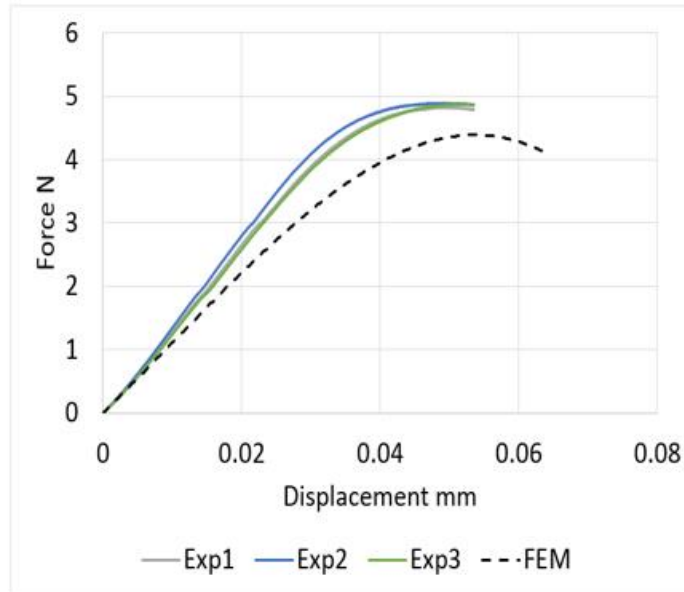


Figure 2.9 BCCV modeling simulation and real experimental comparison

2.6.3 BCCA 1st Layer Collapse (Experimental Vs FEM)

For the BCCV, the first collapse was captured at 1.2 mm displacement. The finite element model and the experimental results show that the failure started on the middle layer see the Figure 2.10 [89].

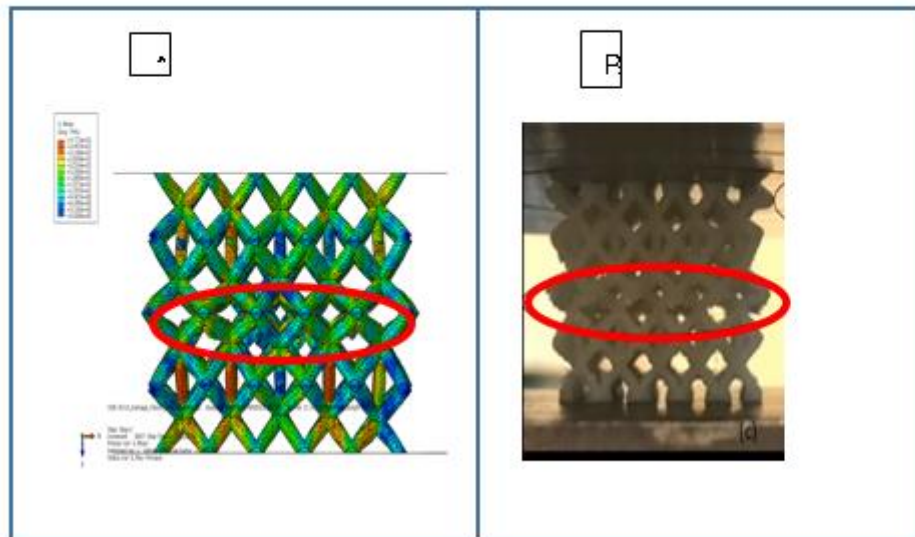
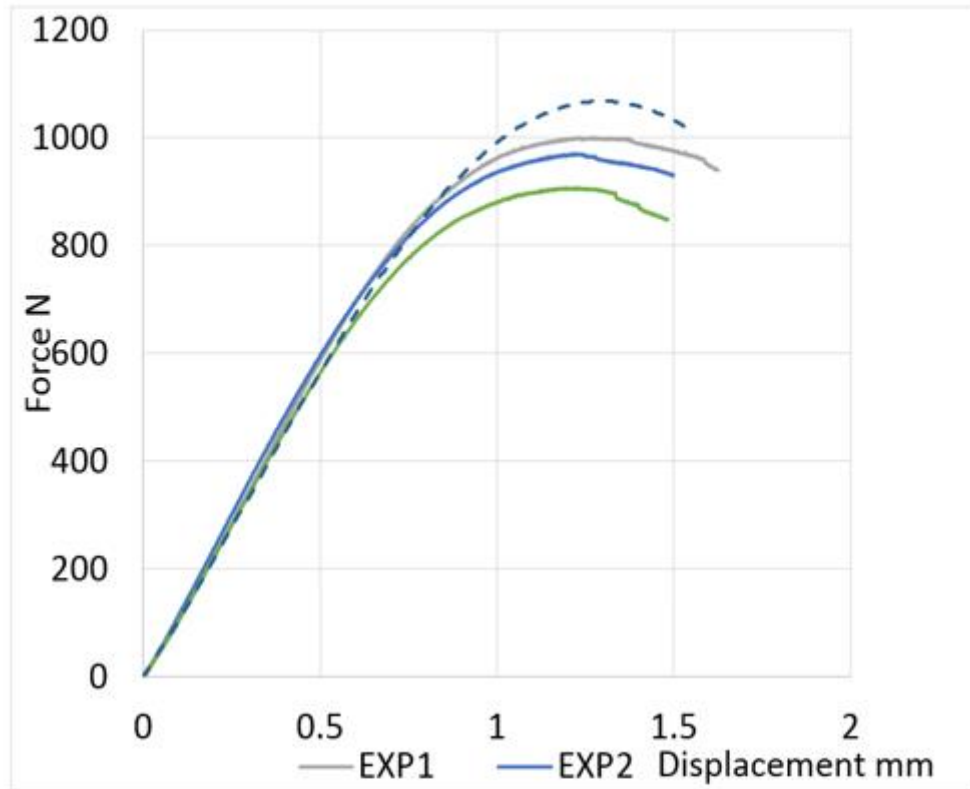


Figure 2.10 BCCA modeling simulation and real experimental comparison

2.7 The Low Velocity Impact Test Modeling Results

Based on Al Rifaie [52] and Turner's [58] experiments, the finite element models have been developed and validated for this application. As was mentioned in section 1.2.2.6, the machine dropped the impactor from a height of 0.6215 m, as a consequence the initial velocity was 3.492 m/sec according to the equation 2.1. Al Rifaie [52] used the mass of 2.436 kg for his impactor, and this mass will correspond the initial kinetic energy of 14.85 Joule according to equation 2.2. To reduce the computational time and increase the efficiency of the models one quarter of the specimen as shown in the Figure 2.12 (a) was modeled. Another reason for this decision was because of the symmetry of the specimen condition, the symmetry boundary conditions in x-direction and y-direction were applied. For example, the symmetry in x-direction leads to $U1=0$, $UR2$, and $UR3=0$. Where $U1$ is the displacement in x direction, $UR2$ rotation about y-axis, and $UR3$ is the rotation about z-axis as shown in Figure 2.11 (b) [109].

$$v = \sqrt{2gh} \quad (2.1)$$

$$KE = \frac{1}{2}mv^2 \quad (2.2)$$

Where g is the gravitational acceleration and $g = 9.805 \text{ m/s}^2$, and h is the drop height.

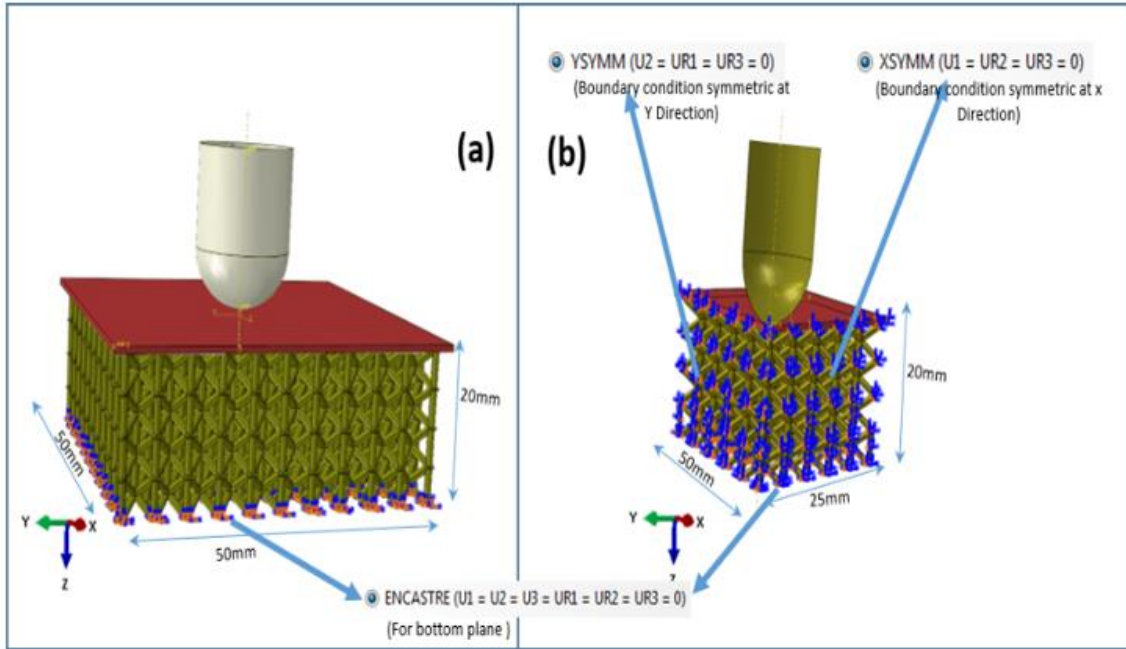


Figure 2.11 (a) Boundary condition of the entire model, and (b) boundary condition for one quarter

2.8 Impact Test Results

The FEM models for the impact test show similarities in the maximum forces and displacements to the experimental specimens [25]. According to both the experimental and FEM results, they have demonstrated a variety of material behaviors and abilities to absorb impact energies.

2.8.1 Finite Element Model for The Impact Test for BCC

The BCC configuration has shown the peak forces during the test between 2200-2700 N with the displacement of 8.1-9.01 mm as shown in Figures (2.12 a,b,c,d). Obviously, because this configuration is less stiff than the others, it provides less peak forces and higher displacement during the impact. Also, it has less reversed velocity between (0.28-1.25) m/sec. This is due to the fact that the BCC has higher damping behavior and can absorb more energy [25].

2.8.2 Finite Element Model for The Impact Test for BCCV

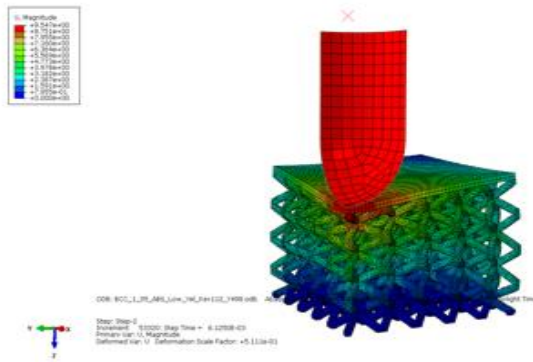
For the BCCV plots as shown in the Figures (2.14 a,b,c,d), the maximum corresponding reaction forces were (3400-4000) Newton with the maximum displacement about (5.8-6.3)mm. The velocity at the time of hitting was 3.491 m/sec while the reversed velocity has reduced to the values of (0.35- 2) m/sec as shown in Figure (2.13 b). This is due to the absorbed energy by the BCCV configuration design [109].

2.8.3 Finite Element Model for The Impact Test for BCCA

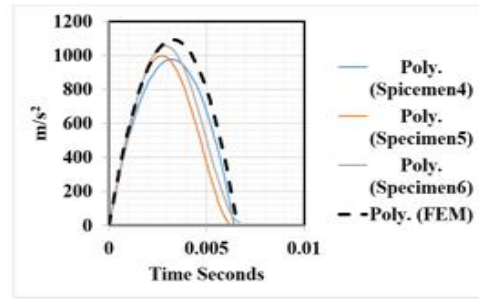
The next configuration was BCCA. It showed the maximum forces between (4500-6800) Newton as shown in Figure (2.14 a,b,c,d) with the maximum displacement about (6.8-7.8)mm.

2.8.4 Impact Specific Energy Absorption (SEA)

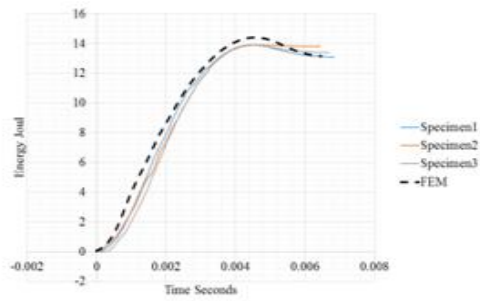
To identify the optimum configuration design, it is important to calculate the Specific Energy Absorption (SEA) [14]. Since the value of SEA is the ratio between the energy to the mass, it is necessary to calculate the energy from the Force-Displacement curves. For example, the BCCV, the energy was calculated by integrating the area under the curve. It was 13.89 Joule and its weight was 21.0 g. Thus, the SEA will be 661.428 J/kg. All the SEA values have been computed and summarized in Table 2.3. According to the SEA plots, it is obvious the BCCV and BCCA have higher SEA values. This implies that both of the BCCV and BCCA have the highest energy absorption against the impact forces. On the other hand, the BCC configurations have the same levels of the SEA even though they are different design. Therefore, mass is not the main factor can affect to the energy absorption rather than the geometrical design.



(a)

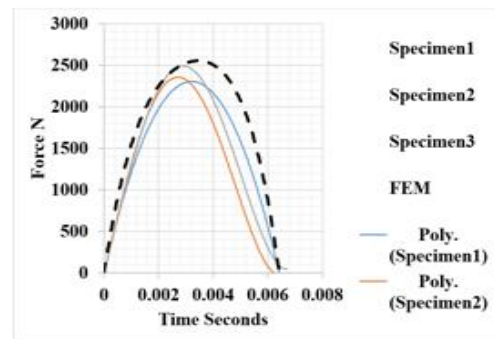


(b)



Energy absorption-time curve for BCC

(c)



(d)

Figure 2.12 BCC impact results experimental and FEM (a) Impact simulation (b) Acceleration-time (c) energy-time, and (d) force-time

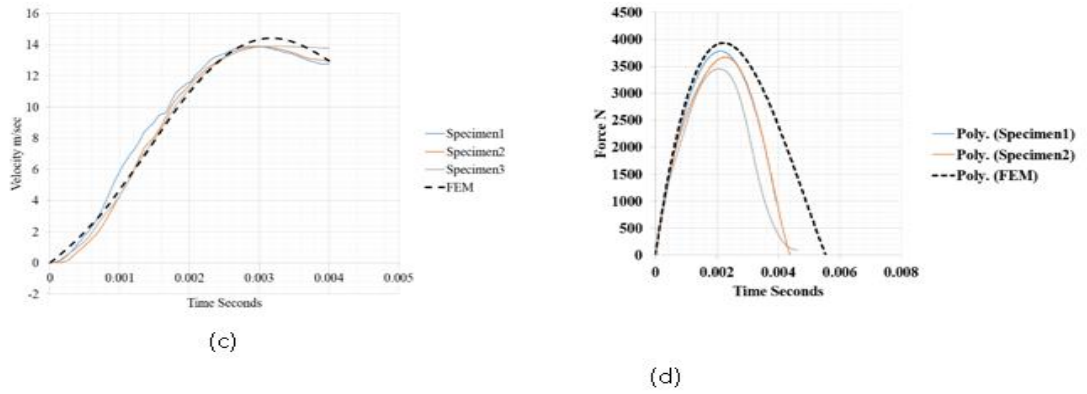
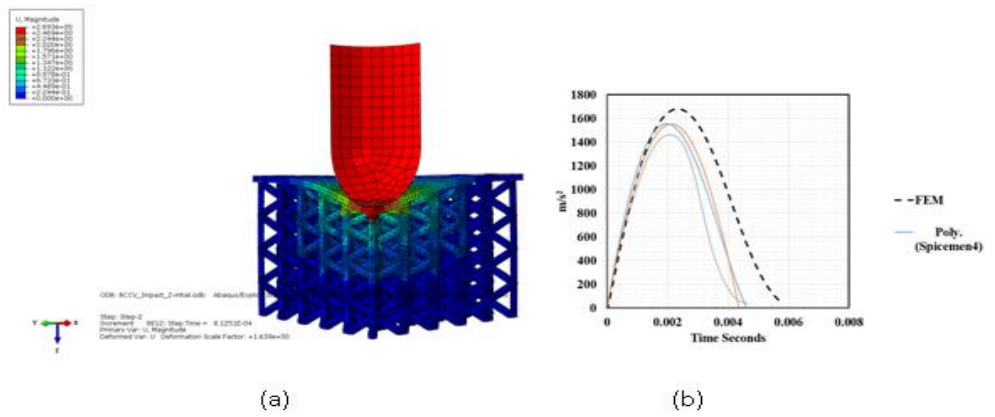


Figure 2.13 BCCV impact results experimental and FEM (a) Impact simulation (b) Acceleration-time (c) energy-time, and (d) force-time

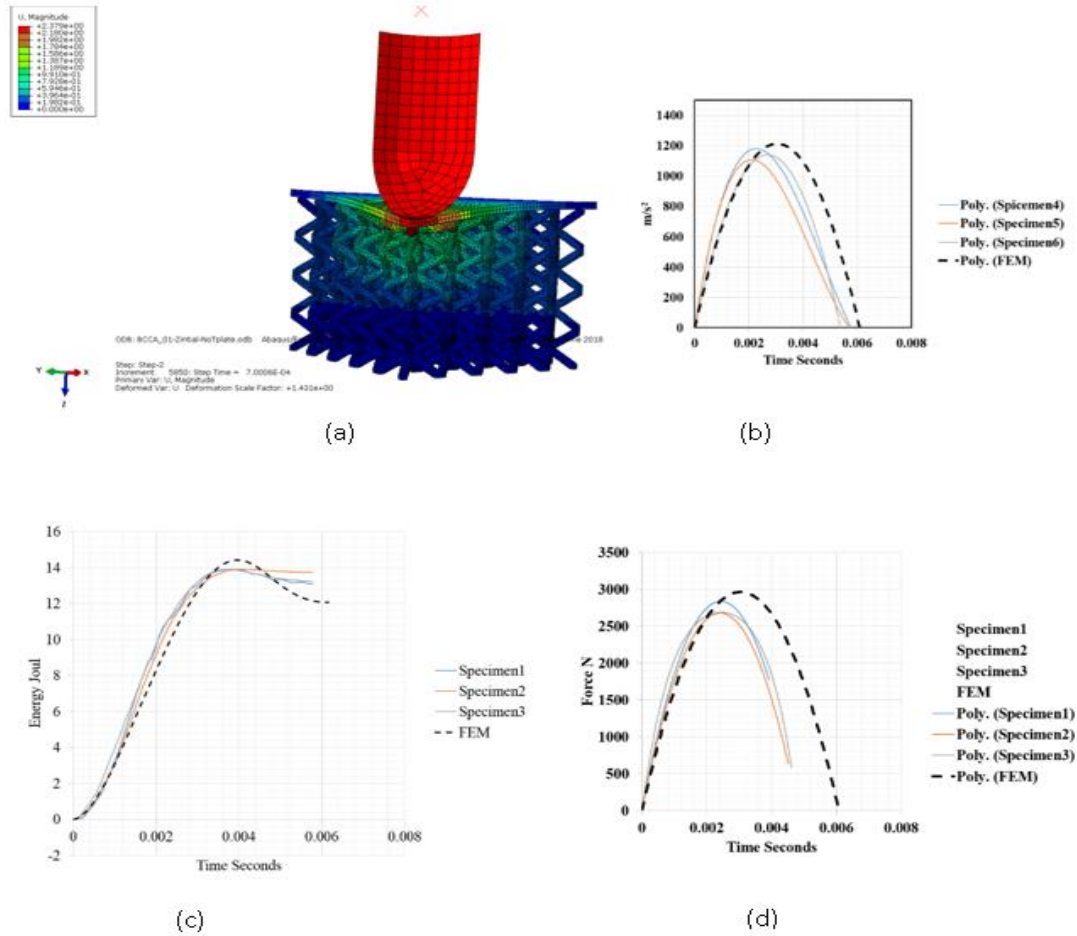


Figure 2.14 BCCA impact results experimental and FEM (a) Impact simulation (b) Acceleration-time (c) energy-time, and (d) force-time

Table 2.3 SEAs comparisons FEM vs experiment for the Impact test

SEA (J/Kg) for the BCC			SEA (J/Kg) for the BCCV			SEA (J/Kg) for the BCCA		
Experiment	FEM	Error%	Experiment	FEM	Error%	Experiment	FEM	Error%
719.62	669.24	7.0%	626.67	578.48	7.6%	695.83	658.23	5.4%

2.9 Summary

Chapter 2 has addressed how to create finite element model for compression and impact tests based on the elastic plastic stages. Because of the complexity of the geometric

feature for the lattice, the ABAQUS SolidWorks associative interface ASI tools was used to create the geometry and transfer the model to ABAQUS for completing the FEM modeling. However, this model is to be meshed only with Free Tech which only accepts tetrahedron mesh. Because the tetrahedron mesh has fewer degree of freedom than the brick elements, it will be stiffer and less accurate and as such is reliable for the elastic stages only. According to the results, the models for both the compression and impact tests have shown good correlation for all the configurations with small errors. Even though these models were efficient, and the results were validated, there are still some drawbacks. First, the models are not able to capture the post-yielding stages completely, second the computational time is high, third the models are still not perfectly matched to reality. For these reasons, any other possible solution was sought in order to getting high accuracy and reduce the computational time. The next chapter addresses the development of Python code to create and analyzing the lattice geometric shape and create a GUI (graphic user interface) under the name of Lattice Structure Designer (LSD) tool. This tool will help to create more reliable models to capture the post-yielding stages and the fracture mechanisms.

Chapter 3. Developing Python Code for Lattice Structure Designer (LSD)

3.1 Overview

Chapter 2 addressed the development of finite element models for the lattice structures by creating the lattice in the SolidWorks and transferring the model to the ABAQUS via the SolidWorks Associative Interface tool. This model has successfully provided the information and simulation for the elasticity stages but insubstantial in plasticity stages. This is because the tetrahedron elements cannot work very well to capture the post-plasticity stages accurately as shown in the Figure 3.1. Also, according to Cook and Banzely [81, 82] , the tetrahedron elements tends to be stiffer than the hexahedron elements because they have fewer degrees of freedom. On the other hand, the brick elements are more capable to capture the post-yielding stages and fracture progressive (see the Figure 3.1).

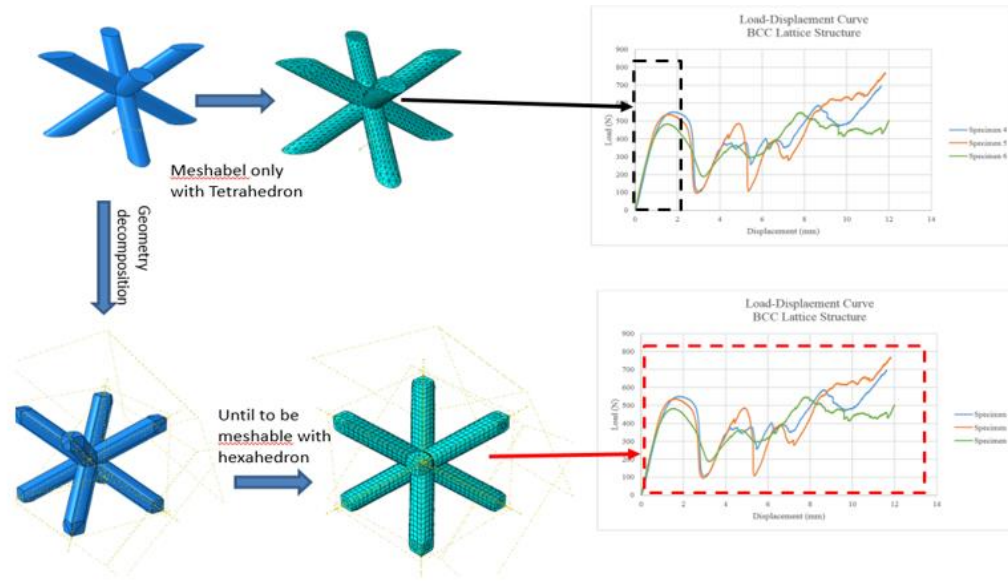


Figure 3.1 Tetrahedron and hexahedron characteristics comparisons

It was proven that ABAQUS is effective for modeling of mechanical behavior and particularly good in simulating composite materials [22, 28, 111]. For example, according to [112], ABAQUS has been used for the composite material of Steel-concrete structures. Also, ABAQUS is able simulate fully composite material behaviors of linear and nonlinear stages [112]. Also, ABAQUS was used for the lattice discrete method to model the fracture and analyze the damage after the break [113], and to capture the dynamics behavior [114]. Therefore, ABAQUS is appropriate software to simulate the finite element modeling for the composite materials.

3.2 ABAQUS /Python Graphical User Interface (GUI)

According to (Simulia, GUI plugin, 2016), the Lattice GUI is essentially an initialized Python interpreter to allow active entry of Python on the ABAQUS scripting interface commands [80, 115]. Because Python is powerful programming, the tools can

allow to combine the functionality of the GUI and other features to create a single program that can model the failure and post failure behavior of lattice structures [116-119]. For this reason, Python scripting will be used to create the model, define the materials, define the geometry, define the boundary conditions, define the geometry faces, and submit the jobs and perform the analytical studies. Therefore, a creative GUI interface under the name of Lattice Structure Designer (LSD) was designed and developed. Development of this program will be discussed in this chapter (chapter 4). LSD installation, running and output validation will be discussed next in chapter 5.

3.3 Developing ABAQUS Plug-In Tool GUI to Create and Perform ABAQUS

Modeling

Because of the complexity of procedures to create an LCS model in ABAQUS, it is required to enhance ABAQUS to do more efficient modeling for good mesh convergence and good parameters. For example, Nesládek and Španiel developed an ABAQUS plug-in tool for capturing and simulating multi applications of the fatigue design [120]. The reason for this tool is to design FEM topology and reduce the solution time and amount of error. This software can predict the material behavior and damage mechanisms due to the fatigue condition [120]. The program was conceived as a plugin equipped with a graphical user define interface (GUI) running under ABAQUS. It offers a function for interacting with the model in an ABAQUS viewport to make the preparation as simple as possible. The program can perform many fatigue cases possible [120]. Another plug-in tool used with ABAQUS is called representative volume element (RVE). It generates 2D and 3D composite materials. However, ABAQUS has included the technology of FE-RVE analysis in the base program and is costly in computational time. For this reason, the tool RVE for

Micromechanics plug-ins was developed for ABAQUS [80, 117]. However, this plugin must be coded in Python and to be scripted in ABAQUS. This tool can be found in the plugins tab in ABAQUS and display plugins dialog in a separate window. These tools can offer less human intervention and model multiple event in micromechanics in composite materials [121].

3.4 The LSD Algorithm Flow Chart

Figure 3.2 shows the program flow chart proposed for the LSD program. Some of the work will be done by Python scripting and submitted to the ABAQUS solver to complete the work and perform the analysis and capture the output. In other words, the Python will help to perform all challenging tasks that are difficult or impossible to be performed manually. Some of these tasks are creating parts with specific datum, geometric decomposition, face recognition, body coupling, body (feature) realization, linear and polar patterns, part location adjustment (translation or rotation if needed), assigning the boundary conditions, assigning the materials (i.e. creating library, sections, and assign to the model) and finally creating the Job to be ready for submission. However, to have the Python scripting work in ABAQUS environment, it is required to import some of ABAQUS components as parameters for the LSD scripting as shown in the Figure 3.3. For example, it is required to import what is needed to create the models such as *part*, *ABAQUS constant*, *material*, *assembly*, *materials* etc. Otherwise, the Python scripting will not be able to access the ABAQUS features. Also, to make the Python program readable and easy to track, one *class* was created under the name *createpart* to manipulate all the input parameter such as the dimensions, number of cells and so on.

➤ ABAQUS Graphical user interface (GUI)

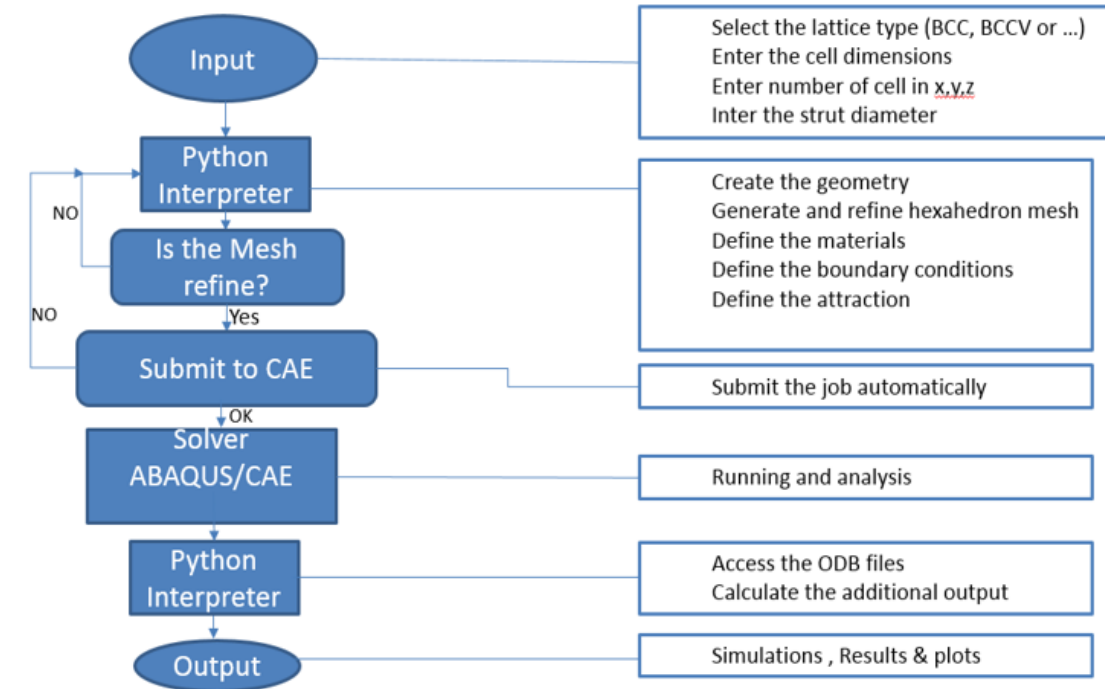


Figure 3.2 Initial Python flow chart

```

# -*- coding: mbcs -*-
from abaqus import *
from abaqusConstants import *
from part import *
from material import *
from section import *
from assembly import *
from step import *
from interaction import *
from load import *
from mesh import *
from optimization import *
from job import *
from sketch import *
from visualization import *
from connectorBehavior import *
#from abaqusTester import *

def createPart (X, Y, Z, R, NX, NY, NZ, HFrame3, ComboBox1):#X=X Dim , Y=Y_Dim , Z=Z_Dim , r is the strut radius
    #TT=ComboBox1.appendItem('BCC')
    mdb.models['Model-1'].Part(dimensionality=THREE_D, name='Part-1', type=
    DEFORMABLE_BODY)
    M=mdb.models['Model-1']
    P=M.parts['Part-1']
  
```

Figure 3.3 Proposed GUI programming

3.5 The LSD Input Data and Characters

The LSD input was designed based on three portions for the input data. The first input was the configuration type. The second input was for entering the dimensions and cell distributions. The third input was for selecting the materials. For the first input, a combo box with a list of items were designed to select the configuration type. This combo box was designated as *ComboBox1* for the coding. The list items were designed to accept the string values and the values were BCC, BCCV, BCCA, Tet, TetH, and Pyr seen in Figure 3.4. After selecting the configuration, to the user must enter the dimension of the configuration. For this reason, it was designed the second input. Because the configuration is based on three types of the families such as BCC, Tet, or Pyr, the second input port was classified into three groups. First group was the BCC, BCCV, and BCCA, second group was Tet and TetH, third group was Pyr. See Figure 3.5 for how this looks in the software. Table 3.1 shows all the dimension parameters used for the programming. The third input was for the materials frame, this frame was designed based on two portions for the input, first was for the default's materials such as ABS, Ti-6Al-4V, and second was for any other possible material. First, for the default materials, the material parameters such as elasticity and plasticity were included in the code. Second, for any other materials, the text box was designed to allow input of the mechanical properties and the material name manually. See Figure 3.6 and Table 3.2 for the material parameters.

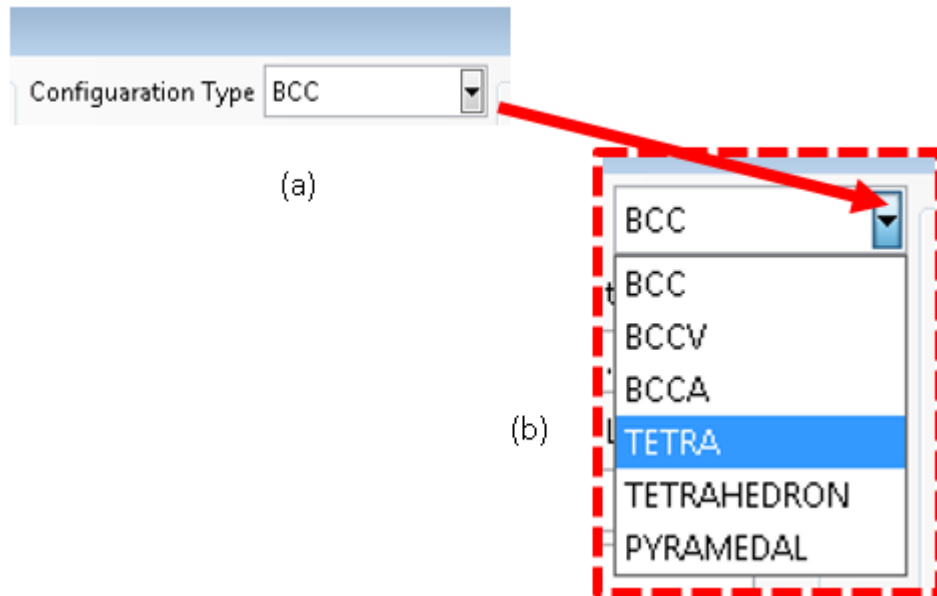


Figure 3.4 First input portion (a) ComboBox, and (b) List Item



Figure 3.5 Second Input for three groups of dimensions

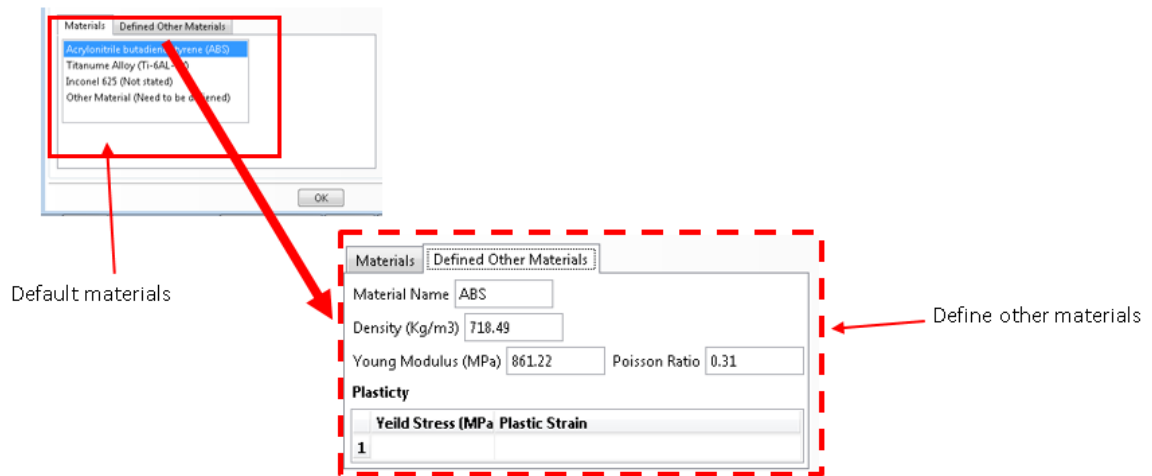


Figure 3.6 Third input for the materials

Table 3.1 Second input data parameters

Input Group	The Variable	Meaning
	R	Strut radius
Group (1)	NX	Number of cells in x direction
BCC, BCCV, BCCA	NY	Number of cells in Y direction
	NZ	Number of cells in Z direction
	X	The cell dimension in X direction
	Y	The cell dimension in y direction
	Z	The cell dimension in z direction
Group (2)	SL	Side length
	ZH	The tetra/ tetrahedron cell Hight

Tetra	and <i>NTZ</i>	Number of cells in Z directions
Tetrahedron	<i>RadL</i>	Number of radial levels for the cell distribution
Group (3)	<i>Pyr_SL</i>	Side length
Pyramidal	<i>Pyr_Z</i>	The Pyramidal cell height
	<i>NPH</i>	Number of cells in Z directions
	<i>NPX</i>	Number of cells in x directions
	<i>NPY</i>	Number of cells in y directions

Table 3.2 Material parameters for the Third input

The material variable	Meaning	Description
<i>Mat_name</i>	Material name	
<i>Den</i>	Density	
<i>Young</i>	The young modulus	
<i>Poiss</i>	Poisson ratio	
<i>Table</i>	Plasticity data	

3.6 Python Interpreter

For the python script, Notepad⁺⁺ was used to debug the program. This interpreter is used to perform many complex tasks such as creating the geometry and decomposing

the geometry by partitioning, meshing, face recognition, body recognition, patterns (linear-polar), unions, materials assigning, and creating Jobs for submissions.

3.6.1 Creating the Geometry and Decomposition

Because the brick elements have more degrees of freedom and higher degrees of formulation, Benzaly [81] and Simulia [80] have recommended using a hexahedron mesh for capturing post-yield stages. In other words, to capture the lattice progressive failures for all layers until the densification, one must use the hexahedron mesh with some finite element enhancements. Moreover, there are many other benefits of using hexahedron meshes, such as reducing the computational time and providing fracture simulations. Basically, every part can be automatically meshed with tetrahedron elements, but there are few geometric shapes that can be automatically meshed by hexahedron elements as was mentioned in section 1.2.4.3. However, it is required to decompose the lattice into ABAQUS as a regular geometric structure before they can be meshed with hexahedron elements automatically. These procedures are costly and tedious for one lattice cell, as shown in Figure 3.7 (a) for one-unit cell of BCC. Consequently, for whole lattice structure, the procedures have to be repeated and tested with an optimized mesh density as shown in Figure 3.7 (b). Therefore, application of these manual procedures in generating hexahedron for one cell lattice structure is exhausting and time consuming.

To solve these problems, the plugin tool LSD was developed for ABAQUS which can automatically perform these repetitive and complex tasks [118, 122]. The struts are defined based on datum points in X,Y,Z coordinates and these points will identify the location of the struts ends, and they are based on the cell dimensions in (X,Y,Z) as shown in the Figure 3.8 (a). The commend *ReferencePoint* will be used to identify the reference

point of the unit cell and the command *DatumPointByCoordinate* will be used to locate the points in the ABAQUS coordinate system as shown in the Figure 3.8 (b). All the coordinates X,Y,and Z will be entered as the unit cell dimensions. After that, the program will be ready to create the 3D solid features by using the command *SolidExtrude* and create the first struts. This procedure needs to be repeated to create all the struts (see Figure 3.8). Next, the struts are partitioned as next step, but it is needed to assign the partitioning planes. The partitioning planes are created based on the datum points, but eight partitioning planes are required for each strut as shown in Figure 3.9. Then the program will check the mesh for one unit-cell to ensure the meshability of the cell before repeating this procedure to the entire lattice structure as shown in the Figure 3.10.

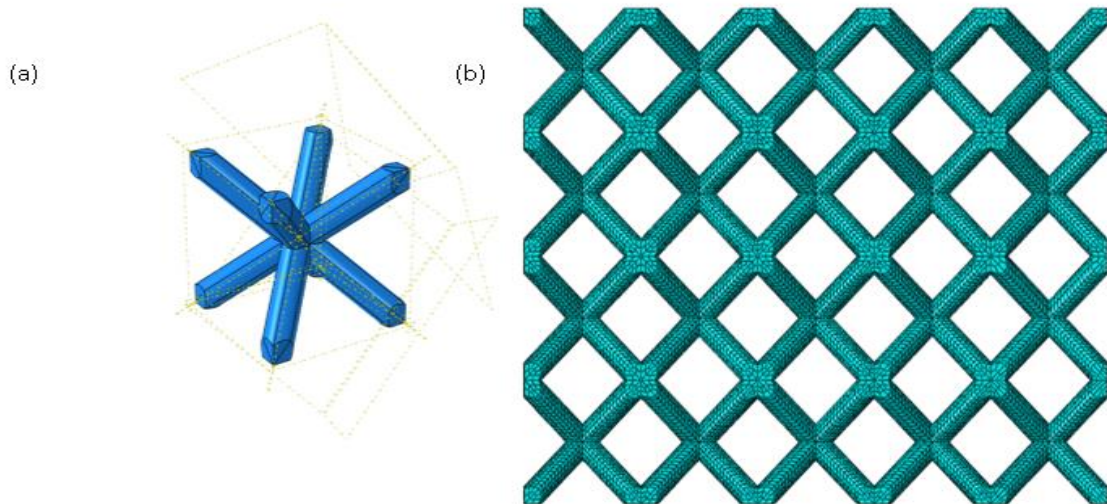
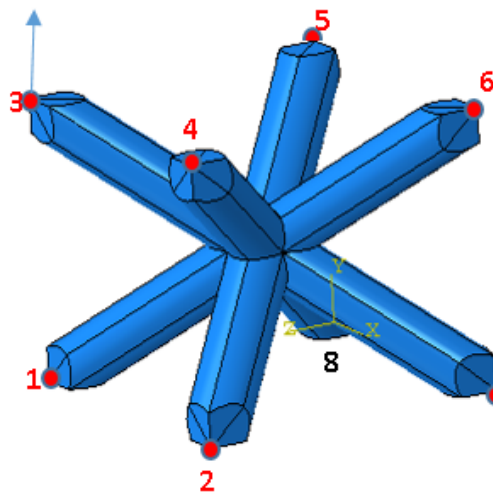


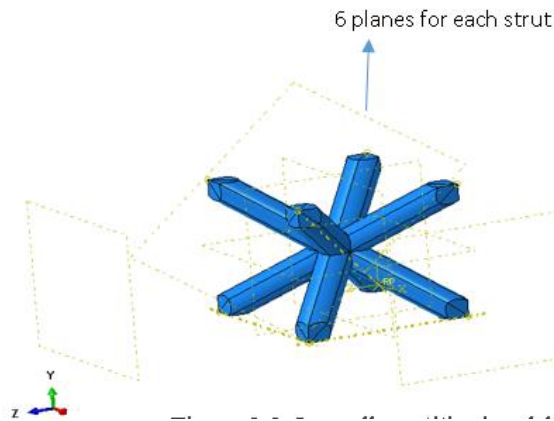
Figure 3.7 BCC (a) Decompose one cell, and (b) Optimum brick mesh for entire BCC lattice

8 Datums



- Datum 1 → P.ReferencePoint(point=(0.0, 0.0, 0.0))
- Datum 2 → P.DatumPointByCoordinate(coords=(X, 0.0, 0.0))
- Datum 3 → P.DatumPointByCoordinate(coords=(0.0, Y, 0.0))
- Datum 4 → P.DatumPointByCoordinate(coords=(0.0, 0.0, Z))
- Datum 5 → P.DatumPointByCoordinate(coords=(X, Y, 0.0))
- Datum 6 → P.DatumPointByCoordinate(coords=(X, 0.0, Z))
- Datum 7 → P.DatumPointByCoordinate(coords=(X, Y, Z))
- Datum 8 → P.DatumPointByCoordinate(coords=(0.0, Y, Z))

Figure 3.8 BCC Unit cell debugging



- P.DatumPlaneByPrincipalPlane(offset=Z/2., principalPlane=XYPLANE)
- P.DatumPlaneByPrincipalPlane(offset=X/2., principalPlane=YZPLANE)
- P.DatumPlaneByPrincipalPlane(offset=Y/2., principalPlane=XZPLANE)
- P.Mirror(keepOriginal=0N, mirrorPlane=P.datums[14])
- P.Mirror(keepOriginal=0N, mirrorPlane=P.datums[13])
- P.DatumPlaneByOffset(flip=SIDE1, offset=8.0, plane=P.datums[13])

Figure 3.9 One cell partitioning debugging with 6 planes for each strut

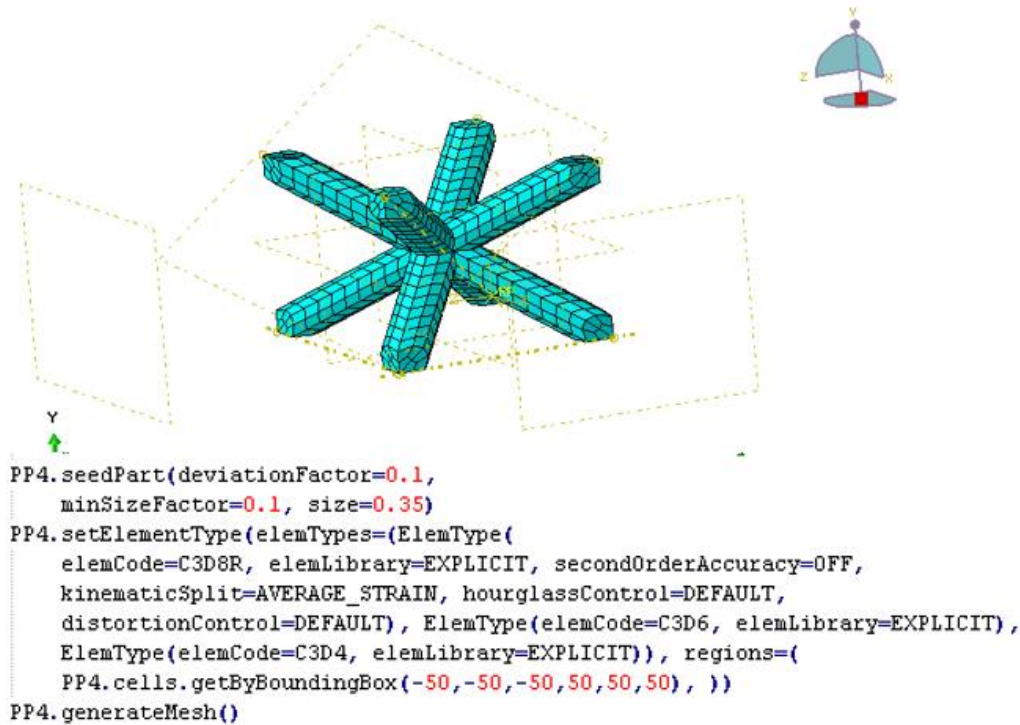


Figure 3.10 Mesh test for one-cell BCC

3.6.2 Face Recognition

Another challenge for modeling the lattice structure is selecting the faces that will be tied each other for multiple unit cells. Because of the strut partitioning, there will be multiple faces on the top and bottom of the lattice structure. For example, for one cell of the BCC as shown in the Figure 3.11, the number of faces will be eight at every side (see Figure 3.11). However, in the entire lattice structure with 5 by 5 by 4 units there will be $8 * 5 * 5 = 200$ faces and selecting all these faces manually are costly in time and effort. Therefore, it was required to formulate the lattice geometry and debug the procedure by using Python with ABAQUS GUI. The Program was designed to store all these faces as arrays, so they can be used for any other operations. To do this procedure, the program

design loop *while* was used to identify any arbitrary point located in the face. Because the centroid points are the most commonly selected points, it was selected to be reference point for each face. And based on points, the argument *findAt* was used to discover the faces and store them under a Tuple array with the name of *Faces_Tuple1* as shown in the Figure 3.11 [122, 123]. This technique was used to select the faces to be tied with the rigid plated in top and bottom of the configuration as shown in the Figure 3.12. For the entire lattice structure, the procedures were repeated based on the number of faces in the top or bottom side of the lattice structure and tied as shown in the Figure 3.13 for the final stage to tie the faces with the rigid plates.

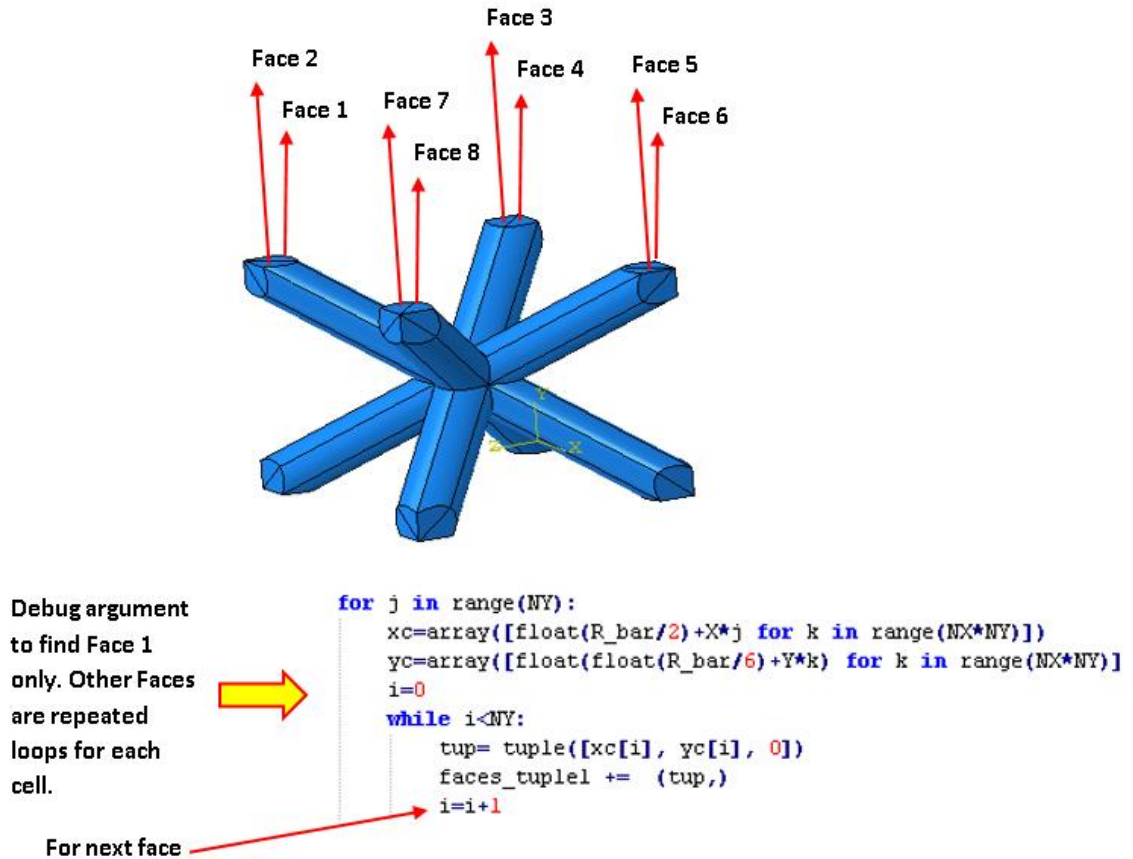
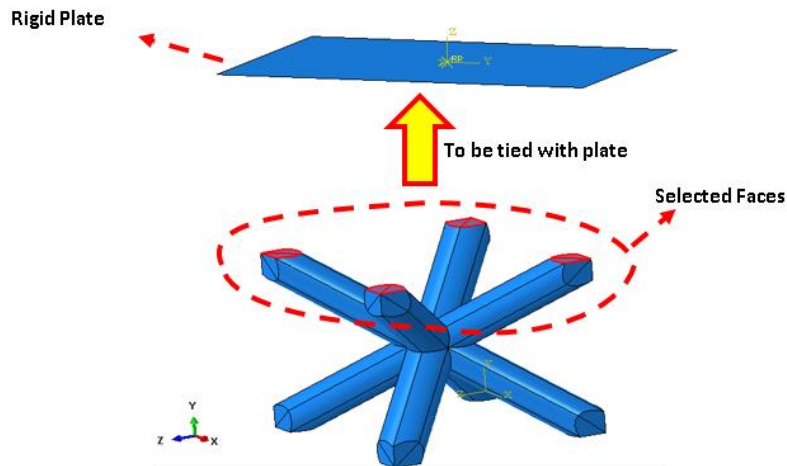


Figure 3.11 BCC unit cell faces recognition for 8 faces on top side



Select 8 Faces
for one cell

```
faceRegion = PFArt2.faces.findAt(coordinates=faces_tuple2+faces_tuple1+faces_tuple3+faces_tuple4+faces_tuple5+faces_tuple6+
faces_tuple7+faces_tuple8)
```

Create Tie
between the
selected faces
and the rigid
plate

```
mySurface = M.RootAssembly.Surface(
name='s_Surf-1', sideFaces=faceRegion)
mdb.models['Model-1'].Tie(adjust=ON, master=
mdb.models['Model-1'].rootAssembly-surfaces['m_Surf-1'], name=
'Constraint-1', positionToleranceMethod=COMPUTED, slave=
mdb.models['Model-1'].rootAssembly-surfaces['s_Surf-1'], thickness=0N,
tieRotations=0N)
```

Figure 3.12 For unit BCC face finding and tying with the rigid plate

Tie constraint between the lattice structure and the rigid plat in both sides

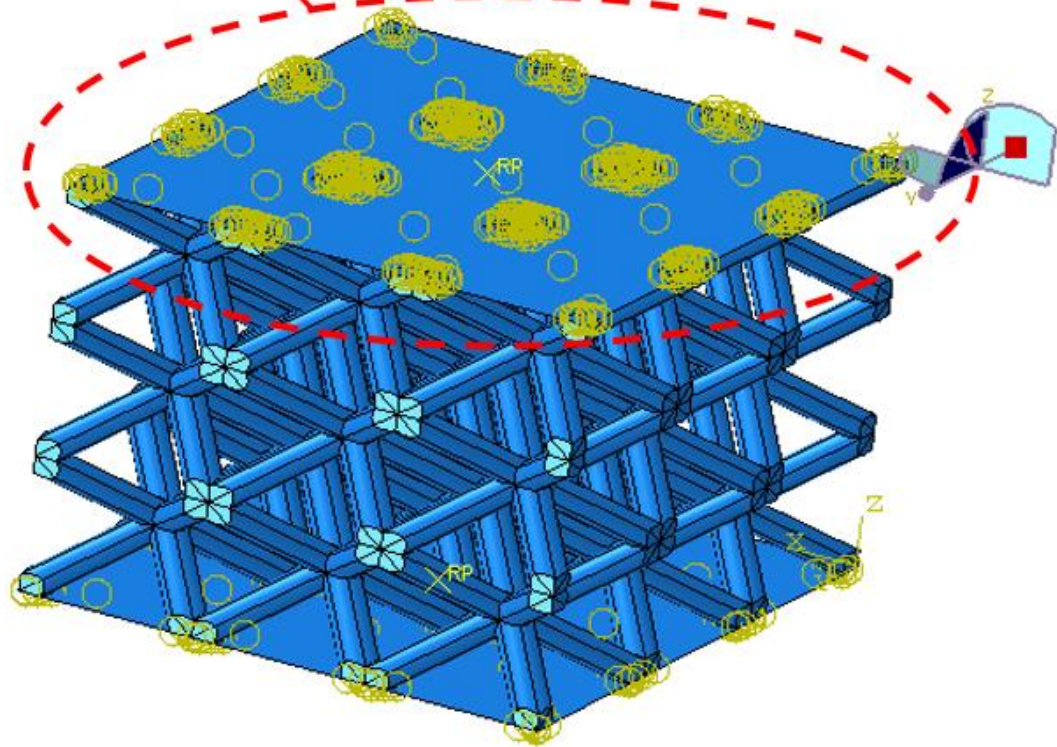


Figure 3.13 Final stage of Faces Tie with the Rigid plates

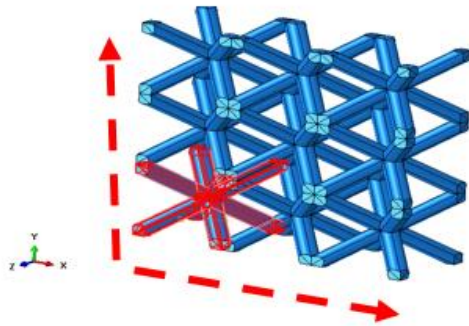
3.6.3 Cell Patterns and Union

After creating one-unit cell correctly with mesh convergence, the cell needs to be copied to create the entire configuration. There are two techniques to create the pattern: linear pattern and polar pattern [78, 80, 115, 123]. The configurations of BCC, BCCV, BCCA, and Pyramidal are arrayed linearly in X, Y and Z, whereas the configuration of Tetra and Tetrahedron are arrayed polarly in radial levels with linear patterns in Z direction. For these reasons, the linear pattern will be used only for BCC, BCCV, BCCA, and Pyramidal; but the polar pattern will be used for Tetra and Tetrahedron for radial arrays and linear pattern for Z arrays only. However, to do all these procedures is costly in time

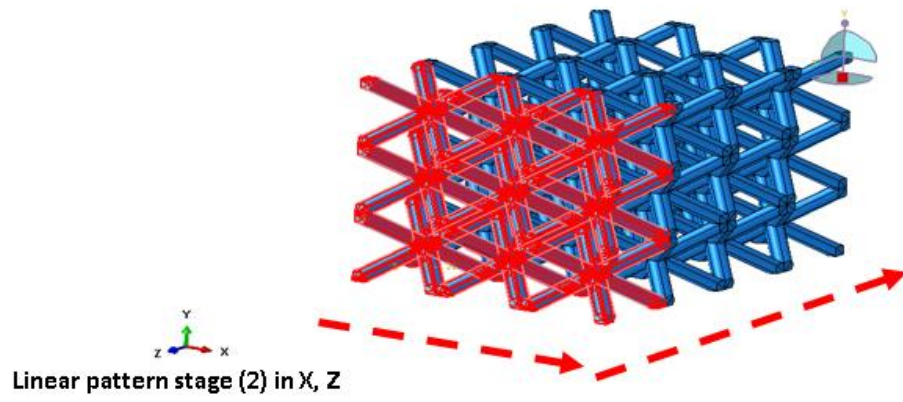
and effort if they were done manually, thus; a Python debug was developed to do all these procedures automatically. However, a user needs to select the initial part and after that they must select all the copied features and make them joined to convert them into a single part. For this matter we need to use a technique for body recognition which will be discussed in section 3.6.4. The following subsections will discuss the feature patterns, and translation and finally the join, but we need to keep all the part criteria such as the partitioning, materials, interactions, etc.

3.6.3.1 Linear Pattern

This technique was used only with the configurations that are linearly distributed such as BCC, BCCV, BCCA, and Pyramidal. Because the cells are distributed in (X, Y, Z) and the pattern for ABAQUS is only for 2D meshes (if we do it manually), we need to apply this command twice to perform it for 3D. First stage we need to apply it for X, Y and second stage apply it for X, Z as shown in the Figure 3.14. However, an argument needs to be created for the LSD to do all these steps in action by using a programmed 3D vector. This vector is called the Smart Vector. The Smart Vector will work to insert and move the parts based on the configuration selected and the input parameters. After this step, the Smart Vector will produce the cells and deduct the directions and build the configurations adequately as shown in the Figure 3.15. According to the code, the Smart Vector was designed by using 3 loops, one for each direction. These loops will produce mutable 3D vectors and part for each vector and this part will be moved automatically to its location.

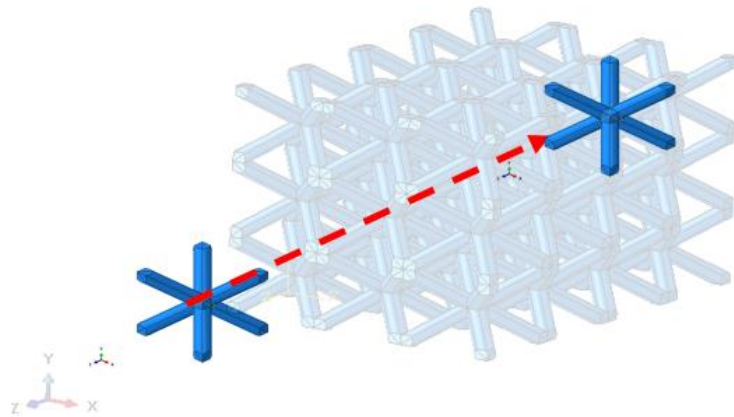


Linear pattern stage (1) in X, Y



Linear pattern stage (2) in X, Z

Figure 3.14 Basic Linear pattern stages for the Lattice



Insert and translate the cell Smart 3D vector. →

```

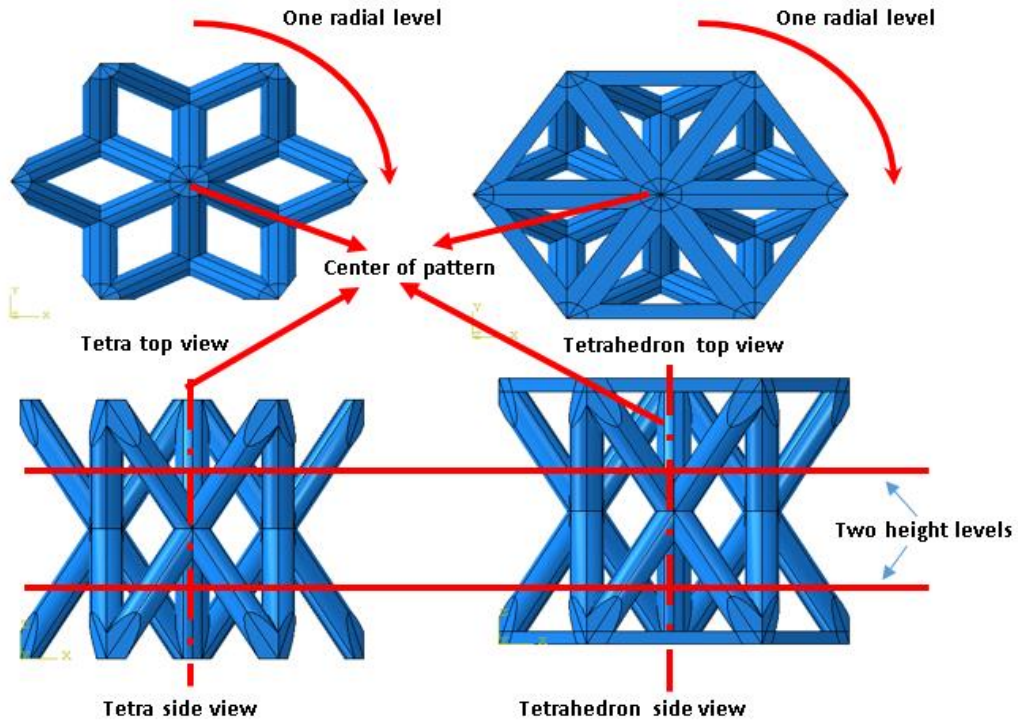
for i in range(NX):
    for j in range(NY):
        for k in range(NZ):
            a=M.rootAssembly.Instance(dependent=ON, name='Cell'+str(i)+str(j)+str(k),
                part=P)
            a.translate(vector=((0.0+(i*X)), (0.0+(j*Y)), (0.0+(k*Z))))

```

Figure 3.15 performing linear pattern by using smart 3D vector debugging

3.6.3.2 Polar Pattern

The polar pattern is required for Tetra and Tetrahedron configurations. Because the Tetra and Tetrahedron cells are distributed in radial level around central axis known as center of pattern as shown in Figure 3.16, it is required to use polar pattern. However, for the second level of the Tetra and Tetrahedron, the user must flip some cells to make the arrangement as shown in Figure 3.17, for Tetrahedron with second level of radial debugging.



```

adb.models['Model-1'].rootAssembly.InstanceFromBooleanMerge(name="Tetra_Coll", instances=([M.rootAssembly.instances[SingleInstances_List[n]]
for n in range(len(SingleInstances_List))]), mergeNodes=ALL,
nodeMergingTolerance=0.1, domain=GEOMETRY,keepIntersections=ON, originalInstances=DELETE)
adb.models['Model-1'].rootAssembly.RadialInstancePattern(axis=(0.0, 0.0, -0.25)
, instanceList=('Tetra_Coll-1', ), number=6, point=(0.0, 0.0, 0.125),
totalAngle=360.0)

```

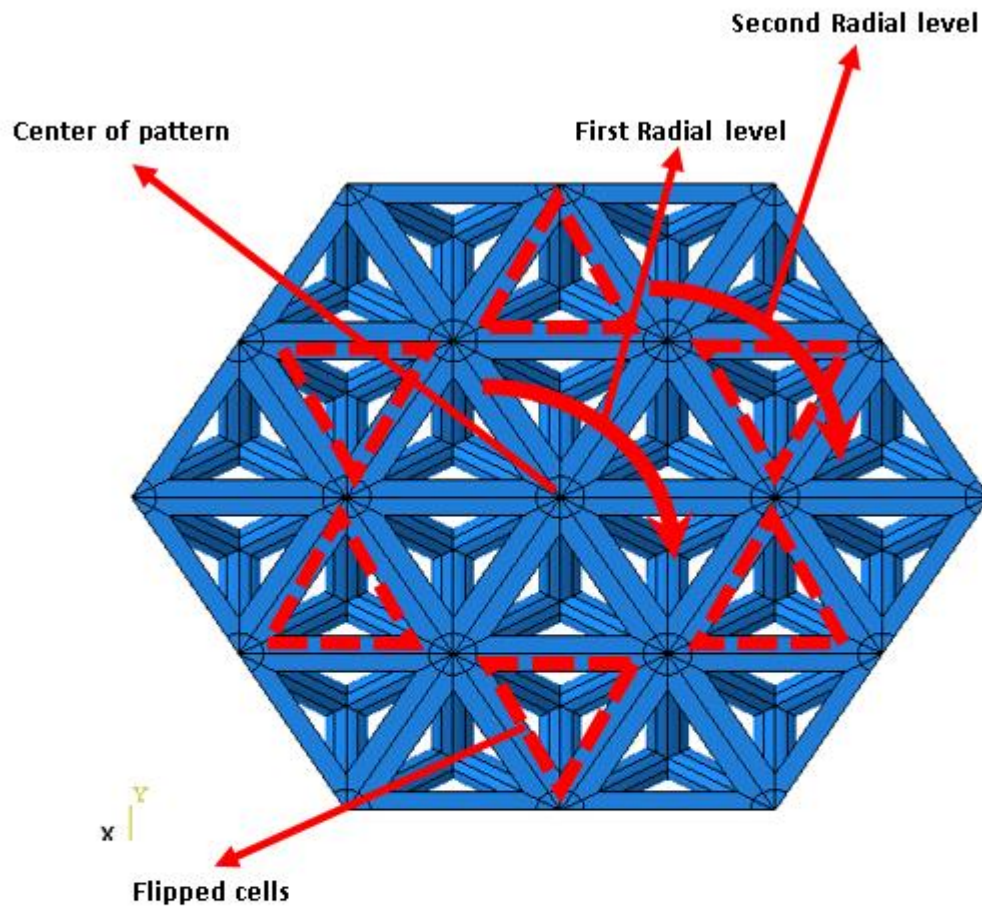
Angle of pattern

Axis parallel to Z axis

Arbitrary point located in Z axis

Number of cells for one radial

Figure 3.16 Tetra and Tetrahedron arrays and arrangements



```

if RadL > 1:
    for i in range(N_rad):
        H.rootAsseblly.Instance(dependent=ON, name='PNFLP'+str(i),
                                part=ndb.models['Model-1'].parts['Part-4'])
        H.rootAsseblly.rotate(angle=180.0, axisDirection=(0.0, 0.0,
                                                         -1.0), axisPoint=(0, 0, ZH), instanceList=('PNFLP'+str(i), ))
        ndb.models['Model-1'].rootAsseblly.translate(instanceList=('PNFLP'+str(i), ), vector=(
            SL/2.0, (2*i+1)*-SL*sin(60*pi/180), 0))
        ndb.models['Model-1'].rootAsseblly.LinearInstancePattern(direction1=(5.0, -sin(60*pi/180),
                                                                              0.0), direction2=(0.5, -sin(60*pi/180),
                                                                              0.0), instanceList=('PNFLP'+str(i), ), number1=1,
                                                                              number2=RadL-2*i-1, spacing1=SL/2.0, spacing2=SL)

        ndb.models['Model-1'].rootAsseblly.LinearInstancePattern(direction1=(5.0, sin(60*pi/180),
                                                                              0.0), direction2=(-0.5, -sin(60*pi/180),
                                                                              0.0), instanceList=('PNFLP'+str(i), ), number1=1,
                                                                              number2=RadL-2*i-1, spacing1=SL/2.0, spacing2=SL)

```

Figure 3.17 Top view of the Tetrahedron shows the flipped cells arrangements

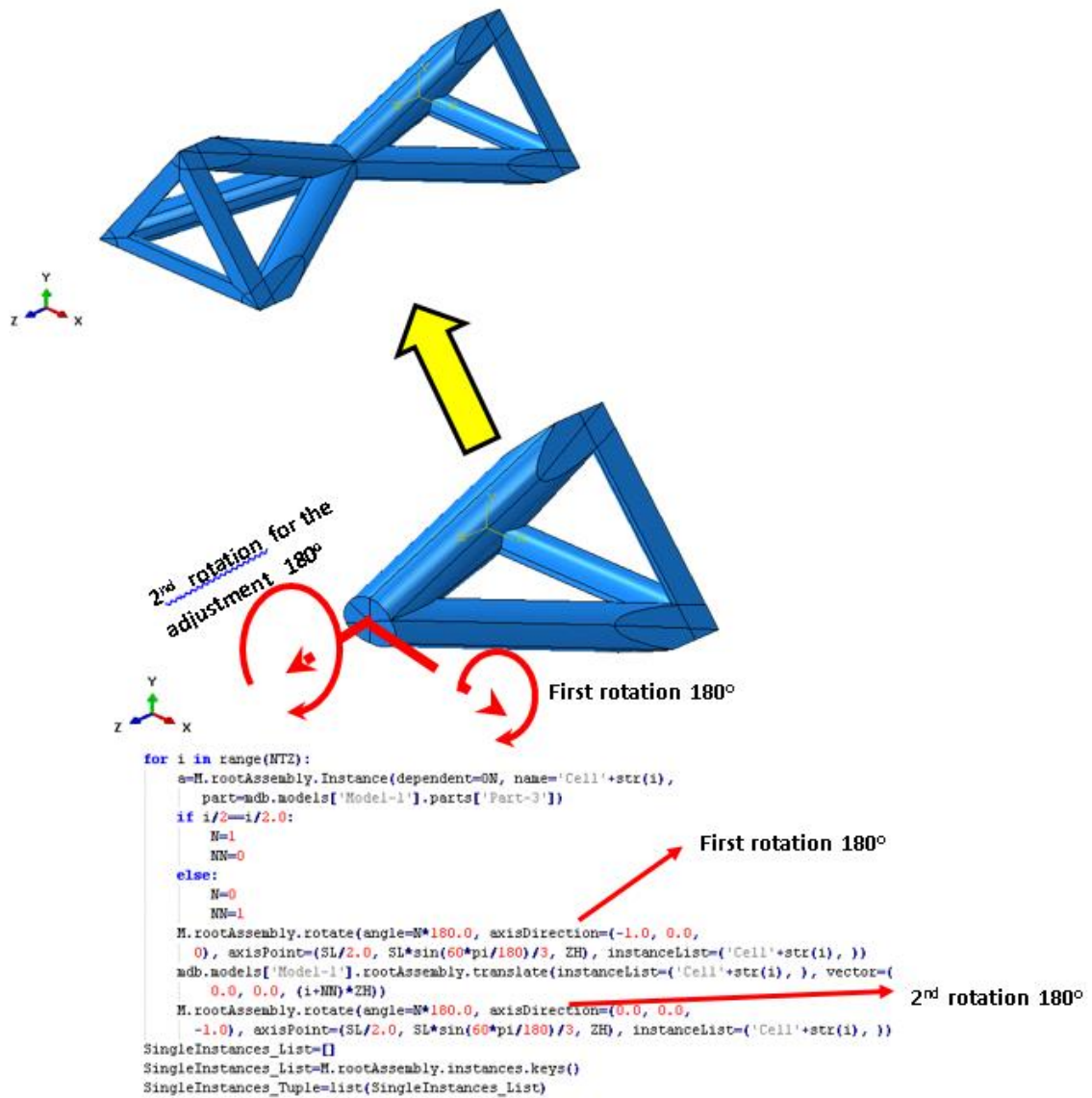


Figure 3.18 Tetrahedron vertical arrays adjustments debugging

3.6.3.3 Translation, Rotation, and Adjustments

This technique is used with the configurations that are required to mirror in the upper or lower levels of the lattice. For example, Tetra, Tetrahedron, and Pyramidal cells need to be flipped in thickness direction. For manual design, mirroring can be used to create flipped cells. However, the mirror command is restricted in ABAQUS to features with planes and boundaries. For these reasons, the cell will be translated and rotated twice to be

adjusted in proper location as shown in the Figure 3.18. The first rotation is to create flipped cells, whereas the second rotation is to adjust the cells locations (See Figure 3.18).

3.6.4 Body Recognitions

This technique is used to show the available features to be analyzed in further commands such as linear or polar patterns and join. First store the feature as tuple or list by using the command `keys()`. Next, use the comment `list` to save all the features under the name of `SingleInstances_Tuple` as shown in Figure 3.19. The example is a print to verify the number of the features and name of the first feature.

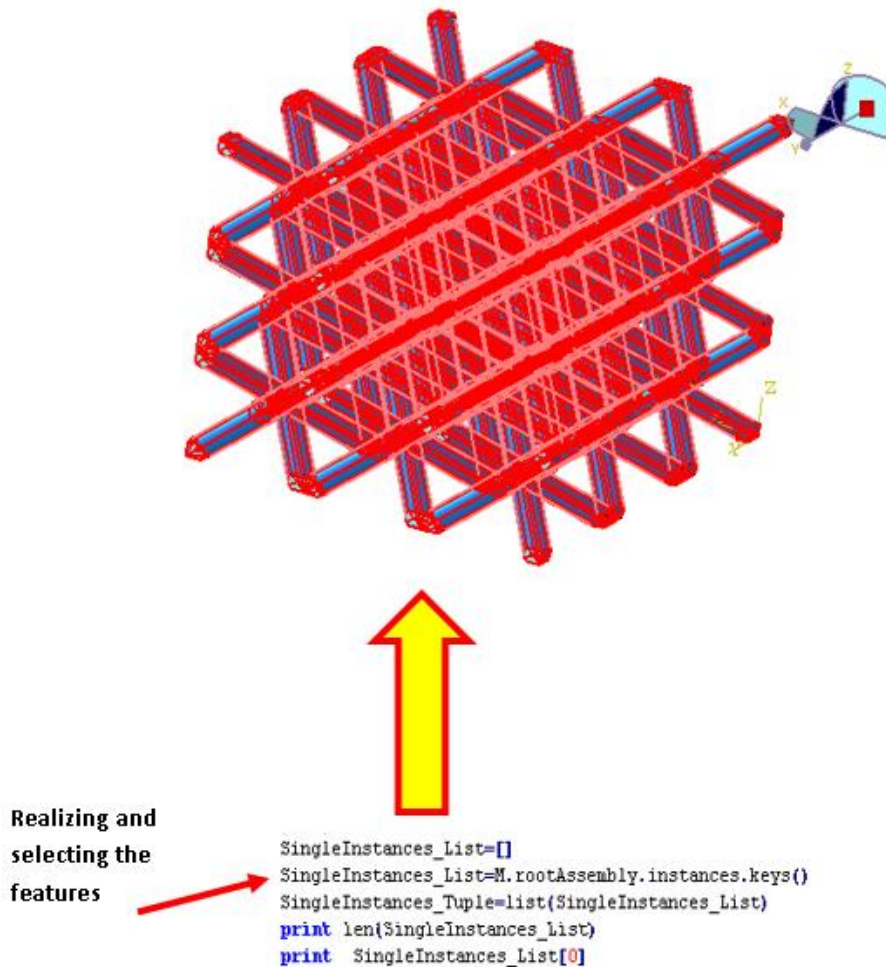


Figure 3.19 Body recognition technique debugging

3.6.5 Features Union

This technique is used to unite many features into one part. It is required to select the features first by using the technique in section 3.6.4, and union them by using the argument *InstanceFromBooleanMerge* to create a new part from the union of the minor parts. However, one needs to keep the boundary by using the *Retain* command and deleting the instances by using *Delete* as shown in the Figure 3.20.

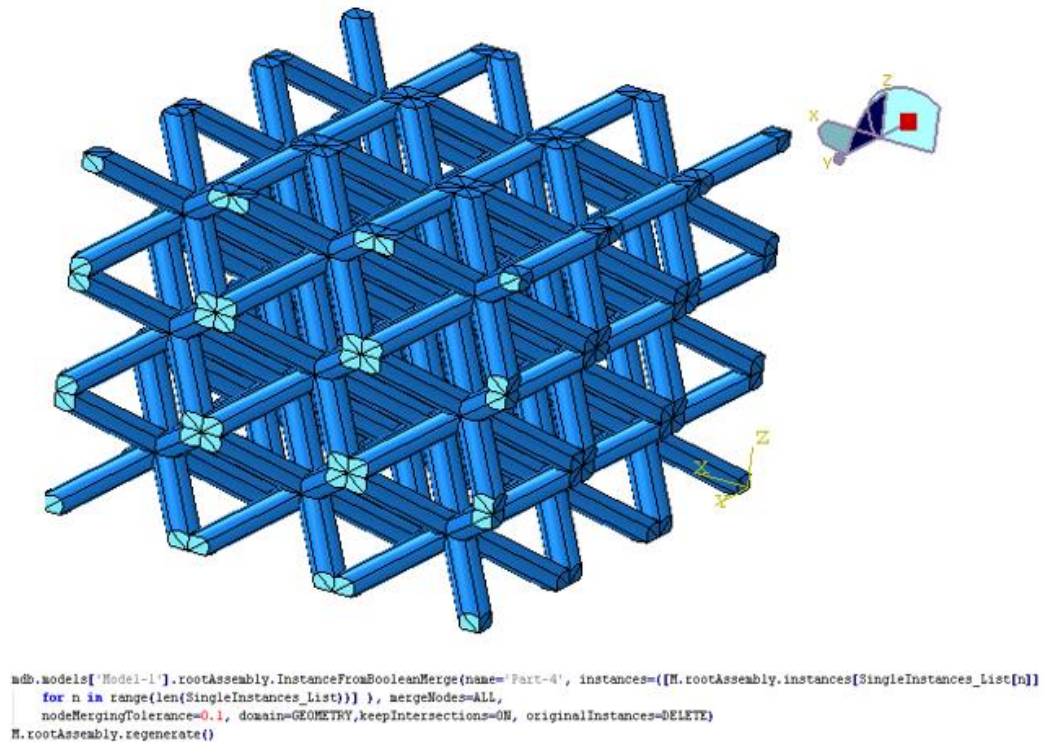


Figure 3.20 Feature union debugging

3.6.6 Creating the Rigid Plates

Technically there are two rigid plates: one on top and another in bottom of the configurations. The movable plate is to be given a specified displacement and the other one

is fixed with *Encaster* boundary conditions. However, the dimensions of the rigid plate have to be appropriate to the size of the lattice structure. For this reason, the rigid plate was given a rectangle shape with dimensions higher than the possible dimension of the lattice by 5 to 10 mm. New parameters of XD, YD, and ZD are created to adjust the dimension and locations of the plates as shown in the Figure 3.21.

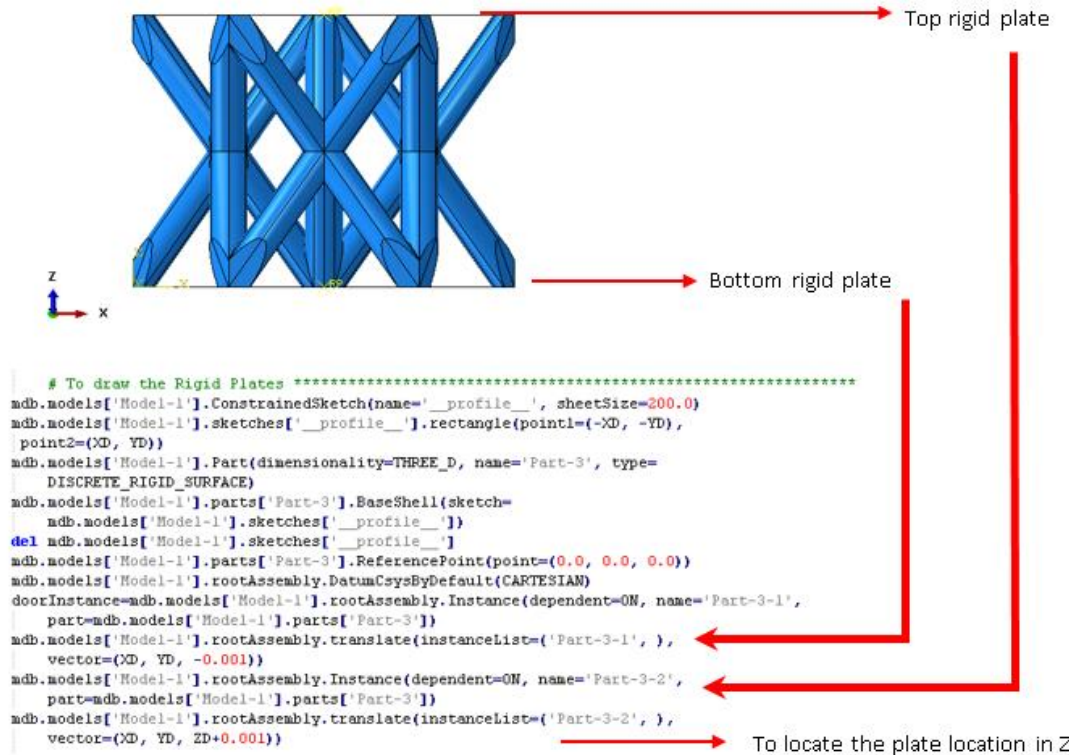


Figure 3.21 Rigid plates creating and adjusting

3.6.7 Assigning the Boundary Conditions

Two types of boundary conditions were assigned, first for the top plate to be movable with specific dimensions and other for the bottom plate to be fixed (*Encaster*). For the *Encaster* boundary condition all the displacement and rotations such as u_1 , u_2 , u_3 , ur_1 , ur_2 , and ur_3 are *zeros*, whereas, for the movable plate the boundary condition u_3 is

equal to the given displacement. Here for the debugging the displaced were assumed equal to $FD=1$ times 0.5 for the adjustments as shown in the Figure 3.22.

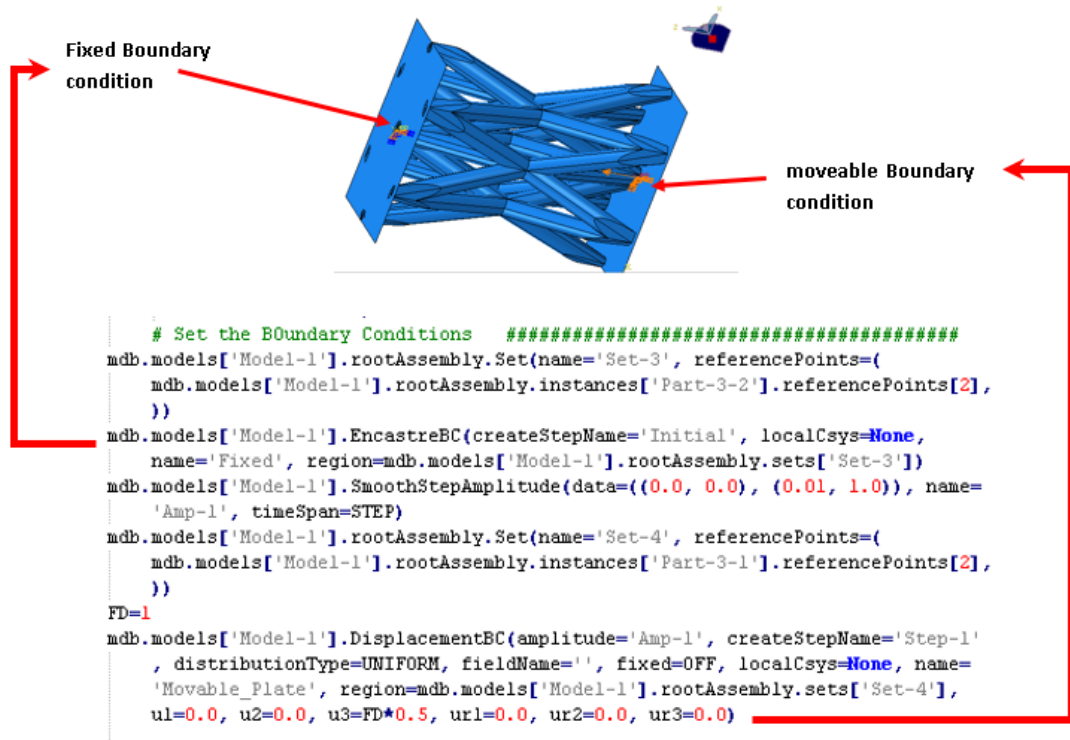


Figure 3.22 Assigning the boundary conditions in the rigid plates

3.6.8 Creating Output Sets and Steps.

The time step was considered to be 0.01 second and the mass scaling was taken as defaults which is about $1E-12$ seconds. For the output, the reference point at the movable rigid plate was denoted as *Set -1* to capture the reaction force and the displacement for the interval of 100 (see Figure 3.23).

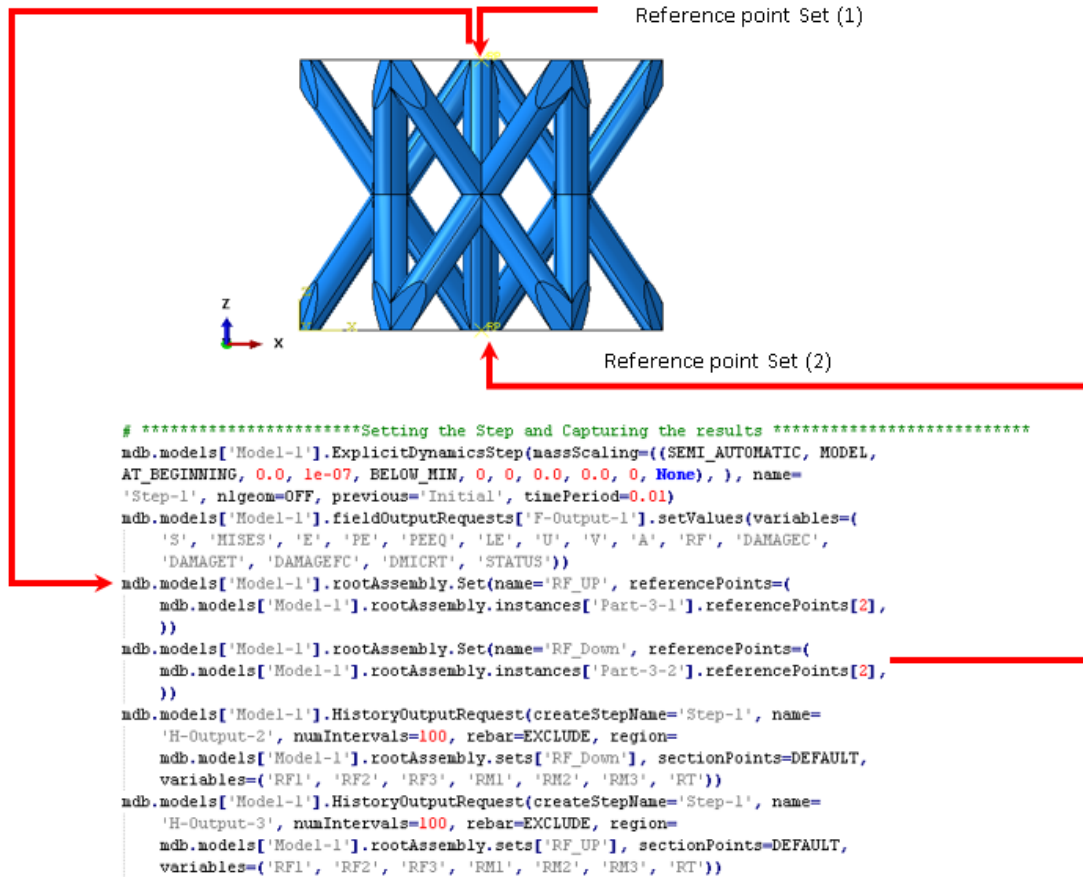
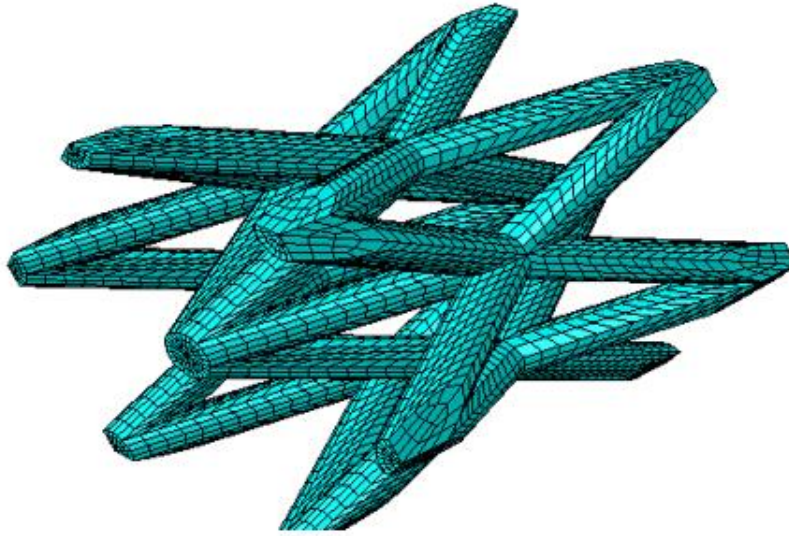


Figure 3.23 Debugging the output in the reference points at the rigid plates

3.6.9 Applying the Mesh

For all the configurations, the final mesh procedure is same because the configuration has been decomposed, as was discussed in section 3.3. The mesh size was taken from previous study according to the convergence as 0.35 mm [20, 22, 89, 109]. linear elements with type of C3D4 were used due to the established feasibility of this element with the lattice structures simulations as was addressed in section 1.2.2.4. The LSD program is run multiple times until the mesh convergence is achieved. After this step the result will be as shown in the Figure 3.24 for the Tetra structure and the Figure 3.25 for the BCC configuration.



```
PP4.seedPart(deviationFactor=0.1,  
            minSizeFactor=0.1, size=0.35)  
PP4.setElementType(elemTypes=(ElemType(  
    elemCode=C3D8R, elemLibrary=EXPLICIT, secondOrderAccuracy=OFF,  
    kinematicSplit=AVERAGE_STRAIN, hourglassControl=DEFAULT,  
    distortionControl=DEFAULT), ElemType(elemCode=C3D6, elemLibrary=EXPLICIT),  
    ElemType(elemCode=C3D4, elemLibrary=EXPLICIT)), regions=(  
    PP4.cells.getByBoundingBox(-50,-50,-50,50,50,50), ))  
PP4.generateMesh()
```

Figure 3.24 Tetra with ideal brick mesh



Figure 3.25 Ideal meshed BCC lattice structure created by the GUI

3.6.10 Debugging of the Materials for Modeling

The GUI program was designed to have two sets of materials as default materials (i.e. ABS and Ti-6Al-6V), and another set is for any other possible printed materials. For the default material, the LSD code includes the material properties for both Acrylonitrile Butadiene Styrene (ABS) and Titanium alloy (Ti-6AL-4V). Table 3.3 shows the elasticity parameters for ABS and Table 3.4 shows the first and last parameter for 1464 points of the plasticity data for the ABS [22, 89] . Similarly, the Table 3.5 shows the elasticity data for Titanium alloy and Table 3.6 shows the first and last point for 100 points of the plasticity stage for Titanium [57, 124, 125] . For any other possible material, text boxes are added to enter the material name and the materials elastic properties and another table to enter the materials plastic properties. Next the software will be responsible for creating the material library and the property sections to be ready for assigning the material to the models. For

the material library, the LSD will plug the elasticity properties, density, plasticity properties, and fracture criteria such as ductile damage, shear damage as shown in the Figure 3.26. Whereas, for the material section, the LSD is designed to create the section frame from the material with solid homogeneous (see the Figure 3.27). For assigning the material, the tool was designed to assign the material section to the model and create set data stored under name *Set-2* as shown in the Figure 3.28. Finally, for any other material the panel was designed so that the material properties and material name can be entered and the LSD program will adjust all the material criteria creatively. The panel and LSD code are shown in Figure 3.29.

Table 3.3 Elasticity and density parameters for the ABS

The Young modulus (MPa)	Poisson Ratio	The Yield Strength (MPa)	Density (Kg/m ³)
861.5	0.29	25.77	718.49

Table 3.4 First and Last point for Plasticity stage for the ABS

Point	Yield Stress	Plastic Strain
1	25.775	0
.....
1464	33.322	0.04555

Table 3.5 Elasticity and density parameters for the Ti-6AL-4V [125, 32]

The Young modulus (MPa)	Poisson Ratio	The Yield Strength (MPa)	Density (Kg/m ³)
104000	0.35	915.302	4017.92

Table 3.6 First and Last point for Plasticity stage for the Ti-6AL-4V [125, 32]

Point	Yield Stress	Plastic Strain
1	915.30261	0
.....
100	1201.95114	0.25

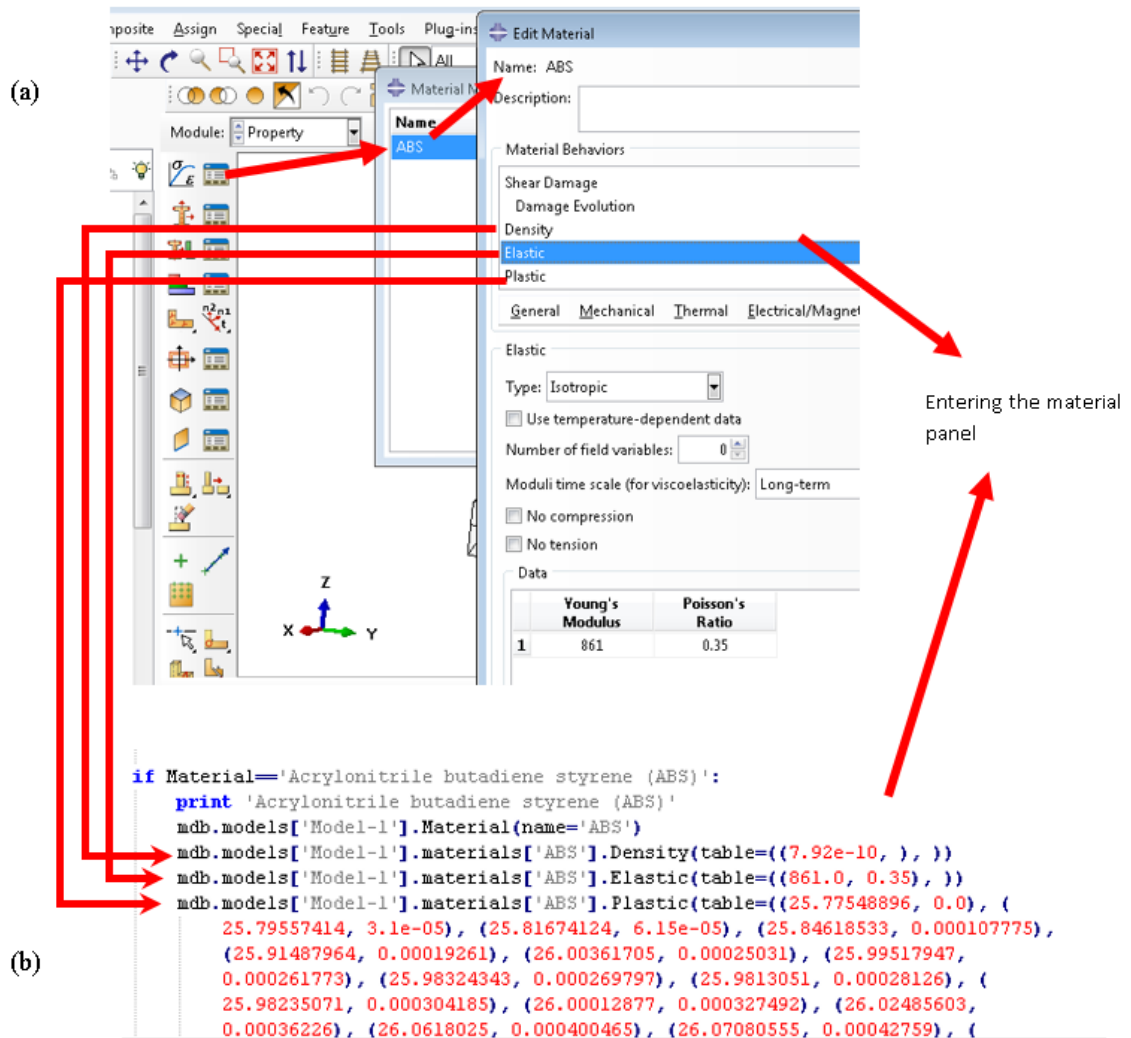


Figure 3.26 Creating Material Library (a) ABAQUS model space, and (b) Python Code

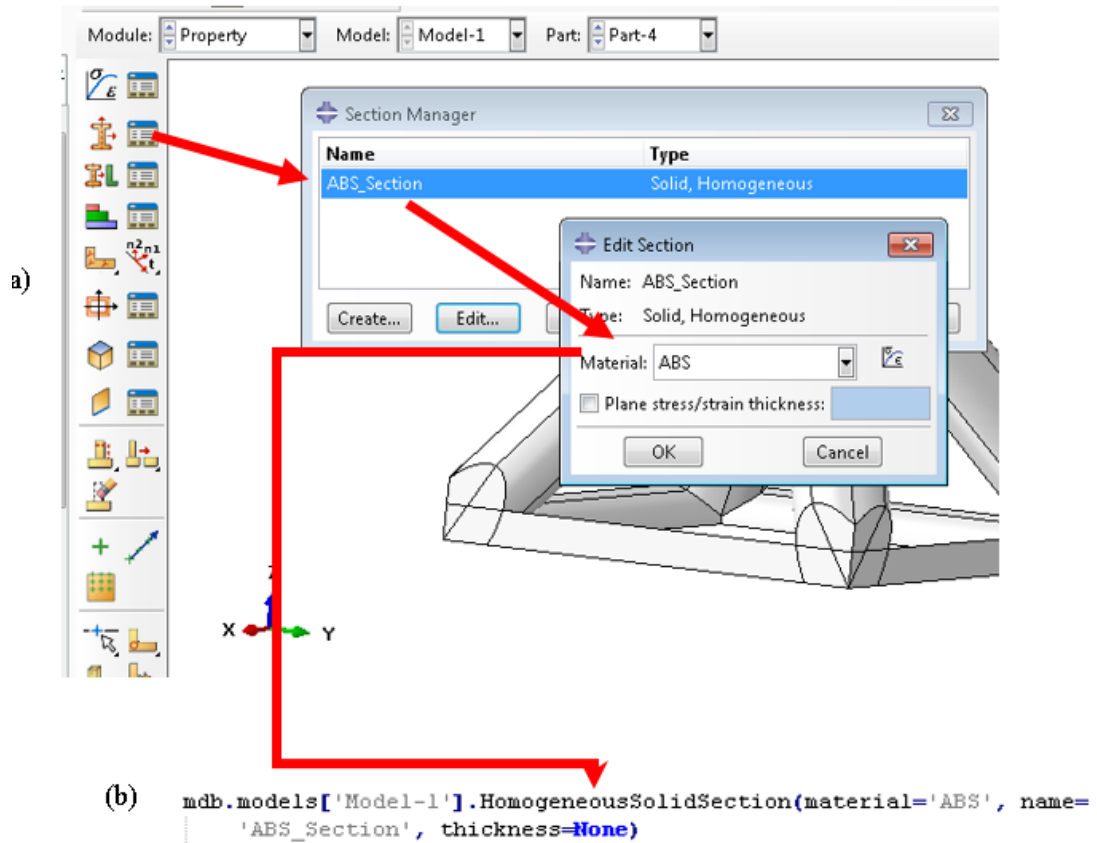


Figure 3.27 Creating Material Homogeneous section (a) ABAQUS model space , and(b) Python Code

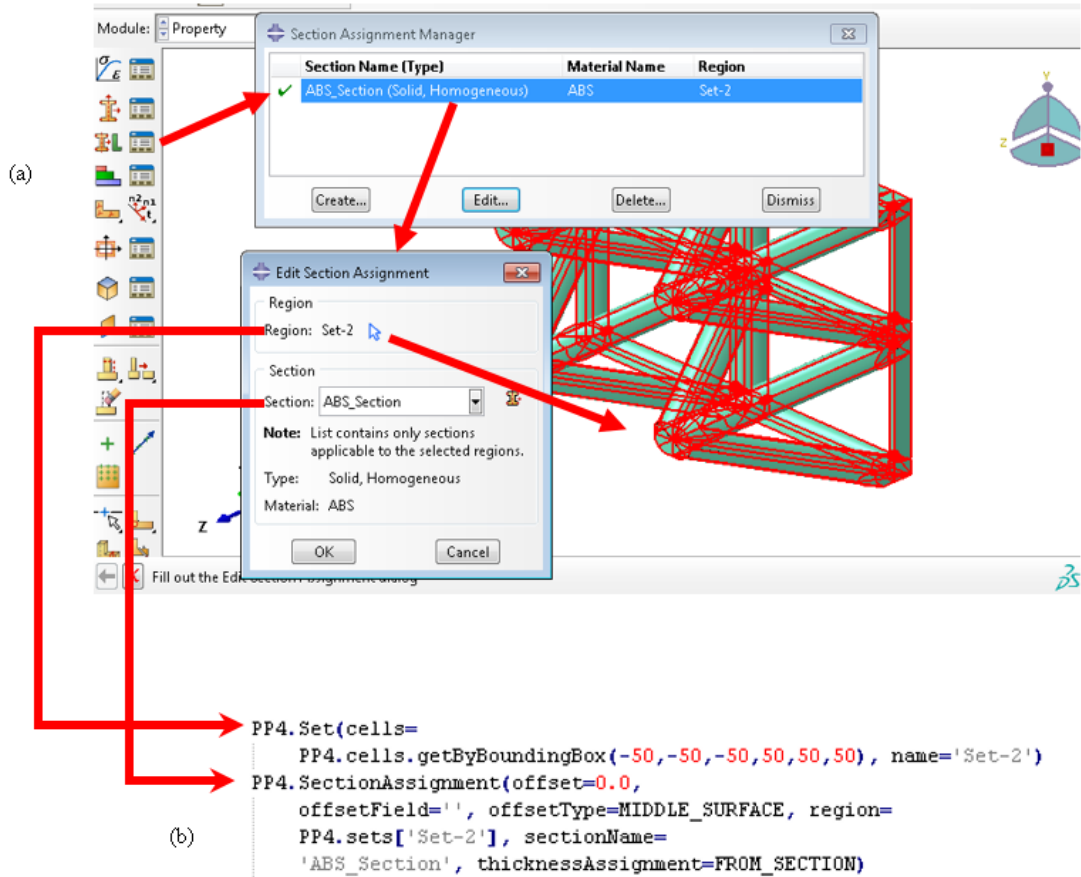


Figure 3.28 Assign the Material the Material section to the Model (a) ABAQUS, and (b) Python

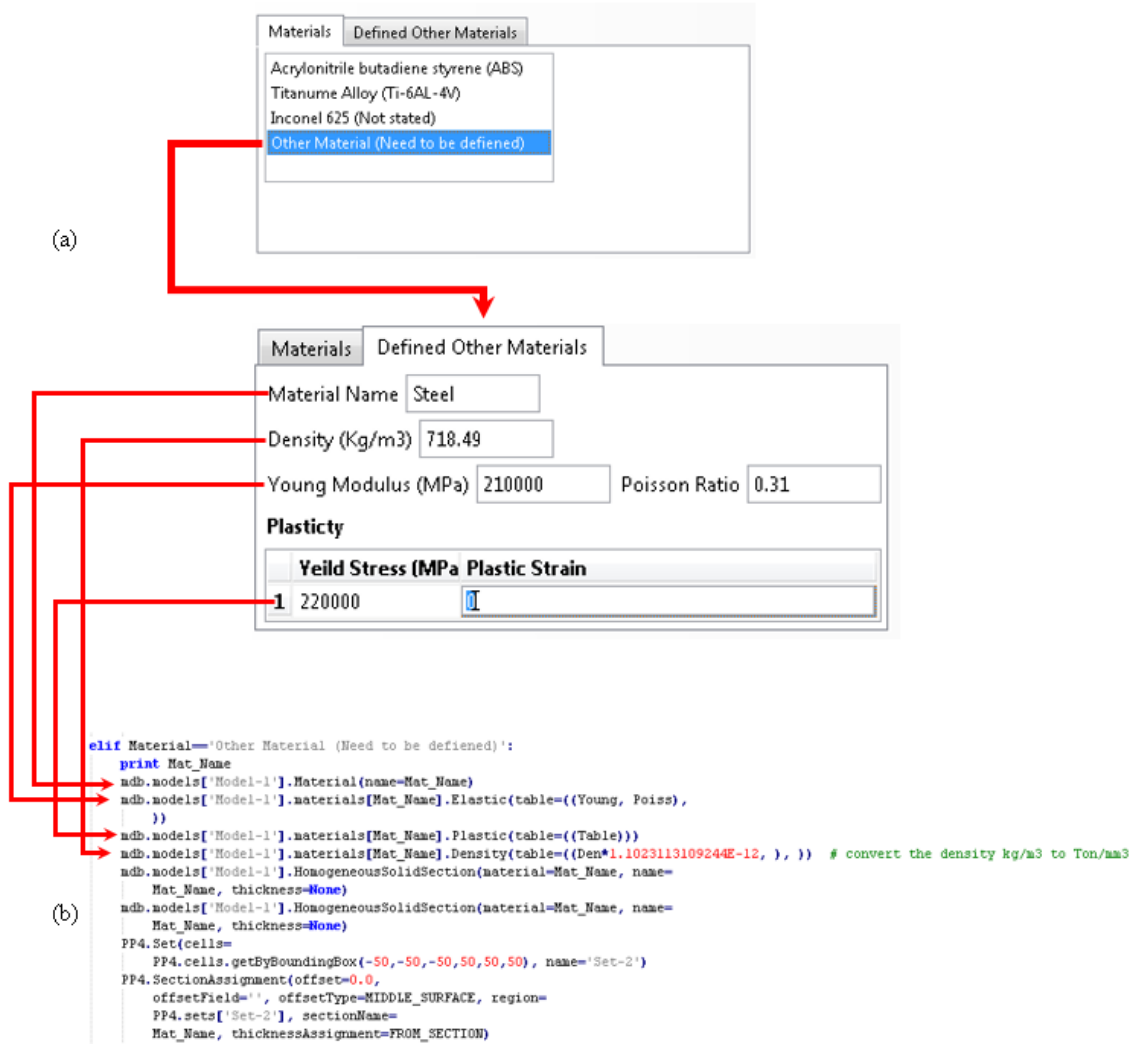


Figure 3.29 Material frame for any other Materials (a) GUI frame, and (b) Python code

3.6.11 Creating the Job for the Submission

Creating the job for submission is the final stage of the ABAQUS model development and after that the model will be ready for running. The program is designed to create the Jobs under the name *Job-e1* as shown in the Figure 3.30. After submitting the job, it usually takes approximately 40 minutes to complete the run for almost all the configurations.

```
# ***** For the job *****
mdb.Job(activateLoadBalancing=False, atTime=None, contactPrint=OFF,
description='', echoPrint=OFF, explicitPrecision=SINGLE, historyPrint=OFF,
memory=90, memoryUnits=PERCENTAGE, model='Model-1', modelPrint=OFF,
multiprocessingMode=DEFAULT, name='Job-el', nodalOutputPrecision=SINGLE,
numCpus=1, numDomains=1, parallelizationMethodExplicit=DOMAIN, queue=None,
resultsFormat=ODB, scratch='', type=ANALYSIS, userSubroutine='', waitHours=
0, waitMinutes=0)
```

Job name

Figure 3.30 Python code for assigning the Job

3.7 Summary

This chapter has discussed how to debug the ABAQUS Python code to create the LSD tool. Because the LCS models have complex geometric features, the developed Python code does all the geometrical analysis. Since creating the lattice structure models manually are difficult and tedious, this chapter has addressed how to automate Face recognition, body releasing and Smart 3D Vector. The chapter also has shown how to automate assigning the materials and creating the analysis Jobs until final stages of the models. The next chapter will address how to install and run the LSD tool and discuss the results validations.

Chapter 4. Application and Validation of LSD Tool

4.1 Overview

Chapter 3 addressed the development and application of LSD tool and the associated background behind its development. The tool is an ABAQUS plugin coded in Python. It is capable of performing geometric formulations, face recognition, and body realization. It allows the creation of lattice models with ideal parameters such as elements size and the boundary conditions. In this chapter, it will be discussed how to install and run the LSD tool to capture the results for the compression tests. Additionally, the results will be validated with the experimental tests demonstrated in previous studies. Finally, we will pick two configurations based on the feasibility of construction using 3D printing and the stability of the load-displacement curves. These configurations will be analyzed based on the progressive failure and absorbed energy.

4.2 Tool Installation

Installing the LSD tool is very simple and similar to installing the micromechanics plug-in tool. One just needs to copy the folder *Fadeel* to the directory *ABAQUS /plugins* in the system. Once the ABAQUS software is started, it will check the *Plug-in* menu and the icon *Fadeel* will be visible as shown in the Figure 4.1.

4.3 LSD Tool Running

When click in the tool icon, it will show the Lattice Structure Designer text box as shown in the Figure 4.2. The tools were designed to have four consecutive option boxes based on the configuration types and materials. First, we need to select the configuration type as shown in the configurations list. The next step is to plug the configuration parameters such as the strut diameter, the unit cell dimensions. Next, choose the type of array or cells strut diameter, the unit cell dimensions. Next, choose the type of array or cells distribution. Finally, choose the materials if the material available in the library, and if the material not available one can enter the material characteristics by using the box to define the other material (see the Figure 4.3). For the BCC, BCCV, and BCCA parameters are located at group 1 in the program, for the Tetra and Tetrahedron are located in group 2, whereas the Pyramidal is located at group 3 (see Figure 4.3). According to the figures the dimensions needed for each configuration can be entered into the text boxes when prompted by LSD.

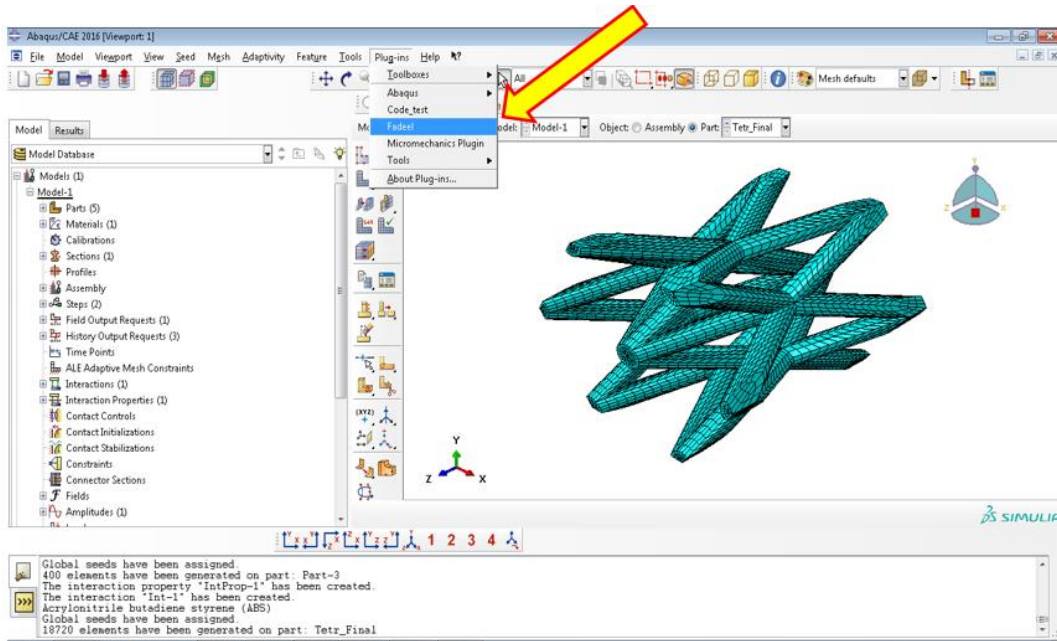


Figure 4.1 Run the LSD tool

4.3.1 First Group (BCC, BCCV, and BCCA)

Because the configurations called BCC, BCCV, and BCCA are basically body centric cubic, they will require similar unit cell dimensions. In this case, we only need the dimension of the unit cell in X, Y, and Z and the number of cells in X, Y, and Z directions and the strut diameters. Then the configuration will be built automatically. For example, the 5x5x4 cell configurations for BCC, BCCV, and BCCA with unit cell dimensions of 5x5x5 mm, and strut diameters of 0.5 mm created using LSD are shown in Figure 4.4, Figure 4.5 and Figure 4.6, respectively. All of the models were created with the ideal mesh convergence.

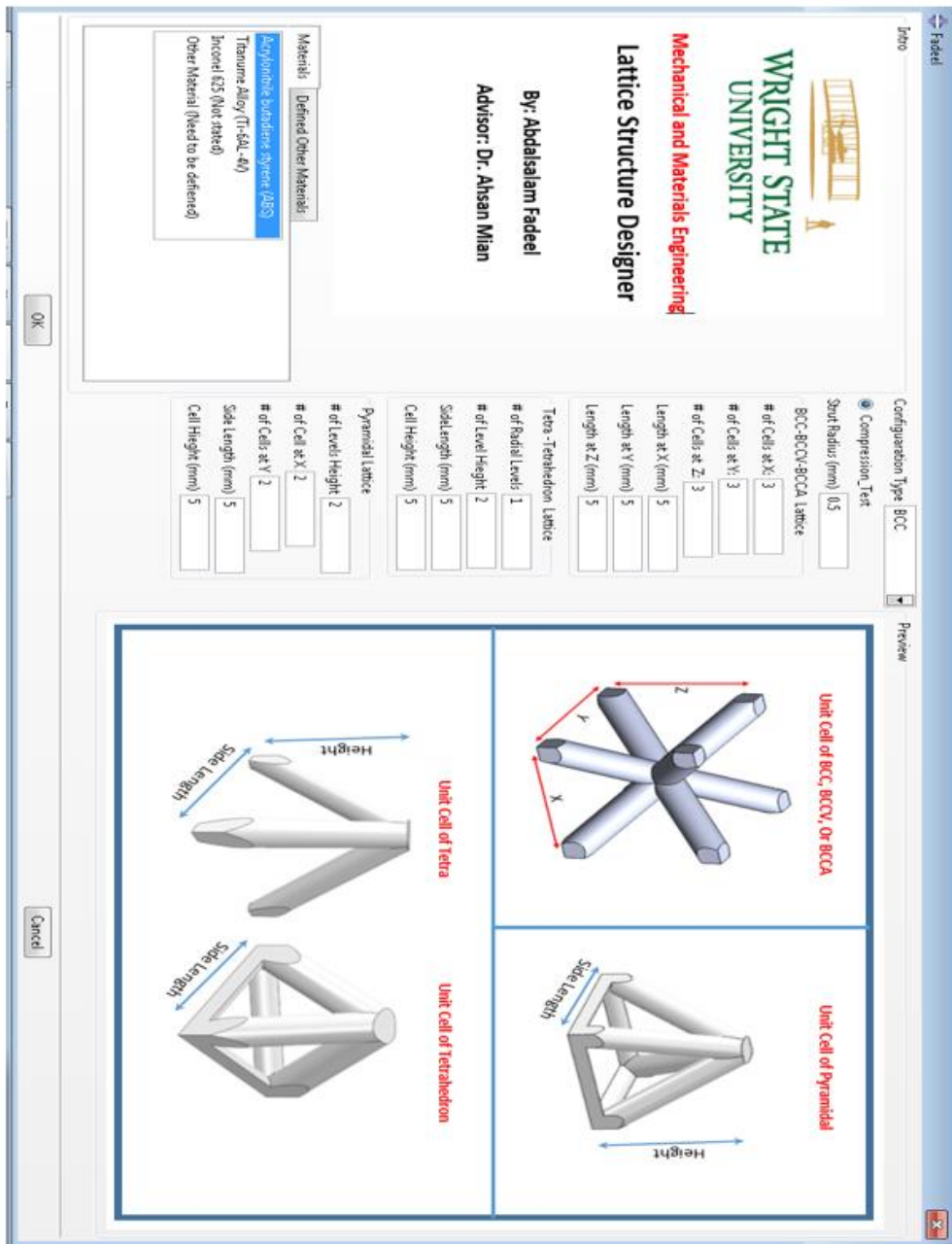


Figure 4.2 Fadeel tool interface main menu

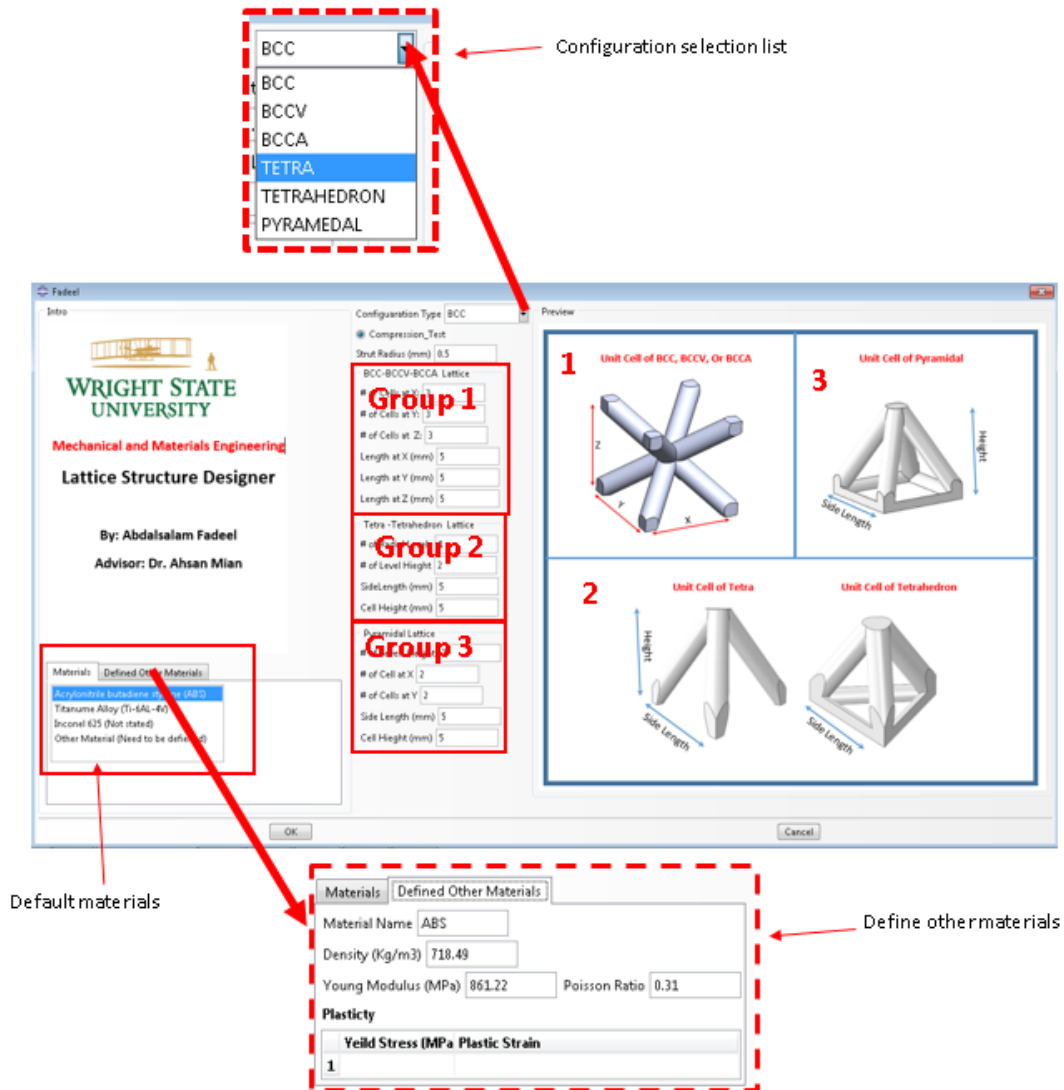


Figure 4.3 The Tool interface details

Figure 4.3 The Tool interface details

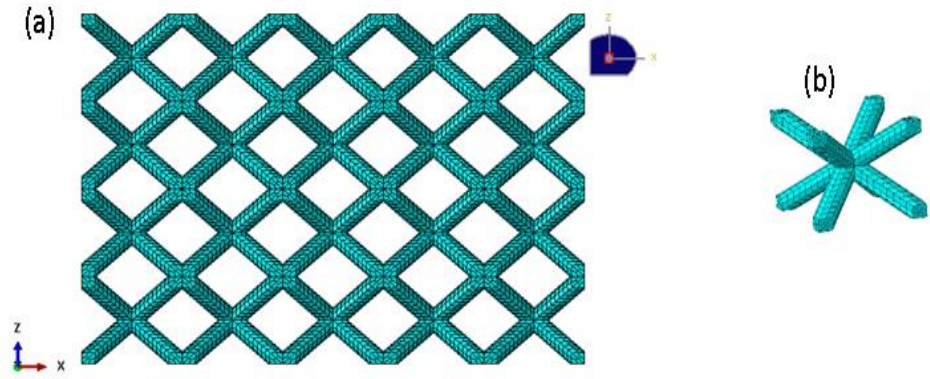


Figure 4.4 BCC result from Fadeel Tool, (a) Entire lattice ,and (b) one cell

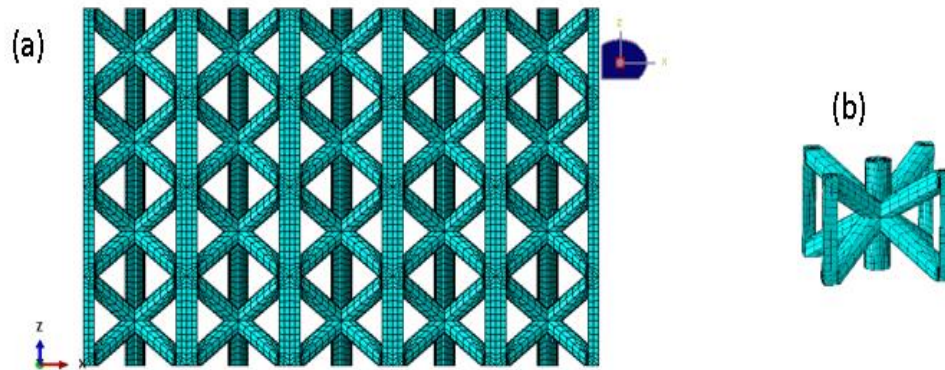


Figure 4.5 BCCV result from Fadeel Tool, (a) Entire lattice and (b) one cell

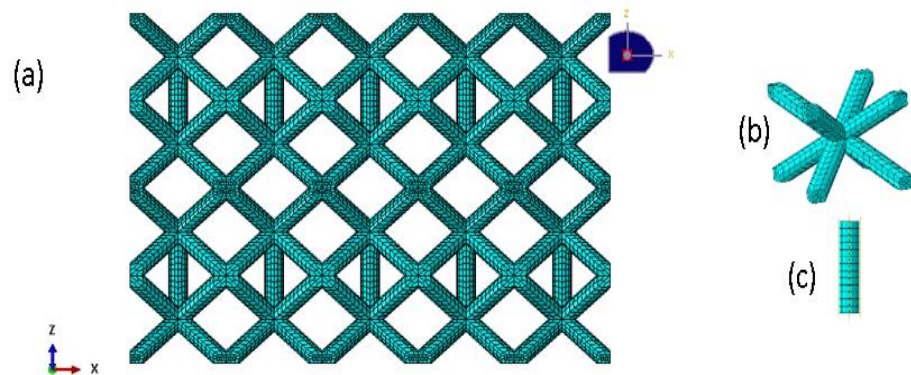


Figure 4.6 BCCA result from Fadeel Tool, (a) Entire lattice (b) one cell and (c) Alternative Vertical strut

4.3.2 Second Group (Tet and TetH)

To create both Tet and TetH structures, we need only the side length, the height, and the strut diameter of the unit cell (see Figure 4.3 for the Tetra and Tetrahedron). However, for the entire configuration, we need to identify the number of radial levels and the number of vertical levels for both Tetra and Tetrahedron. For example, if we need to create the configuration with 4 cells height and 2 radial level the results will be as Figure 4.7 for the Tetra and Figure 4.8 for the Tetrahedron configurations.

4.3.3 Third Group (Pyr)

The pyramidal configuration is very similar to the BCC group except the unit cells are flipped relative to each other in the Z direction. The pyramidal structure requires the side length and height for unit cell to be determined specifically for this configuration. For the entire configuration, it is required to enter the number of cells in X and Y as well as the levels in Z. For example, the Pyramidal configuration with the 5x5x4 and unit cell with side length 5mm and height 5 mm created using the LSD tool will be the one shown in Figure 4.9.

4.4 Assigning the Materials

The most common printed materials are ABS and Ti-6Al-4V and were identified to be the default material. For any other materials, the user can enter the material properties as shown in Figure 4.10. For example, if you want to use any other material such as Steel, 210 GPa, 0.33, and Yield 220 GPa, you can type the name as Steel and other available material parameter.

4.5 Submitting the Job

The program will create the ABAQUS Job so that it is ready for submission. It will require a longer run time as shown in the Figure 4.11. After that it will be ready to display the results as shown in the following sections.

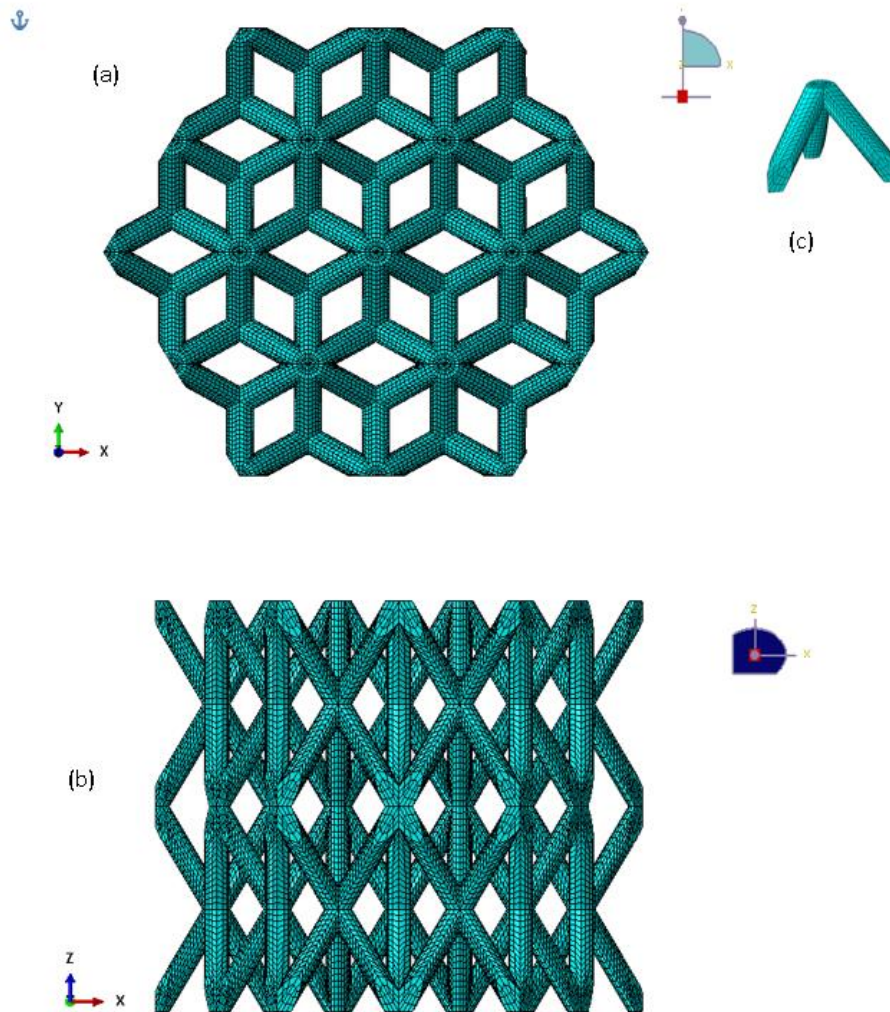


Figure 4.7 Tetra with ideal mesh result from Fadeel Tool, (a) top view (b) side view, and (c) One-unit cell

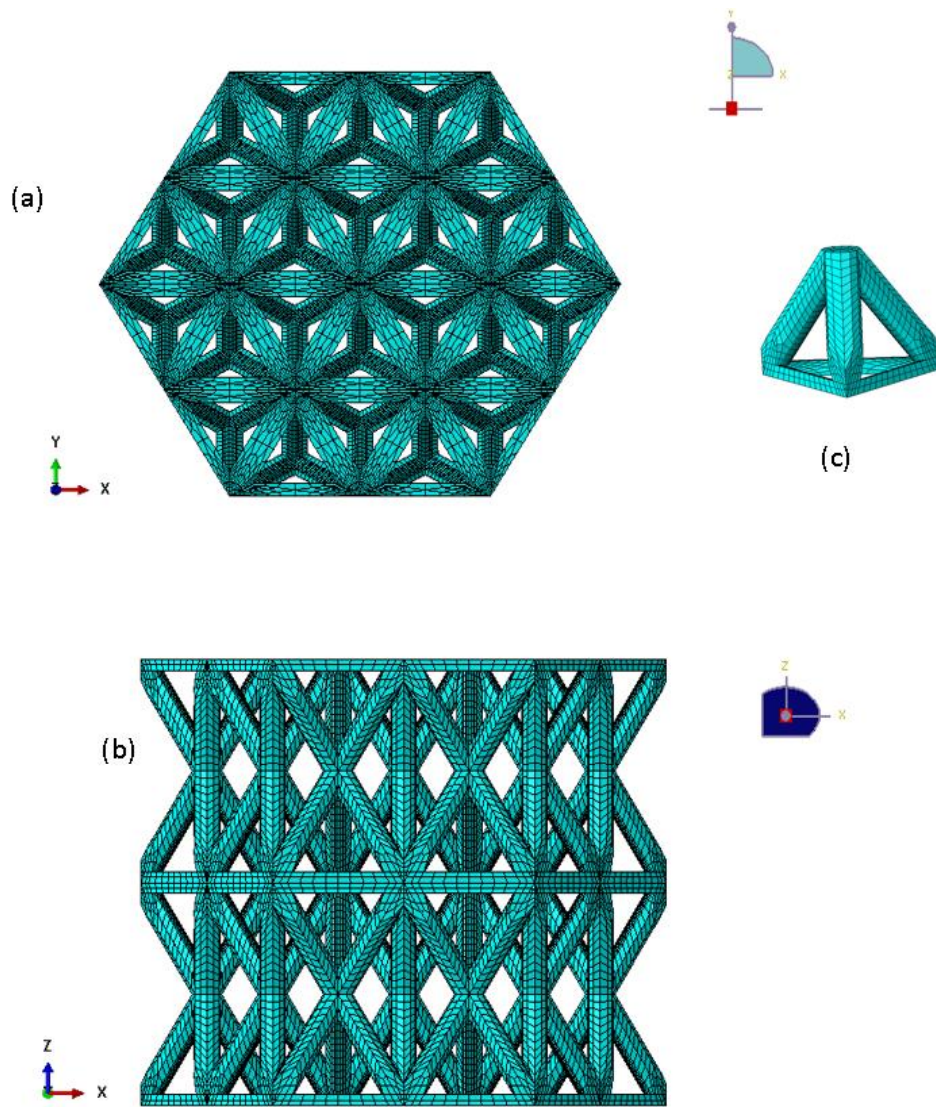


Figure 4.8 Tetrahedron with ideal mesh result from Fadeel Tool, (a) top view (b) side view, and (c) One-unit cell

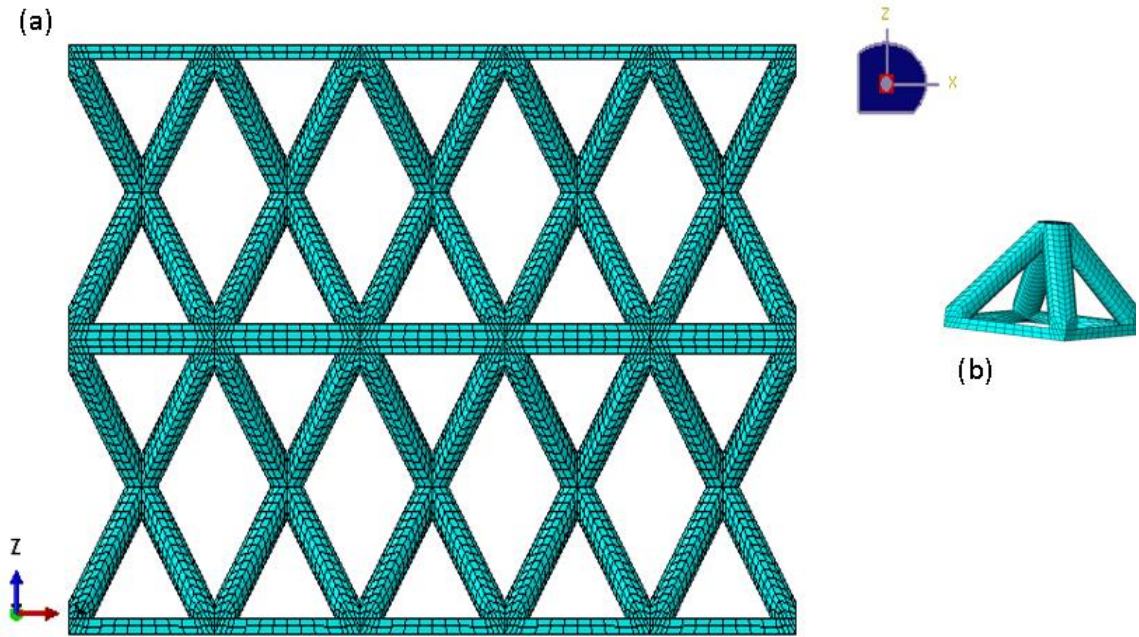


Figure 4.9 Pyramidal with ideal mesh result from Fadeel Tool, (a) Entire Lattice and (b) One-unit cell

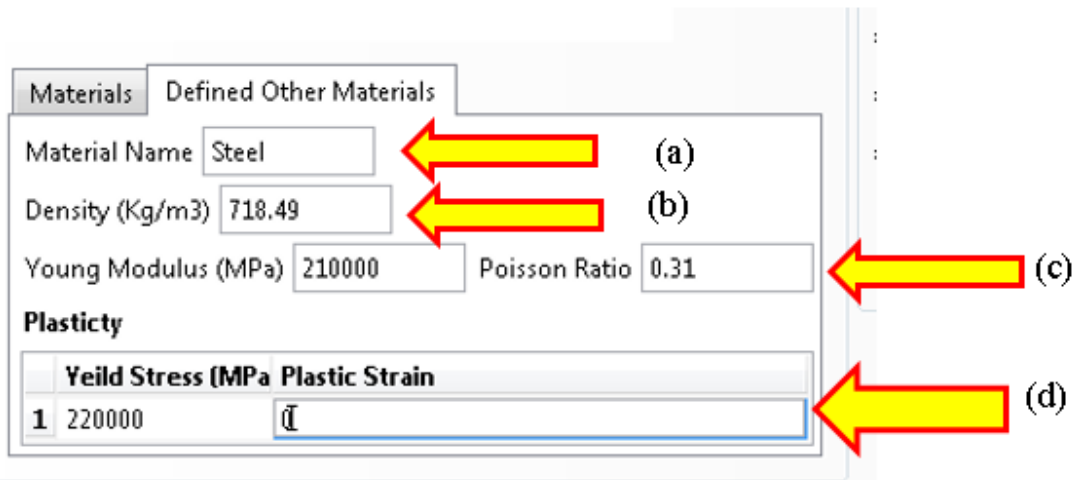


Figure 4.10 Assigning the materials (a) name (b) density (c) Elasticity, and(d) Plasticity

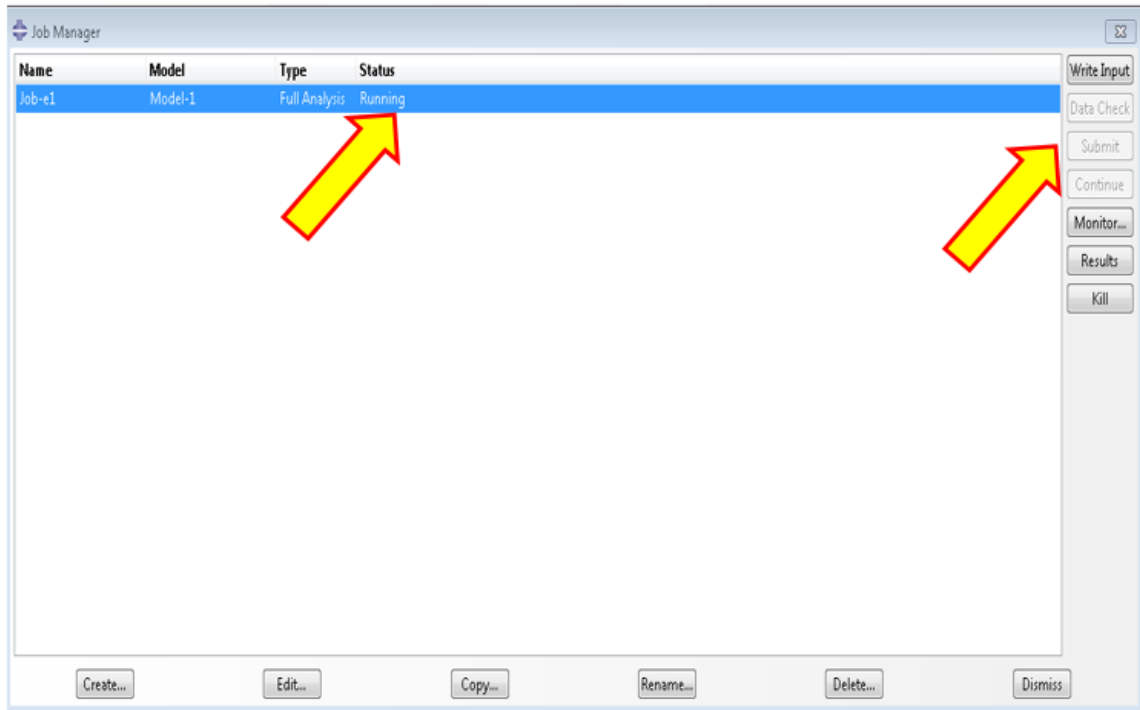


Figure 4.11 Submission and running the Job

4.6 The LSD Outputs

After the job run completes, the data will be saved in Output Database (*.odb) files. These files usually take the same name of the Job and can be accessed and edited by ABAQUS. It is recommended to copy all these data to excel or MATLAB code for further plotting and analysis. The following subsections show the results for each configuration.

4.6.1 Model Validation for the BCC Configuration

The load-displacement curves obtained experimentally and from FEA for BCC are shown in Figure 4.12. It is observed that the ABAQUS FEA results agree reasonably well with the experimental observations. All the plots show multiple progressive stages. The FEA result shows that there are four peaks based on the number of the collapsed layers.

The highest possible compressive load is 540 (N), and the lowest is 300 (N). However, this configuration will not be taken for the further study because of the low compressive load.

- For the BCC
- The experimental vs FEM

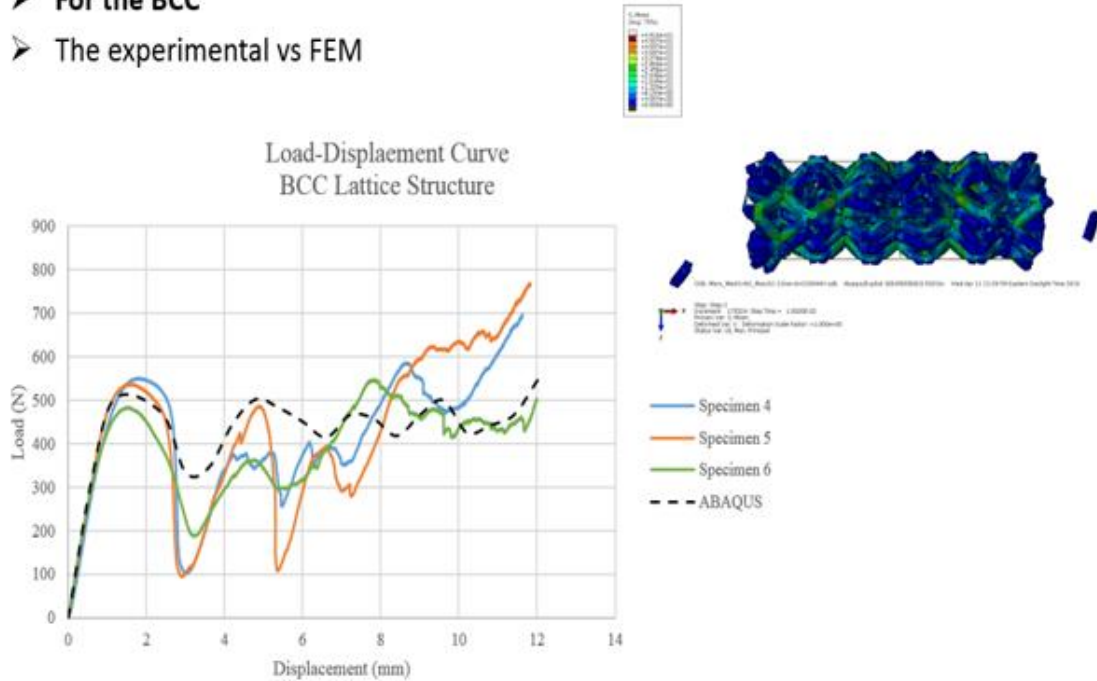


Figure 4.12 BCC model for post-yielding and experimental comparison

4.6.2 Model Validation for the BCCV Configuration

Figure 4.13 shows load-displacement plots for BCCV and a good agreement between the finite element model and the experimental results is observed. Both the FEM model and the experimental results have shown that there are two major peaks in the graph due to the collapse of the vertical struts and multiple minor peaks due to multi collapse of the layers. However, the experimental result did not reach the densification as predicted in

the FEM. Because of the higher compressive load, this configuration will be considered for further study.

➤ For the BCCV

➤ The experimental vs FEM

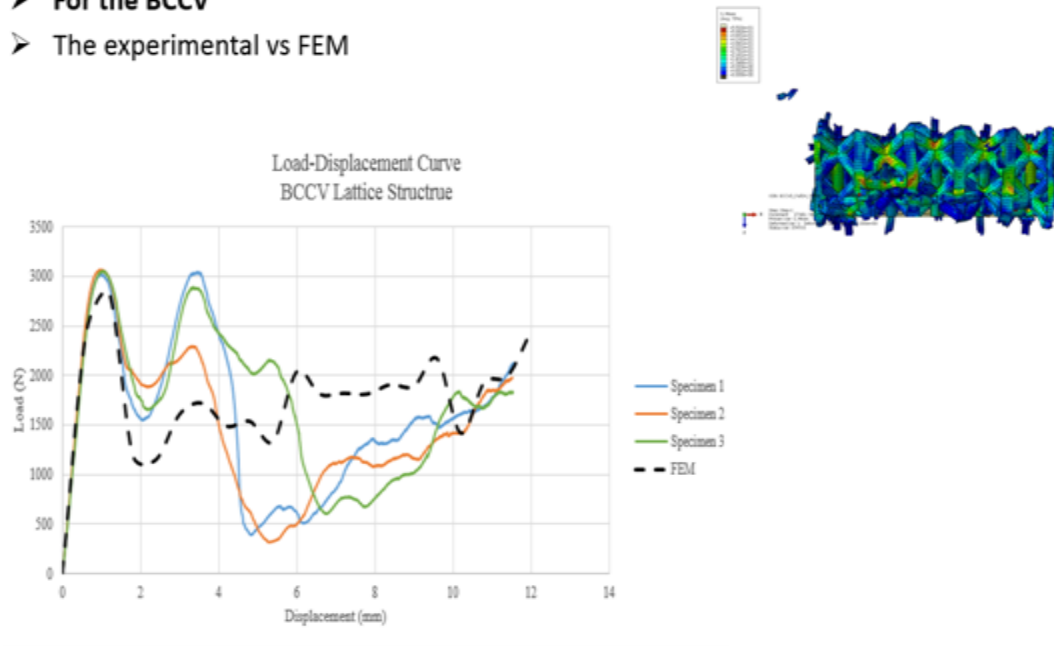


Figure 4.13 BCCV model for post-yielding and experimental comparison

4.6.3 Model Validation for the BCCA Configuration

The FEM and the experimental results for BCCA are in agreement as shown in Figure 4.14. This configuration has shown the load-displacement behavior similar to the BCC configuration in the progressive failure mode; however, BCCA has higher peak load because of the alternative vertical struts. Since the compressive load is 1000 (N) which is a little smaller than expected, this configuration will not be taken for further study.

- For the BCCA
- The experimental vs FEM

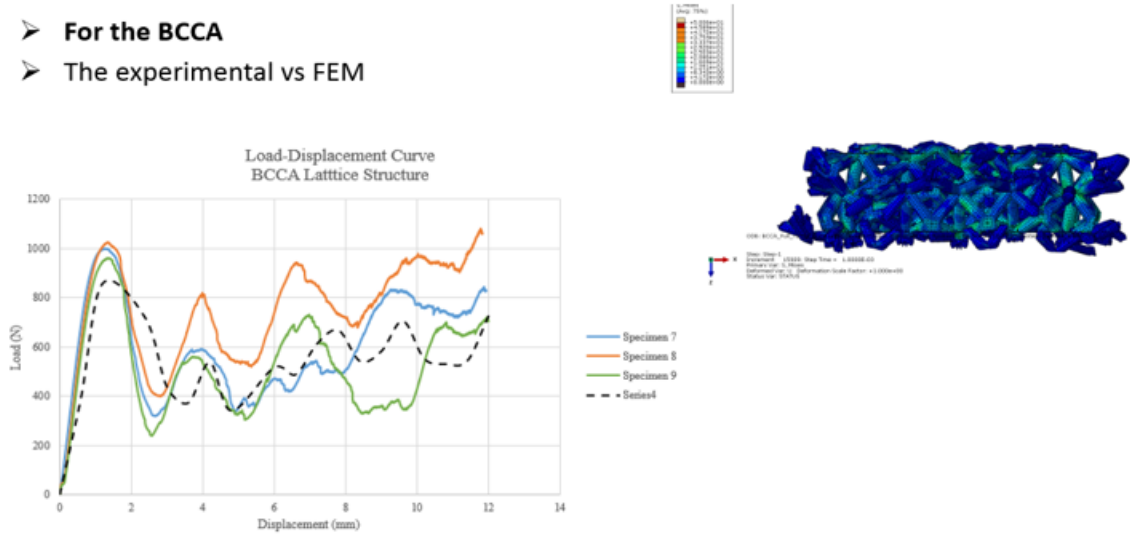


Figure 4.14 BCCA model for post-yielding and experimental comparison

4.6.4 Model Validation for the Tetra Configuration

The FEM has shown good agreement with the experimental results as shown in Figure 4.15. The first peak was because of the resisting struts. However, after this there is a huge drop from peak down to zero (0) (N) in the experimental data. Because of that, this configuration will not be considered for further analysis.

- For the TETRA
- The experimental vs FEM

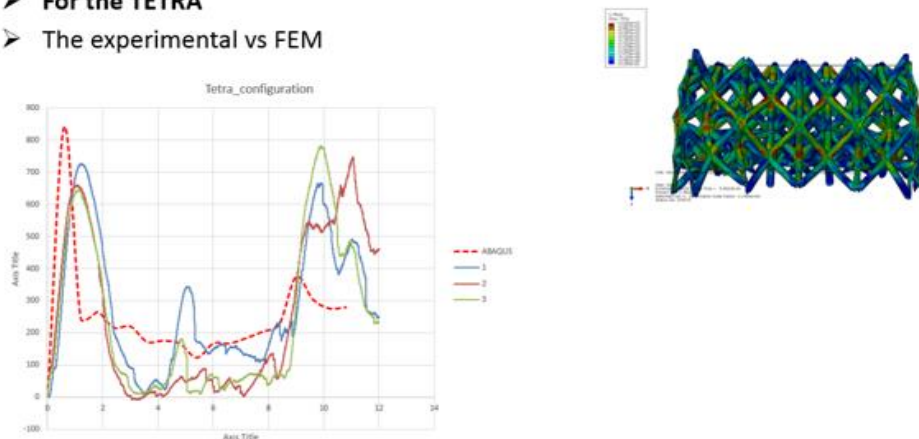


Figure 4.15 Tetra model for post-yielding and experimental comparison

4.6.5 Model Validation for the Tetrahedron (TetH) Configuration

The load-displacement plot obtained from FEM for TetH has shown good agreement with the experimental results as shown in Figure 4.16. The First peak was due to the horizontal struts failure and this configuration bears compressive force of more than 3200 (N). Because of the stability of this configuration and its higher compressive load, this configuration was recommended to be selected for further study.

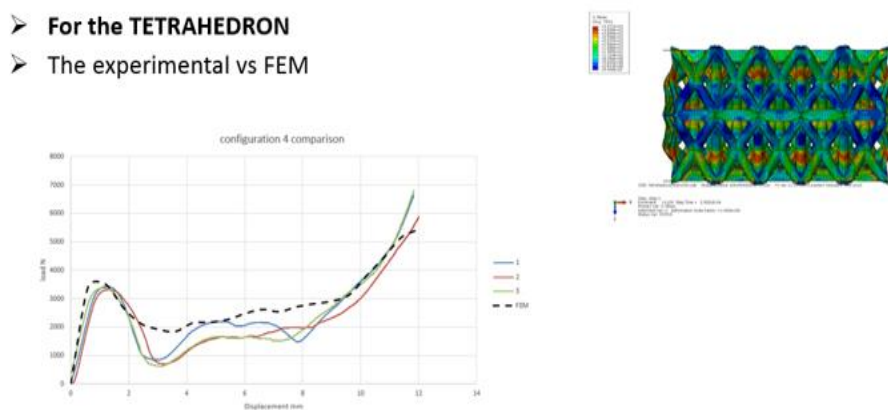


Figure 4.16 Tetrahedron model for post-yielding

4.6.6 Model Validation for the Pyramidal Configuration

The load-displacement behavior of the pyramidal configuration is shown in Figure 4.17. It is clear from the plots that the FEM results are in good agreement with the experimental results. It is observed that, there is a huge drop of resisting load after the first peak due to the collapse of the horizontal struts and hence this configuration will not be considered for further study.

- For the Pyramidal
- The experimental vs FEM

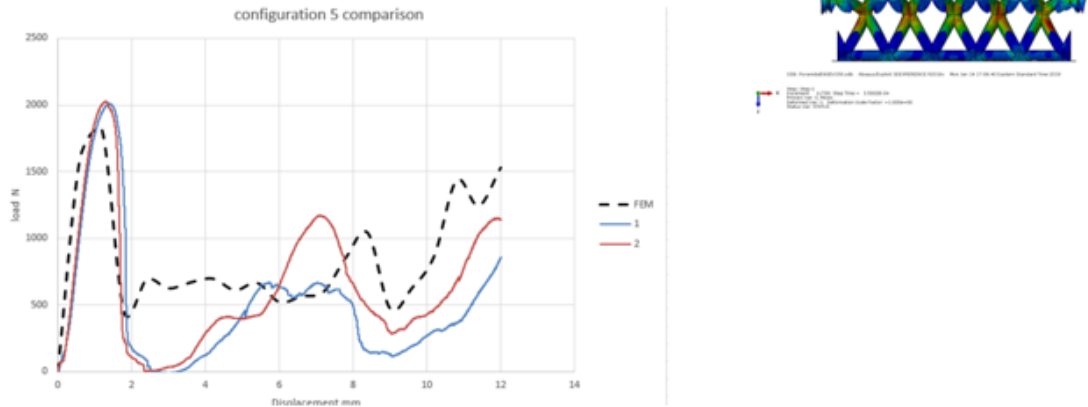


Figure 4.17 Pyramidal model for post-yielding and experimental comparison

4.7 The LSD Tool Validation

According to the experimental and FEM results for the post-yielding load-displacement behavior for the 6 configurations tested in this study, the finite element models have successfully provided the information and simulation for the elastic-plastic stages. The FEM also captured the progressive damage reasonably correctly for all configurations. The FEA predicted load-displacement trends appear to capture relatively well during the entire loading process.

4.7.1 Comparison of FEM with Experimental Results for ABS

Table 1 shows the comparison between the experimental and FEM results based on the Young's modulus, lattice yield stresses, and peak loads. The percentage error appears to be very small for four configurations and relatively large for Pyr and Tetra configuration. It is obvious that the FEA models have provided acceptable simulations for the progressive damages and post-yielding behaviors of the lattice.

Table 4.1 Comparison of FEA results with the experimental counterpart along with associated Errors

LCS	Young's modulus (MPa)			Lattice yield stresses (MPa)			Peak load (N)		
	Average experiment	FEA	Error	Average experiment	FEM	Error	Average experiment	FEM	Error
BCC	13.46	14.19	5.14%	0.807	0.813	0.74%	515.5	470.29 2829.1	-9.61%
BCCV	110.46	87.166	21.08%	4.72	4.63	1.9%	3050.50	6	3.97%
BCCA	24.21	22.86	2.58%	1.49	1.372	8.29%	995.33	716.20	28.04%
Tetra	36.59	41.80	-14.23	1.162	1.344	-15.28%	840.336	721.50	14.16%
TetH	143.679	151.61	5.23%	5.13	5.13	-0.01%	3372.12	3361.2	-0.32%
Pyr	69.91	85.06	17.81%	2.55	2.95	13.42%	2013.2	1825.3	-10.29%

4.7.2 Comparison with Published FEM Results for Titanium Alloy

In terms of checking the validity of the LSD tool with other possible materials, the model has been validated with the BCC lattice structure made from the published Titanium alloy (Ti-6Al-4V). In this case, the results from our LSD/ABAQUS model were compared with the previously published FEM results for Ti-64. According to Kadkhodapour and others, the finite element model for the Titanium alloy was developed for 8 configurations [126, 42]. Based on the criteria they used, the BCC lattice structure with 4x4x4 cells was chosen as shown in Figure 4.18 for further analysis. The unit cell dimension was 5mm with strut diameter of 0.2 mm. The model developed using the LSD tool was run in ABAQUS and was compared with Kadkhodapour's results. According to the results as shown in Figure 4.19, both models have shown acceptable agreements. Therefore, it can be said that the developed LSD/ABAQUS finite element model is effective for Titanium in addition to ABS. Therefore, the LSD tool has promise for any other materials for the lattice structure engineering design.

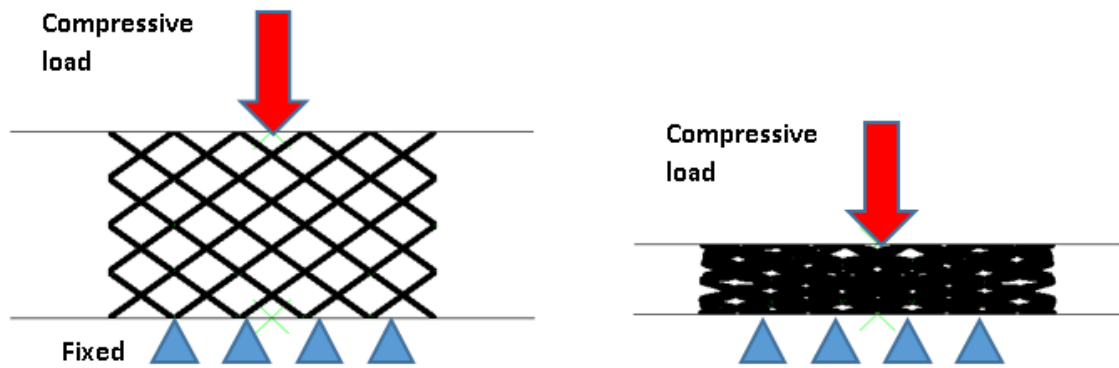


Figure 4.18 FEM model for the Titanium model

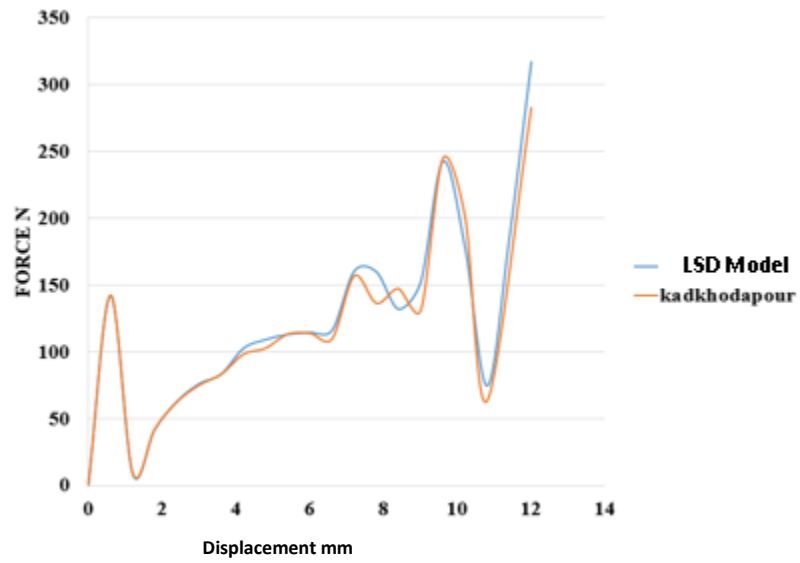


Figure 4.19 Ti-6Al-4v models by LSD and Kadhodapour comparison

4.8 Summery

This chapter has addressed how to run LSD for all the six LCS configurations. All the results were captured based on quasi-static compressive models. The results have shown good agreement with previous experimental tests for the ABS and with another model for the Ti-6Al-4V alloy. The models have good ability to capture and simulate progressive damage stages during the entire loading process. Based on their ability to bear the compressive load and resist fracture the BCCV and Tetrahedron lattices were chosen for the next chapter to further analyze the failure mechanisms and absorbed energy of the structures.

Chapter 5. Progressive Damage Analysis

5.1 Overview

Chapter 4 addressed the application of the LSD tool to capture the load-displacement curves for six configurations (BCC, BCCV, BCCA, Tetra, and Tetrahedron). In terms of looking for the most feasible configuration based on the highest compressive load and stability in the failure progression, it has been recommended to elect the BCCV, and Tetrahedron configurations for the fracture mechanism analysis and absorbed energy. In this case, both configurations were evaluated and analyzed based on the Gibson-Ashby model. These models will be addressed in this chapter. The stress-strain curve was identified by dividing the compressive load with the specimen cross section area for the stress and the displacement with the specimen height for the strain.

5.2 Ashby and Gibson Failure Stages Model Background

According to Ashby and others, there are three possible collapse regions. The Gibson model is defined by dividing the micro-mechanical structure of a lattice into 3 regions: linear elastic, plateau region, and densification [98, 99]. However, the drawback of the Gibson model is with detailed information on the microstructure of the foam, because the Gibson model includes the density [98].

The Gibson-Ashby model defines lattice failure into three stages: Linear elastic, Plastic collapse (Plateau stress), and densification regime as shown in the Figure 5.1 [100, 101]. Therefore, it is necessary to find model to understand the relation between the cellular topologies and the mechanical responses.

Over 20 years many fracture models have been developed and through these models three aspects have always been investigated: structure, material constitutive equations, and better numerical control [102]. Numerical simulation is preferred for the studies more than the experimental for many reasons; low cost, and practicality [102]. For this reason, the numerical analysis is used to compare deformation mechanisms and mechanical properties against observed conditions in experimental work. However, in terms of getting higher accuracy, the higher order of the formulation and small-time frame can improve the quality of the results [104]. The numerical model has helped to observe how Young's moduli and the mechanical properties of the studied lattice can vary or change due to the influence of the topologies and boundary conditions [44] . Because modeling of the fracture is very sensitive to the elements, the element formulation has to be chosen and validated carefully [105, 106]. Also, the mesh orientation has to be taken into account for the effect on the crack pattern, also to the resolution of the model [106, 107]. It was proven that the brick elements are more efficient than the tetrahedral elements for many reasons including a higher degrees of freedom and higher degree of the formulation [22, 81, 82].

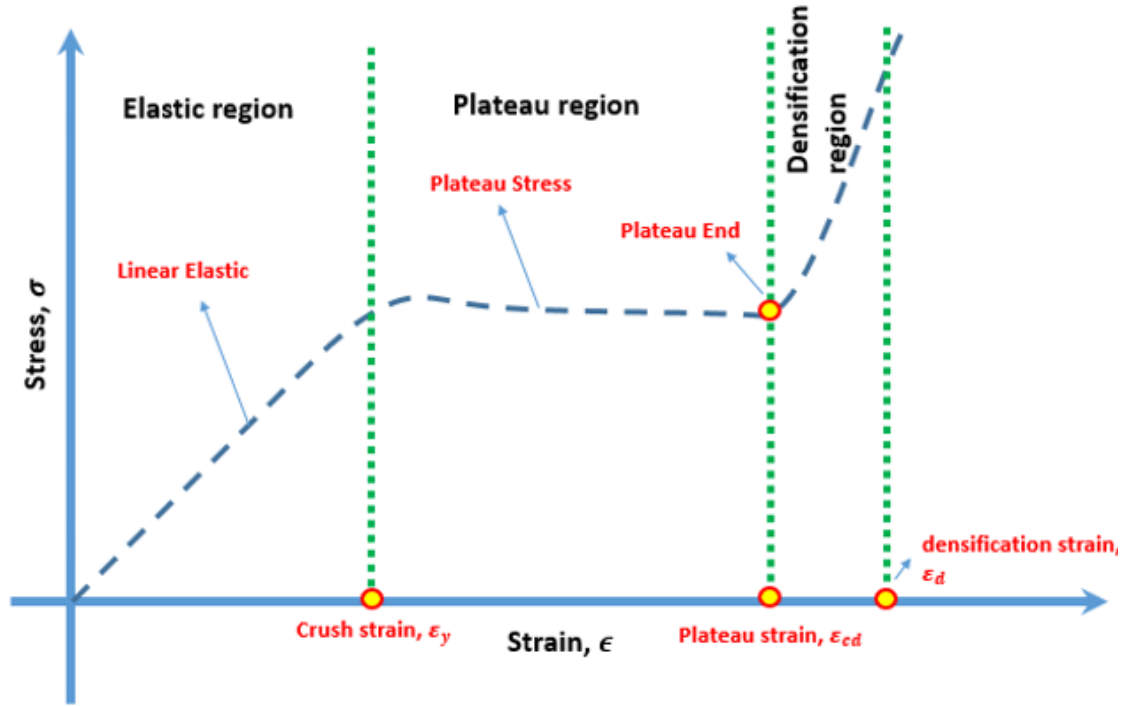


Figure 5.1 schematic Ashby and Gibson failure stages for the lattice form for the compressive stress strain behavior.

5.3 Progressive Damage Analysis for BCCV

Both the experimental work and the finite element model have shown good agreement in terms of the elastic modulus and first peak load. The stress-strain plots were computed for every configuration by dividing the compressive load with the specimen area for the stress and the displacement with the specimen height for the strain. The BCCV configuration's layers have been classified into four layers based on the BCC cells and the layers were denoted as L1 for layer 1 and L2 for layer 2 and so on. They were further subdivided into section x and y for the planes xz and yz, respectively as shown in Figure 5.2 for the pre-stages. For stage 1 as shown in the Figure 5.3, when applying the load as monotonic displacement the yield point was captured at the strain of 0.06 and the corresponding stress is 4.633 MPa. The modulus of elasticity was 77.23 MPa. The First

stage of the failure is the collapse of all the vertical struts. Due to this abrupt failure the stress drops to 1.847 MPa. The section X and section Y and the side view have shown the shear damage that took place on the vertical struts. Stage 2 to stage 3 will be between the strain values of 0.09 to 0.12, and during this stages all the vertical struts will collapse at the shearing stresses as shown in the Figures 5.4 and 5.5. The next stage (stage 4), the configurations will resist depending on the regular struts and the stress will raise up to 3.668 MPa at the strain of 0.1799 for the second peak. In Stage 5 and stage 6, the L4 layer will collapse and then Layer 3 and the stresses will be dropped to 2.256 MPa and 2.62 MPa respectively. In stage 7 there is will be huge drop in the stress to 1.24 MPa. This drop is due to damage of all layers before starting developing the densification for the stages 7 to 9 as shown in Figures 5.9 to 5.10.

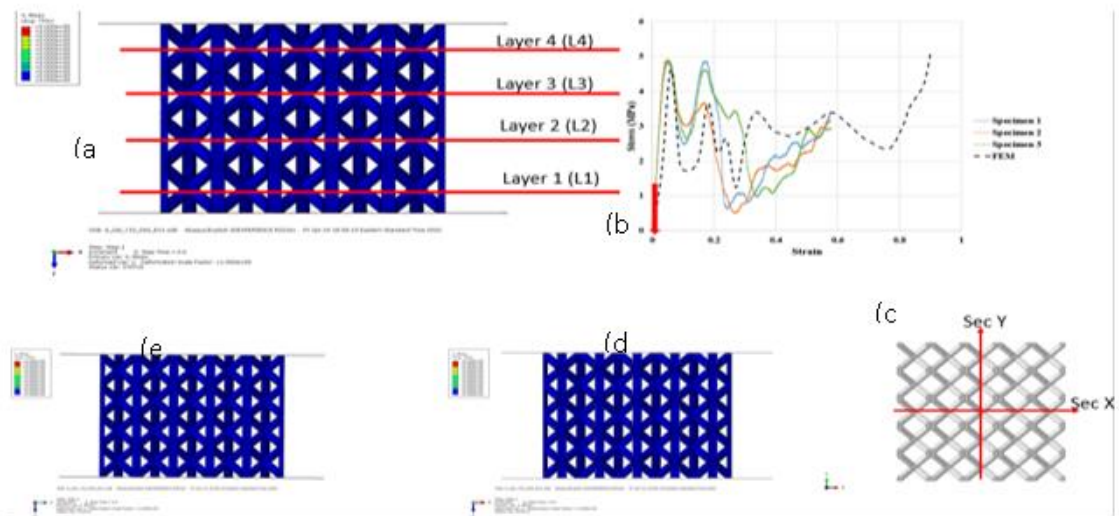


Figure 5.2 BCCV initial stage with (a) Side view (b) Location in the curve (c) Top plan (d) Section x, and (e) Section y.

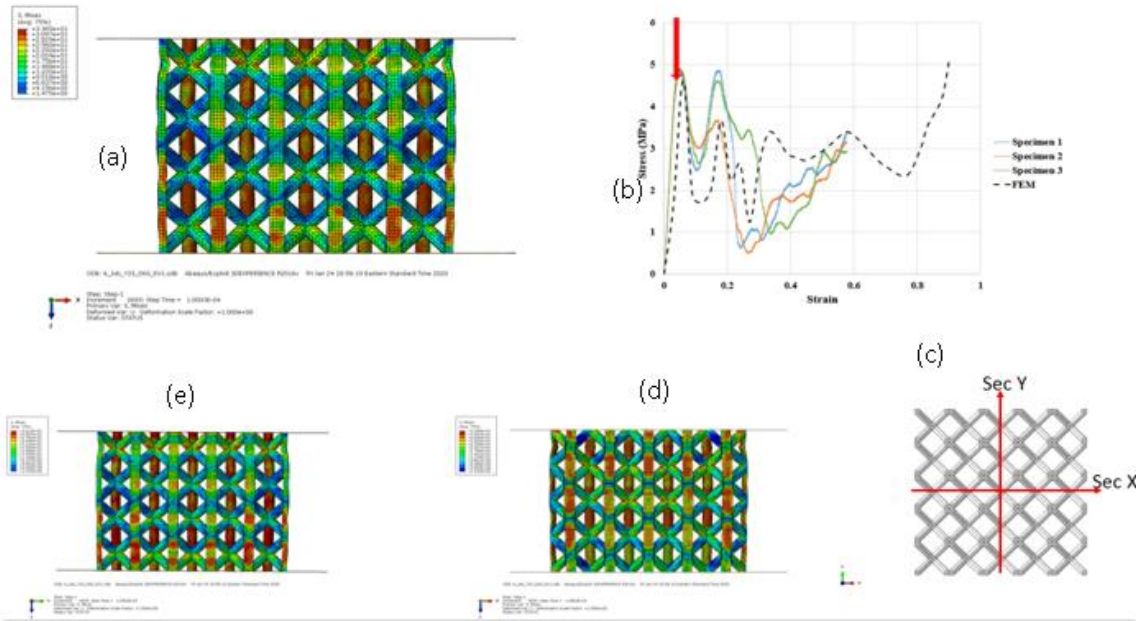


Figure 5.3 BCCV stage(1) with (a) Side view (b) Location in the curve (c) Top plan (d) Section x ,and (e) Section y.

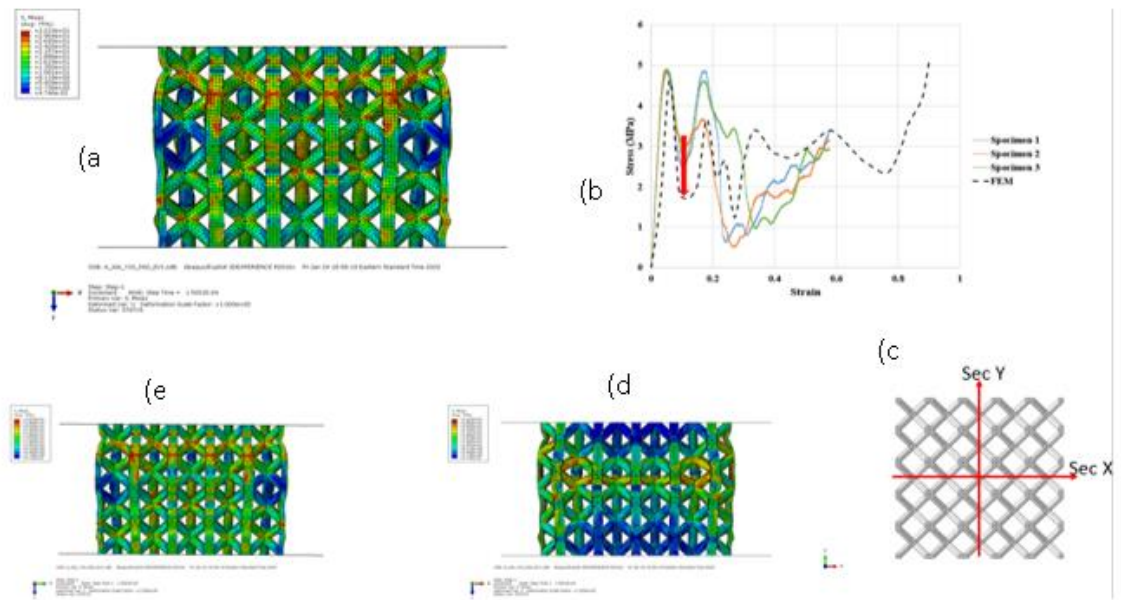


Figure 5.4 BCCV stage(2) with (a) Side view (b) Location in the curve (c) Top plan (d) Section x ,and (e) Section y.

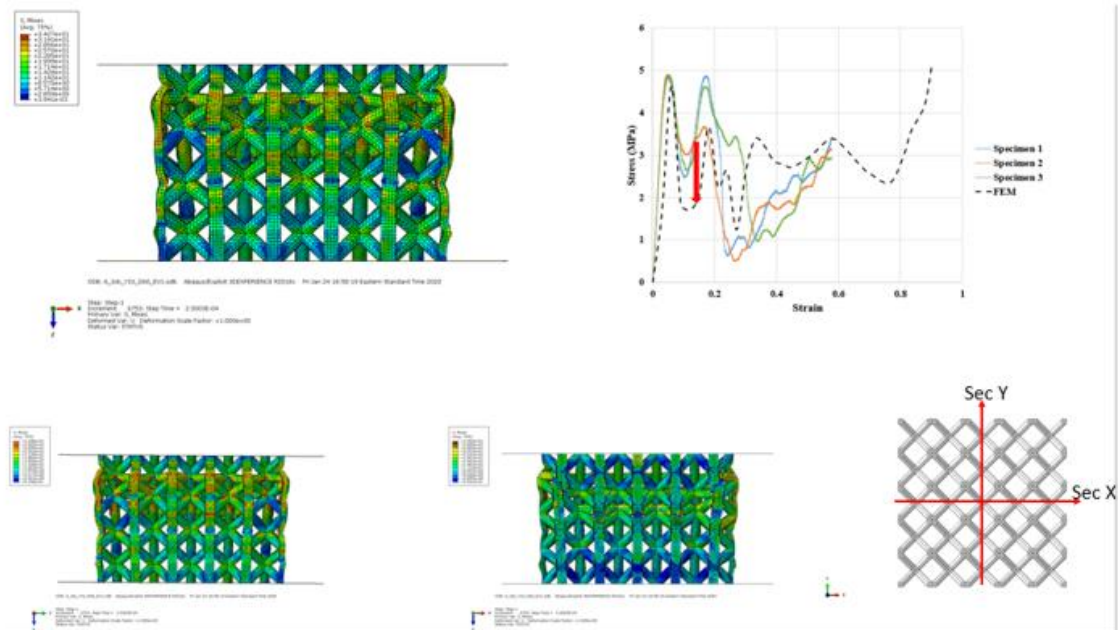


Figure 5.5 BCCV stage(3) with (a) Side view (b) Location in the curve (c) Top plan (d) Section x ,and (e) Section y.

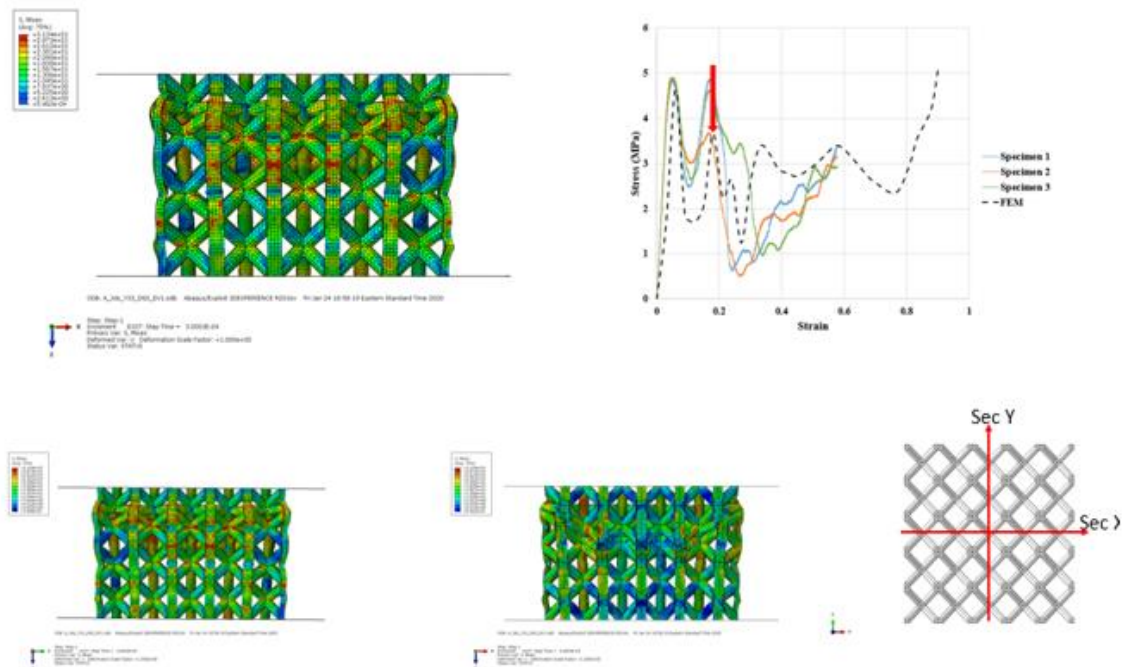


Figure 5.6 BCCV stage(4) with (a) Side view (b) Location in the curve (c) Top plan (d) Section x ,and (e) Section y.

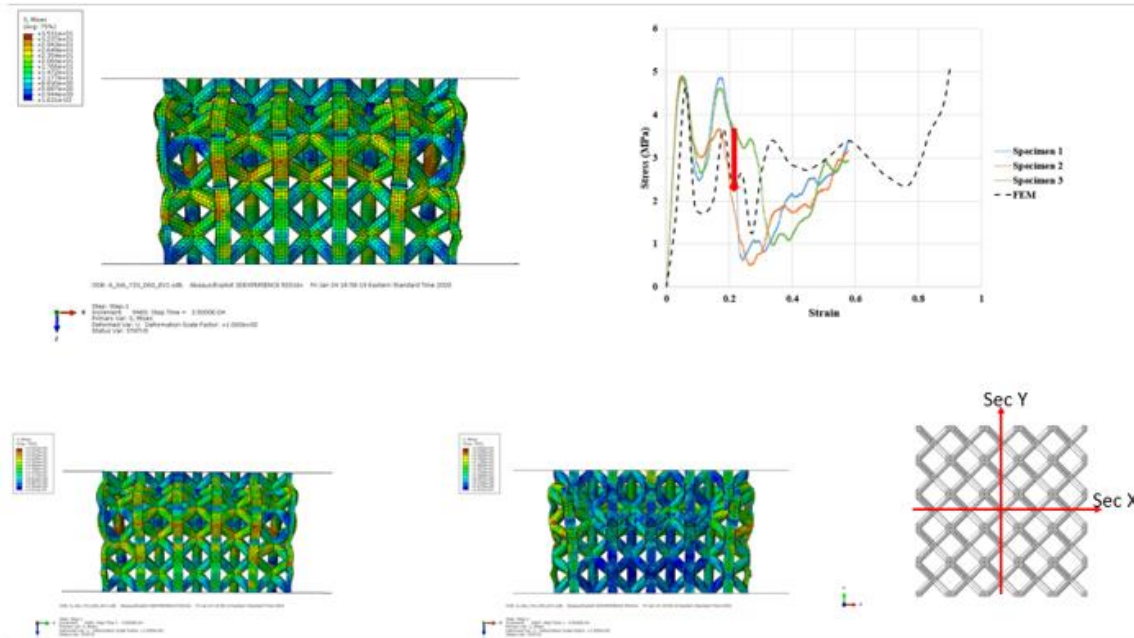


Figure 5.7 BCCV stage(5) with (a) Side view (b) Location in the curve (c) Top plan (d) Section x ,and (e) Section y.

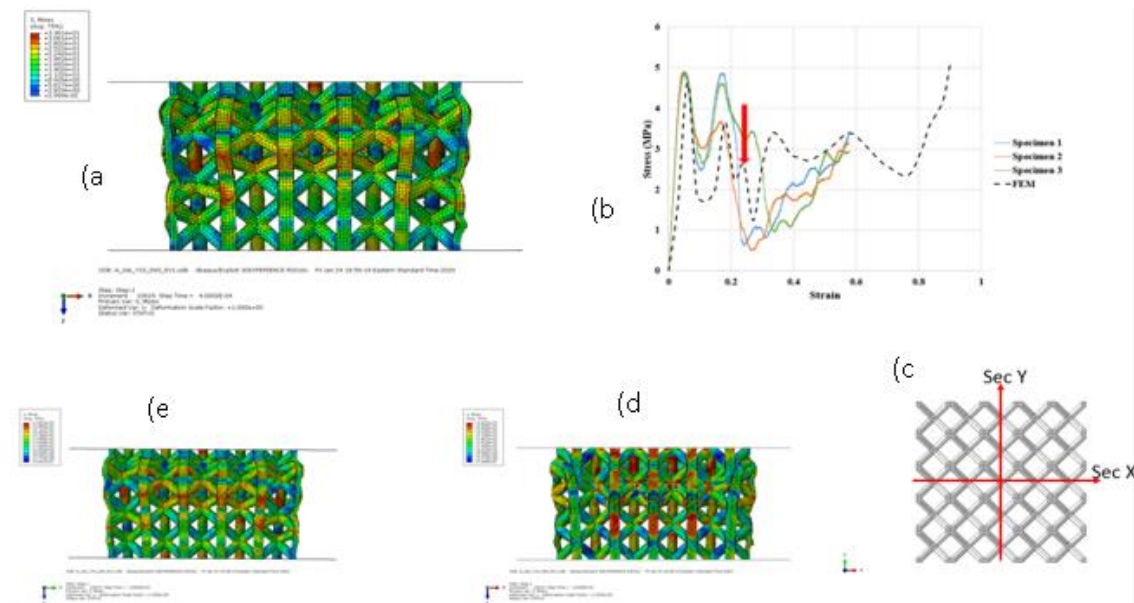


Figure 5.8 BCCV stage(6) with (a) Side view (b) Location in the curve (c) Top plan (d) Section x ,and (e) Section y.

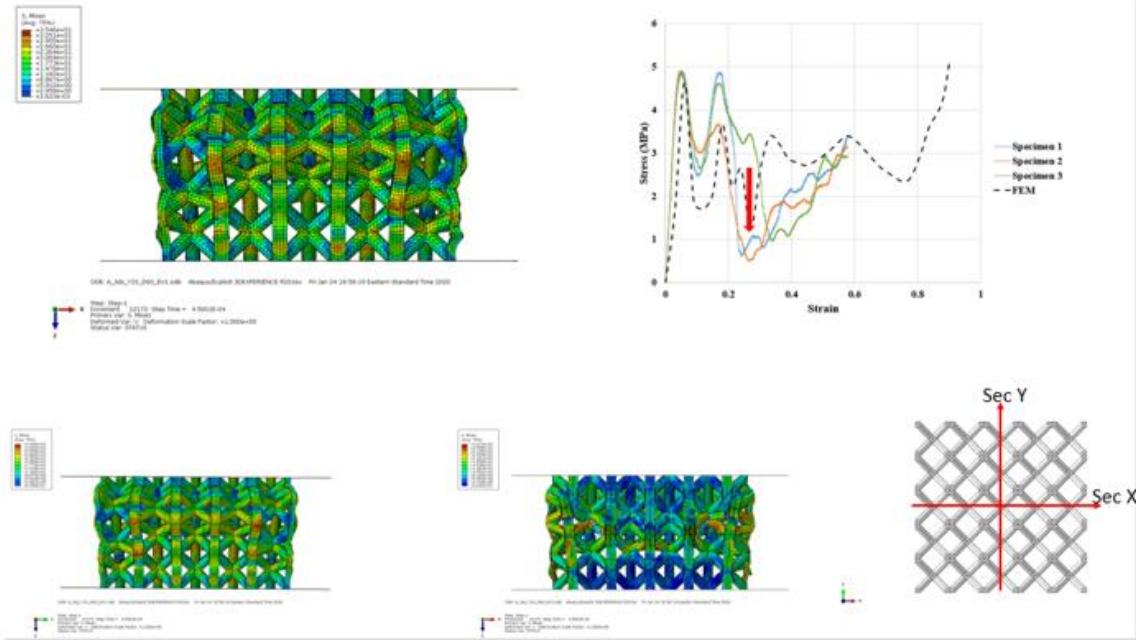


Figure 5.9 BCCV stage(7) with (a) Side view (b) Location in the curve (c) Top plan (d) Section x ,and (e) Section y.

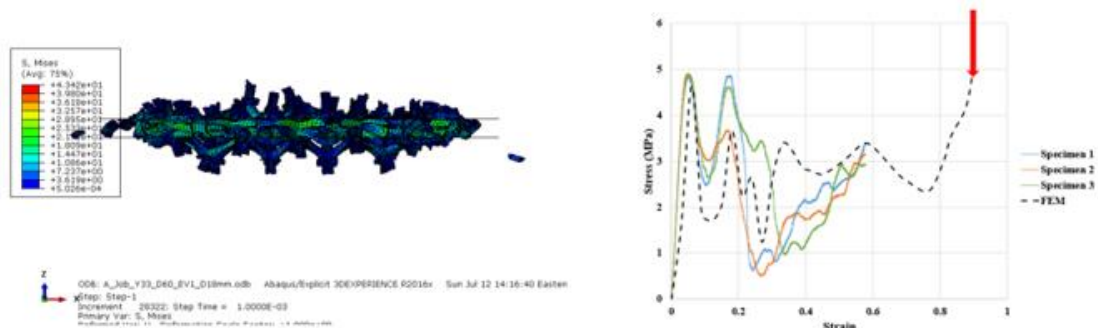


Figure 5.10 BCCV stage(9) with (a) Side view , and (b) Location in the curve

5.4 Progressive Damage Analysis for TetH

For the TetH configuration, two types of layers are defined. The first layer is for the horizontal struts, which are denoted as HSL1 to HSL3. The second set of layers are denoted as L1 to L4 for tetra layers (Figure 5.11). In this regard, it has been observed that L2 is opposite to L1 and L4 is opposite to L3. For the xz and yz planes, they were designated section x and section y respectively, also shown in Figure 5.12. For stage 1, the

linear elastic behavior is observed until the strain of 0.03 with corresponding stress of 4.548 MPa before starting the plastic plateau stage as shown in Figure 5.12. After that, stage 2 starts which is at the strain of 0.06 and corresponding stress of 5.133 MPa. At this stage, the maximum stress is observed at the internal sides of the struts as shown in section x and section y of Figure 5.13. This is because the extreme stresses. Fatal deformation occurs in the struts and the failure happens at the joints between the horizontal struts and the tetra struts as shown in the stage 3. For stage 3, the abrupt failure starts due to the fracture of the horizontal struts and the corresponding strain reaches 0.18 and the stress drops down to 2.643 MPa as shown in Figure 5.14. For the other stages, the strut will deform and continue resisting elastically and plastically until the strain densification happens in the final stage as shown in Figure 5.15.

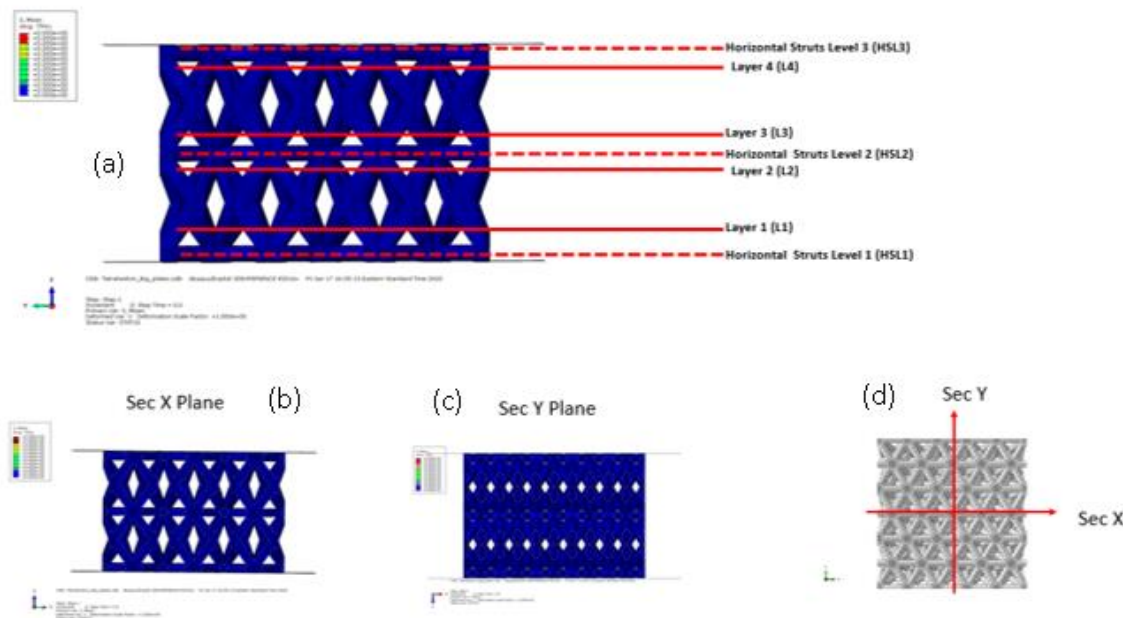


Figure 5.11 Tetrahedron initial stage with (a) Side view (b) Location in the curve (c) Top plan (d) Section x ,and (e) Section y.

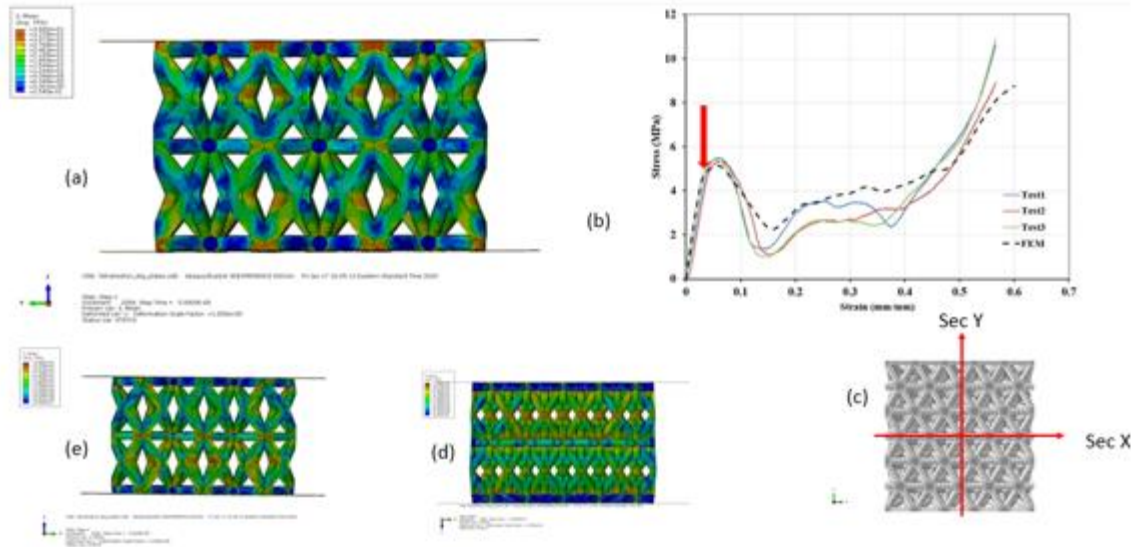


Figure 5.12 Tetrahedron stage(1) with (a) Side view (b) Location in the curve (c) Top plan (d) Section x ,and (e) Section y.

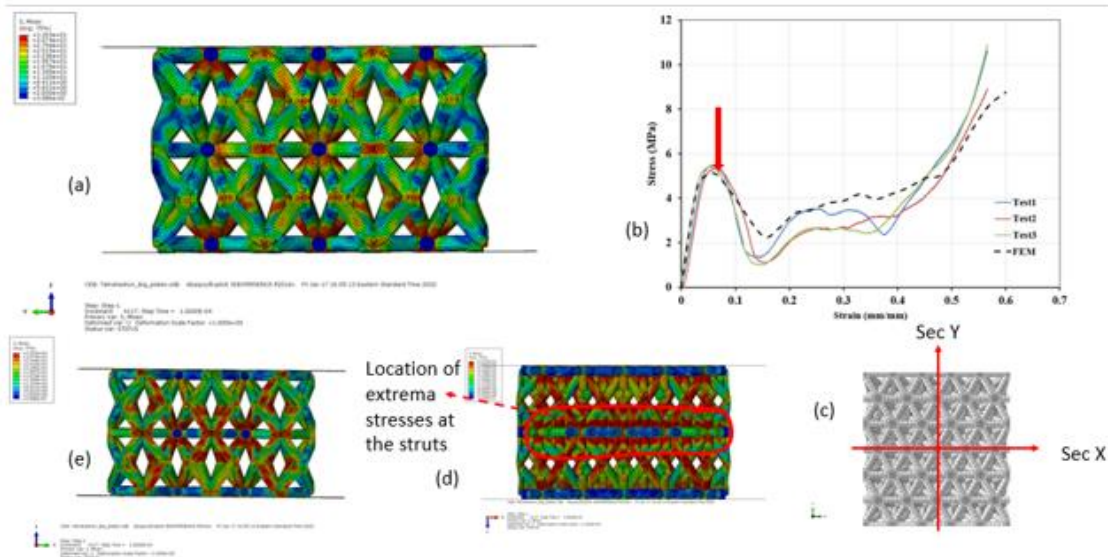


Figure 5.13 Tetrahedron stage(2) with (a) Side view (b) Location in the curve (c) Top plan (d) Section x ,and (e) Section y.

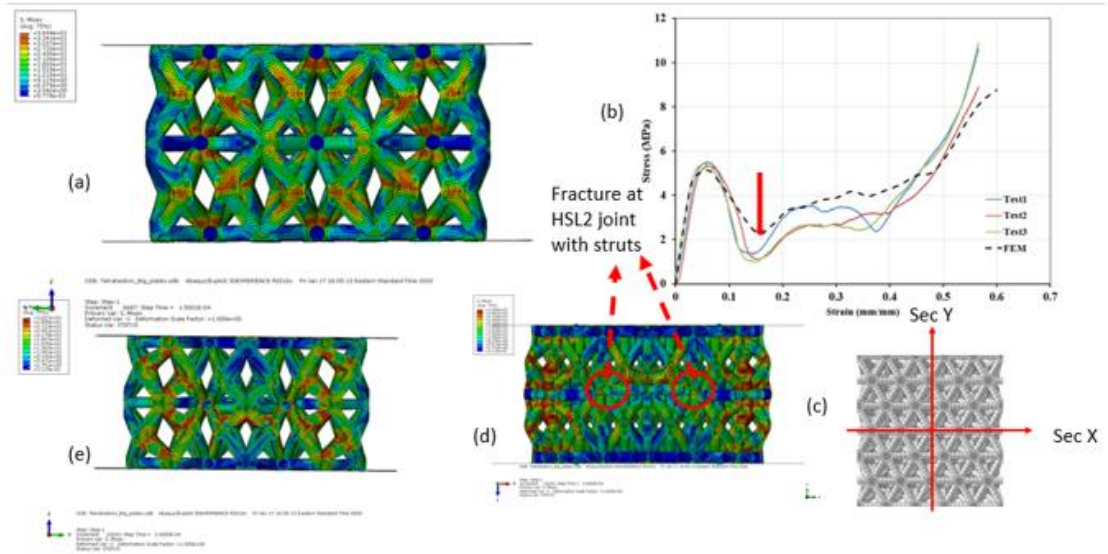


Figure 5.14 Tetrahedron stage(3) with (a) Side view (b) Location in the curve (c) Top plan (d) Section x ,and (e) Section y.

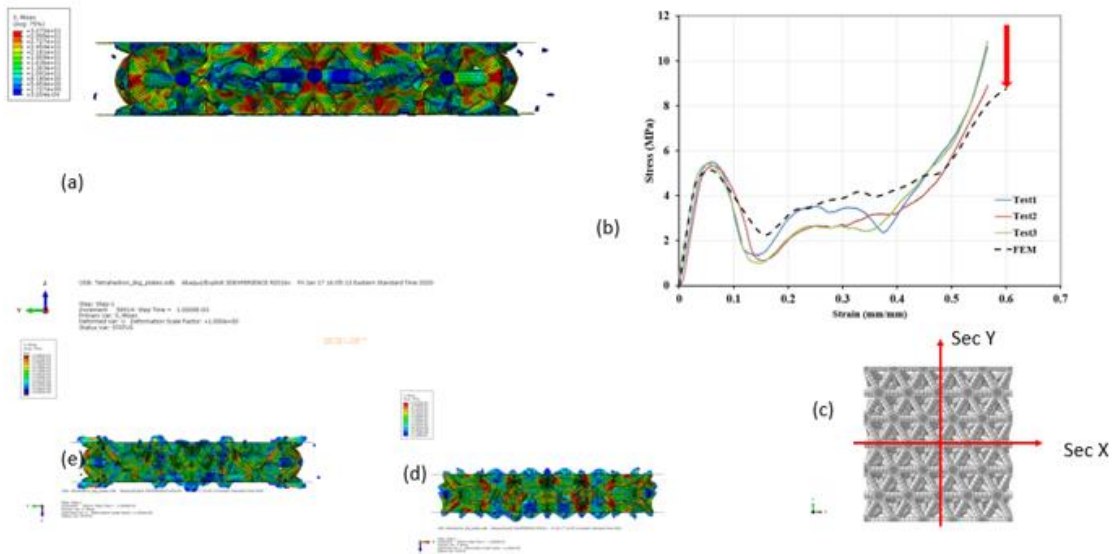


Figure 5.15 Tetrahedron stage(4) with (a) Side view (b) Location in the curve (c) Top plan (d) Section x ,and (e) Section y.

5.5 The Plateau Stages Validation for The BCCV and Tetrahedron

Even though the models were validated with experimental work as shown in previous chapters, they still needed to be validated based in the fracture stages. New

samples for both the configuration, BCCV and Tetrahedron and tested at specific strain values. The strain was applied based on the location of the plateau changing. For example, for the BCCV, it was selected the locations of the strains of 0.09 for first plateau and the strain of 0.26 for the second plateau. According to both the finite element models and the experimental picture at the strain of 0.09, it was noticed that all the vertical struts have collapsed and the configuration rests only on the regular struts as shown in the Figure 5.17. At a strain of 0.26, it was noticed that both the finite model and the experimental have shown collapsed in the layers L4 and L3 to result in the significant decrease in applied load which corresponded to the stresses as shown in the Figure 5.18. For the other configuration, the Tetrahedron, the first plateau was chosen at the strain of 0.06, and at this stage all the horizontal struts where damaged as shown in the Figure 5.19. The second plateau was chosen at the location of the strain of 0.36 where the regular struts have started to collapse as shown in the Figure 5.20.

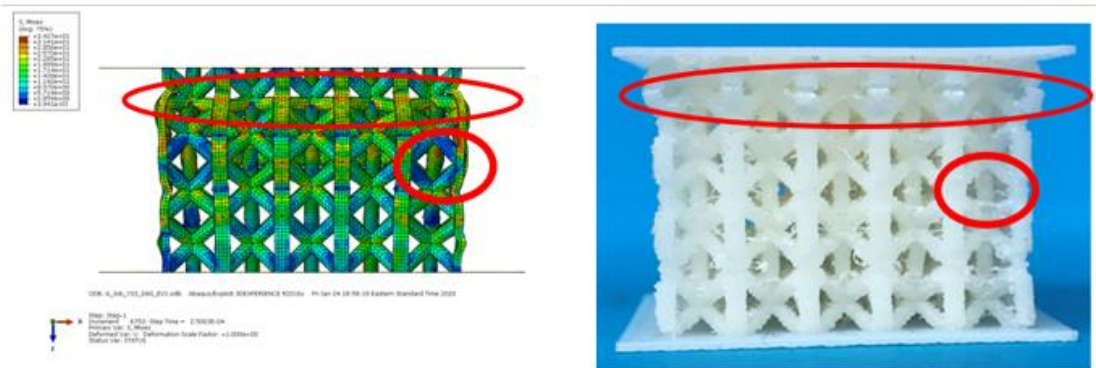


Figure 5.16 The BCCV Plateau progressive FEM vs Experimental at strain of 0.06

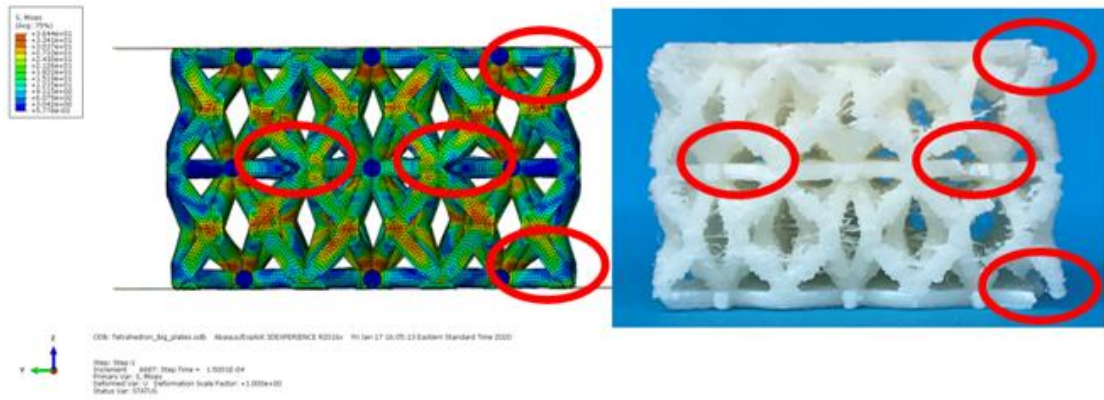


Figure 5.17 The Tetrahedron Plateau progressive FEM vs Experimental at strain of 0.06

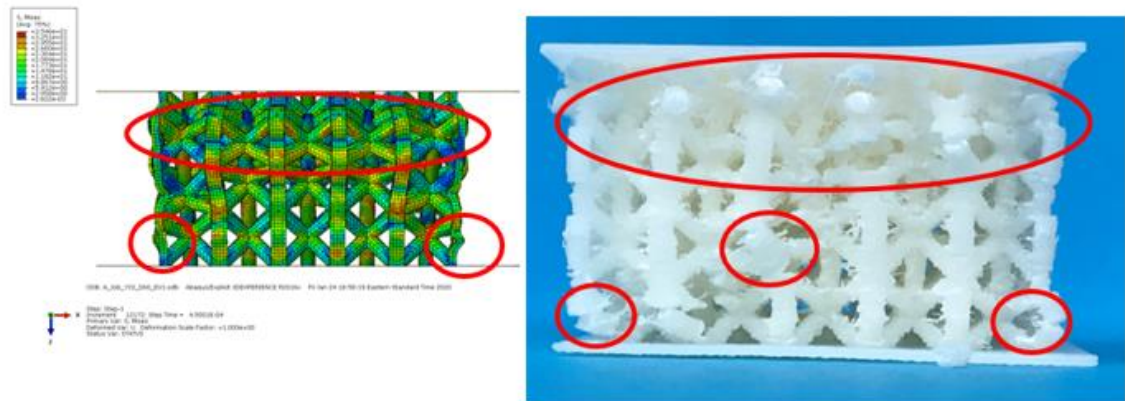


Figure 5.18 The BCCV Plateau progressive FEM vs Experimental at strain of 0.26

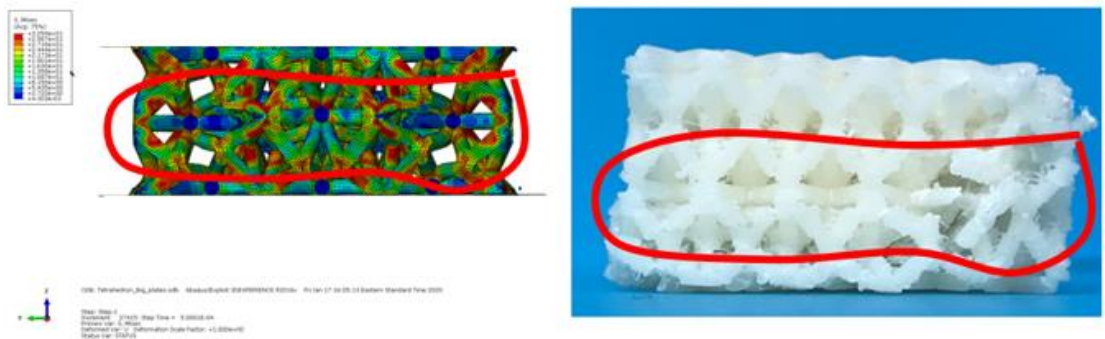


Figure 5.19 The Tetrahedron Plateau progressive FEM vs Experimental at strain of 0.36

5.6 Evaluation of Plateau Stress, Absorbed Energy, and Efficiency

The plateau stress and absorbed energy is essentially used to evaluate the configuration design [127]. To identify the useful absorbed energy, the Plateau stress and the efficiency must be determined. The absorbed energy can be defined as the area under the stress strain curve and it can be calculated from equation 5.1, whereas the efficiency is the ratio between the absorbed energy and the ideal energy absorbed with ideal peak stress and it can be found from equation 5.2. The end of plateau stress is to be theoretically at the same location of the maximum efficiency. Typically, the plateau stress can be found by dividing the energy absorbed by the length of the plateau regime. Thus, it will be dealt with the initial crash strain ε_y until the strain of the end of the plateau ε_{cd} , equation 5.3 will be used to compute the Plateau stress. For example, with the BCCV configuration, according to the Figure 5.21(a), the maximum efficiency was captured at the strain of 0.567 which corresponds to the end of the plateau at 0.856 MPa and from the Figure 5.21(b) and according to the plateau of 0.856 MPa the maximum absorbed energy is 0.3478 J/mm³. Similarly, for both of the TetH lattices Figure 5.22 (a) and (b). shows the plots of the stress-strain with the efficiency and the peak stress with the energy absorbed. Table (2) shows the values of the parameter discussed here for the three configurations.

$$W = \int_0^{\varepsilon} \sigma(\varepsilon) d\varepsilon \quad 5.1$$

$$E = \frac{\int_0^{\varepsilon} \sigma(\varepsilon) d\varepsilon}{\sigma_p * 1} \quad 5.2$$

Where σ_p is the peak stress at the interval strain ε .

$$\sigma_{pl} = \frac{\int_{\varepsilon_y}^{\varepsilon_{cd}} \sigma(\varepsilon) d\varepsilon}{\varepsilon_{cd} - \varepsilon_y} \quad 5.3$$

Table 5.1 The Plastic plateau parameters and energy absorption for the ABS lattice configurations.

LCS	Plateau Stress σ_{pl} (Mpa)	At the end of The Plateau region			
		Strain ϵ_{cd}	Stress σ (MPa)	Energy absorbed W (J/mm ³)	Max Efficiency E (%)
BCCV	2.828	0.877	4.6	2.41	52.2
TetH	3.696	0.4389	5.021	1.589	31

When evaluate the configurations based on the Plateau stress and maximum absorbed energy, we come up with different types of lattice performance. It is noticed that the BCCV has shown the highest absorbed energy of 2.41 J/mm³. Additionally, the efficiency of the BCCV is the highest which is about 52.2%. This is because of the fact that the BCCV has lower stress oscillating compared to the other configurations. The low absorbed energy is due to that the plateau stress for the BCCV is very low compared to other configurations. Both TetH and BCCV are considered Stretch dominated based on Ashby models as previously mentioned, this is the reason for the highest energy absorbed and higher plateau captured as shown in Table 5.1. The BCCV configuration has the highest efficiency due to the limited fluctuation of the peak stresses. It shows progressive damage, whereas the TetH and Pyr configurations have lower efficiency and therefore an abrupt failure and damage.

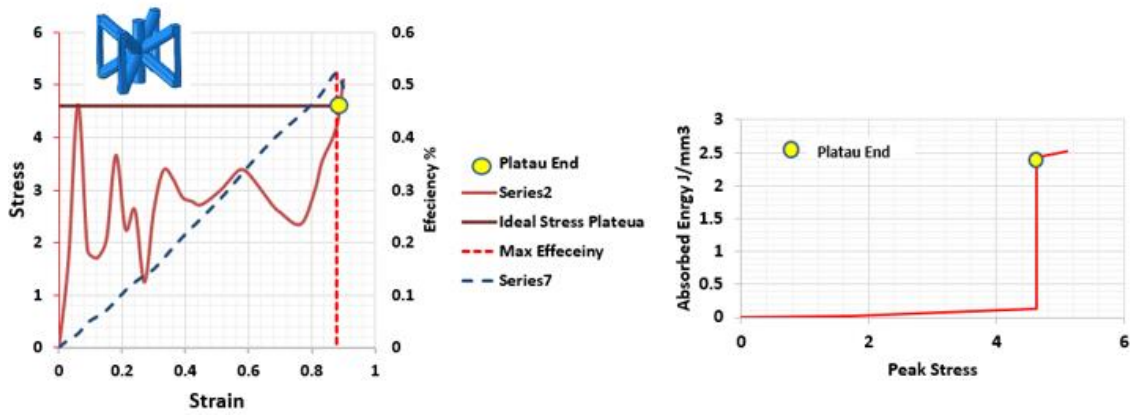


Figure 5.20 identifying the Plateau parameters for BCCV (a) Stress-strain and efficiency, and (b) Peak stress vs Absorb energy W

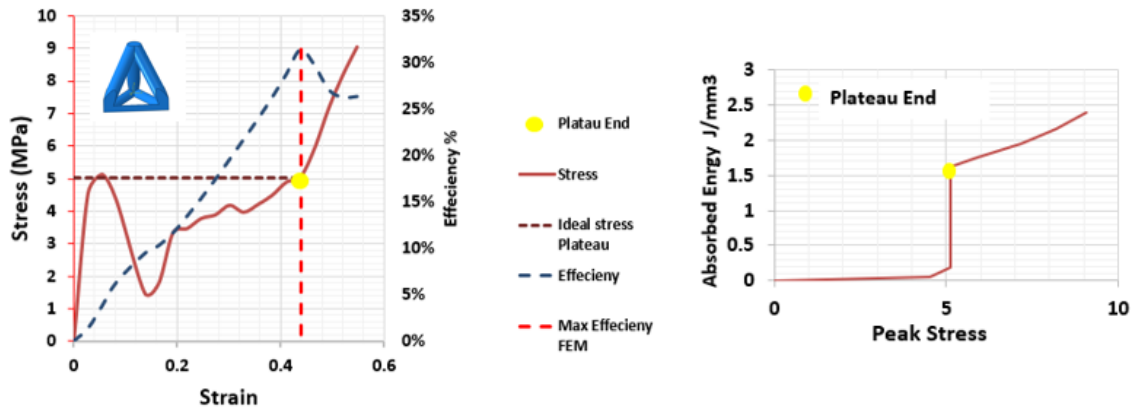


Figure 5.21 identifying the Plateau parameters for TetH (a) Stress-strain and efficiency, and (b) Peak stress vs Absorb energy W

5.7 Summary

The FEA models have shown good agreement with the experimental data in the elastic modulus, peak points, and the curve trends. It is clear that every configuration has provided different progressive damage trends and different mechanical criteria such as elastic modulus, plastic plateau, stiffness and peaks. This is due to many factors, including the topologies and the relative density ratios as discussed earlier. Although the BCCV configuration has shown multiple progressive damages, the lowest peak loads were captured because they tend to be more bending-dominated and have lower relative density ratios. The Ashby and Gibson models highly influence the lattice configurations. Both the BCCV and TetH are Stretch dominated having the highest stiffness and strength.

Chapter 6. Summery and Future Work

This research is motivated by the higher demand of sandwich materials development. The lattice structure geometry has direct impact on the mechanical behavior of the lattice configurations. For these reasons, many studies have been conducted to determine the influence of the lattice geometry on the mechanical behavior. In terms of studying and optimizing the lattice structure for more configurations, many researchers have attempted to develop finite element models for the lattice structure configurations. However, there is a lack of finite models for ABS printed materials due to many factors such as brittle behaviors. The previous studies were focused only on metallic printed materials. They only used beam element B3 for the entire lattice, or just one-unit cell for the ABS materials. Therefore, this study set out to determine an efficient finite element model for the polymetric materials to capture the entire elastic plastic behaviors for nonlinear mechanical responses and predict the fracture mechanisms.

This research has introduced the most appropriate methodologies for the finite element techniques for the printed lattice structures made of ABS materials. In chapter 2, the research has revealed how to develop the finite element model for the elastic stage of the lattice structure. Due to geometric challenges, the research was started in SolidWorks to create the lattice geometry. The SolidWorks Associative Interface tool was used to transfer the models to ABAQUS. However, this model was unable to capture beyond the plasticity stages. Because of this reason, the research has struggled to find creative techniques to overcome these problems as introduced in chapter 3. Chapter 3 addressed how to develop the nonlinear models for the lattice structures. For this reason and according to the finite elements books, we had to use elements with higher degrees of freedom and higher formulation order to capture the post-yield stages. Consequently, it has been thought to use the brick elements to develop this model. However, applying the brick elements in ABAQUS is restricted with many constraints as was mentioned in section 1.2.4.3. For this point, geometric decomposition must be done to the configuration in order for it to be meshable with hexahedral elements. Eventually, this procedure becomes too difficult and tedious to be done manually. Thus, an ABAQUS plugin coded in Python for finite element models was developed as stated in chapter 3. In chapter 3, we discussed how to integrate Python programming with ABAQUS via a graphical user interface (GUI). This tool was developed to perform all the complex tasks such as creating the geometry, geometry decomposition, face recognitions, body recognitions, joins, feature patterns (linear and polar), rotation translation, and adjustments, creating the material library, assigning the materials, and creating the jobs to be ready for the submission. Therefore, we created the tool Lattice Structure Designer (LSD tool). In chapter 4, the structures created with this

tool were validated with the experimental results. For all the six configurations, the tool shows good agreement with the experimental results. In chapter 5, we chose two of the most feasible configurations made with ABS material. The study focused on the progressive damage and evaluated based on both the Gibson and Ashby models and another analysis criterion which was the efficiency of absorption energy. In general, this research has provided many beneficial contributions as will be stated in next section.

6.1 The Research Contributions

This dissertation has provided several contributions in the area of 3D printing, and FEM models for; Compression tests, Impact test, Post-yielding stages, as well as developing new efficient ABAQUS /Python plug-in software (LSD tool).

- The LSD tool is new finite element tool for designing lattice structures. This tool provides a simple interface for defining lattice structures based on parameters of configuration type and unit cell dimensions, and cells distributions. This tool set up to generate 6 types of the lattice structures and it is possible to add more configurations. LSD tool is promising to be beneficial for the lattice structure engineering and designing not only for ABS polymer material but also for any other possible printed materials.
- The finite element models for lattice structure under compression were based on quasi-static tests. Results have shown that the mechanical properties of LCS depends on the topologies more than the materials. This contribution can help to reduce the volume of the printed component and therefore save more time and cost in manufacturing.

- This dissertation has provided a good understanding of the finite element model formulation especially for 3D printed materials. The models were developed for 6 types of complicated geometrical designs. Hence, analyzing and decomposing the geometries to apply the hexahedron elements is critical. The dissertation has provided an essential methodology on how to deal with any complex geometry and capture the post-yielding stages during stress testing.
- Another contribution of this dissertation is based on the validations presented in Chapters 2, 4, and 5. The models are efficient and show great agreement to real life results. Instead of printing material and fabricating the sample, it is now possible to predict the sample behaviors and estimate the costs without manufacturing and testing it.
- The final contribution of this dissertation is the investigation and validation of the progressive fracture mechanism for two types of lattice configurations, BCCV and Tetrahedron configurations. According to our research, these configurations have shown stretch dominant behaviors due to the horizontal and vertical struts. Because of this fact, they can absorb more energy. The absorbed energy and efficiency analyses have revealed the fact that the Ashby model's prediction about stretch-dominated configurations absorbing more energy than the bending-dominated ones but with lower efficiency due to abrupt failure is correct. Accordingly, the efficient stress plateau and maximum energy must be taken into account in terms of achieving optimal and comfortable sandwich material design. The Gibson-Ashby model can be useful to understand the mechanisms of the failure. However, the finite element simulation can help to

capture the failure stages and can provide deeper insight into the progressive failure process.

6.2 Future Work

Despite the research achievements, some of the works are still recommended for the future studies. These will be useful for 3D printed lattice structures. Some of these recommendations can be summarized in the following points.

- In chapter 2, the finite element models for the impact test was developed for the plasticity limits. Future work will develop an efficient Plug-in tool similar to the chapter 3 methodology for the impact test. The main aim of this model is to capture the fracture mechanism due to the impact load and the net absorbed energy from the dent depth for different LCS topologies.
- In chapters 3 and 4, the research has involved with developing the finite element models for the compression tests due to the quasi static conditions. For this reason, it is possible to expand the model to do more analysis such as thermal, vibration and acoustic energies, flow analysis and shear analysis. Much current research is conducted with these analyses to obtain higher quality results and more efficient lattice structure designs [22, 5, 72].
- Also in chapter 4, the research was conducted with 6 types of the lattice structures. Now, by using the same methodology it is possible to develop the models for more useful and feasible configurations such as FCC, BCCXYZ, FCCZ, FCC2 [3, 70].

- Even though the tool is good enough to create an efficient finite element model in combination with ABAQUS, an independent program can be developed in future work. Due to the power of ABAQUS to create efficient finite element models, the LSD tool was designed to work under ABAQUS environments. However, an independent software can be developed by using computer programming such as C++, C#, Java, etc.
- Future work will also develop the models for the taper struts and graded lattice structure. These models will be refined to increase the lattice configurations ability to improve energy absorption and the strength with less material [3, 22, 98].
- The model will also be reworked to expand the analysis of mechanical properties in different directions. Because the lattice structure can be orthotropic, it is recommended to study the mechanical behaviors in other orientations.
- Finally, because of the fact that LCS may be useful in many applications such as biomedical and aerospace [128, 129, 130], these sectors are rapidly growing due to many reasons. These applications usually involve fatigue loads due to repetitive work. For these reasons, future work will investigate the lattice configurations under fatigue conditions experimentally and computationally based on these applications.

References

- [1] R. Mines, S. Tsopanos, E. Shen, S. McKown, W. Cantwell, W. Brooks and C. Sutcliffe, "On the performance of micro lattice structures as core materials in sandwich panels subject to low velocity impact," Department of Engineering, The Quadrangle, University of Liverpool, Liverpool, UK, 2009.
- [2] C. A. M. D. P. Ling, "Mechanical behaviour of additively-manufactured polymeric octet-truss lattice structures under quasi-static and dynamic compressive loading," *Materials and Design*, vol. 162, no. November, pp. 106-118, 2019.
- [3] D. S. Al-Saedi, S. H. Masood, M. Faizan-Ur-Rab , A. Alomarah and P. Ponnusamy, "Mechanical properties and energy absorption capability of functionally graded F2BCC lattice fabricated by SLM," *Materials and Design*, vol. 144, pp. 32-44, 2018.
- [4] J. Wieding , A. Jonitz and R. Bader , "The Effect of Structural Design on Mechanical Properties and Cellular Response of Additive Manufactured Titanium Scaffolds," *materials*, pp. 1336-1347, 2012.
- [5] S. M. Ahmadi, S. A. Yavari, R. Wauthle, J. Schrooten, H. Weinans and A. A. Zadpoor, "Additively Manufactured Open-Cell Porous Biomaterials Made from Six Different Space-Filling Unit Cells: The Mechanical and Morphological Properties," *materials*, no. C, pp. 1871-1896, 2015.
- [6] B. Castanie´, C. Bouvet, Y. Aminanda, J.-J. Barrau and P. Thevenet, "Modelling of low-energy/low-velocity impact on Nomex honeycomb sandwich structures with metallic skins," *International Journal of Impact Engineering*, vol. 35, no. 7, pp. 620-634, 2008.

- [7] M. F. Ashby, *Material Selection in Mechanical design*, Burlington: Elsevier Ltd, 2011.
- [8] L. Gibson and M. Ashby, *Cellular Solids*, New York: The Press Syndicate of the university of Cambridge, 2001.
- [9] G. Gupta, J. Tan and C. . C. Seepersad, "Design And Freeform Fabrication Of Compliant Cellular Materials With Graded Stiffness," The University of Texas at Austin, Austin, 2015.
- [10] I. Hakim, "Non-destructive evaluation measurements and fracture effects in carbon/epoxy laminates containing porosity," *University of Dayton (PhD Dissertation)*, 2017.
- [11] A. Kamaloo, S. Emami, and H. Nuranian, "Enhancing Mechanical Strength of Inorganic Geopolymer Using Phenol Resin," *International Journal of Engineering*, vol. 4, no. 2, pp. 325-328, 2012.
- [12] S. Emami, "Development of Probabilistic Models for Long Term Reliability of Sandwich Composites in Saline Freeze/Thaw Environment for Civil Engineering Applications," *Phd Dissertation, University of Dayton*, 2017.
- [13] M. Mazur, M. Leary, S. Sun, M. Vcelka and D. Shidid, "Deformation and failure behaviour of Ti-6Al-4V lattice structures manufactured by selective laser melting (SLM)," *The International Journal of Advanced Manufacturing Technology*, pp. 1391-1411, 2016.
- [14] . L. B. Hussain and I. A. Hakim, "Recycling and formulation of aluminum scrap via mass balance die casting and forming," *Materials and Manufacturing Processes*, vol. 22, no. 7, pp. 916-921, 2007.
- [15] S. David, M. Norbert, H. Issa and E. Uwe, "Defect Recognition in CFRP Components Using Various NDT Methods within a Smart Manufacturing Process," *AIP Conference Proceedings*, vol. 1949, no. 1, p. 020024, 2018.

- [16] D. Klosterman, C. Browning, I. Hakim and K. Lach, "Investigation of various techniques for controlled void formation in fiberglass/epoxy composites," *Journal of Composite Materials*, vol. 55, no. 4, pp. 489-506, 2021.
- [17] I. Hakim, D. Schumacher, V. Sundar, S. Donaldson, A. Creuz, R. Schneider, J. Keller, C. Browning, D. May, M. Abo Ras and N. Meyendorf, "Volume imaging NDE and serial sectioning of carbon fiber composites," *AIP Conference Proceedings*, vol. 1949, no. 1, p. 120003, 2018.
- [18] S. A. Galehdari, M. Kadkhodayan and S. Hadidi-Moud, "Low velocity impact and quasi-static in-plane loading on a graded honeycomb structure; experimental, analytical and numerical study," *Aerospace Science and Technology*, vol. 47, pp. 425-433, 2015.
- [19] M. Wong, I. Owen, C. J. Sutcliffe and A. Puri, "Convective heat transfer and pressure losses across novel heat sinks fabricated by Selective Laser Melting," *International Journal of Heat and Mass Transfer*, vol. 52, no. 1-2, pp. 281-288, 2009.
- [20] H. Abdulhadi, "Designing New Generations of Bcc Lattice Structures and Developing Scaling Laws to Predict Compressive Mechanical Characteristics and Geometrical Parameters," *PhD dissertation, Wright State University, Dayton, Ohio*, 2020.
- [21] T. Alwattar, "Developing Equivalent Solid Model for Lattice Cell Structures Using Numerical Approaches," *PhD dissertation, Wright State University, Dayton, Ohio*, 2020.
- [22] H. Abdulhadi and A. Mian, "Effect of strut length and orientation on elastic mechanical response of modified body-centered cubic lattice structures," *Proceedings of the Institution of Mechanical Engineers, Part L: Journal of Materials: Design and Applications*, vol. 223, no. 11, pp. 2219-2233, 2019.

- [23] T. Alwattar and T. Mian, "Development of an Elastic Material Model for BCC Lattice Cell Structures Using Finite Element Analysis and Neural Networks Approaches," *Journal of composites science*, vol. 3, no. 4, p. 33, 2019.
- [24] J. Wieding, A. Wolf and R. Bader , "Numerical optimization of open-porous bone scaffold structures to match the elastic properties of human cortical bone," *Journal of the Mechanical Behavior of Biomedical Materials*, vol. 37, pp. 56-68, 2014.
- [25] M. Al Rifaie, A. Mian, P. Katiyar, P. Majumdar and R. Srinivasan, "Drop-Weight Impact Behavior of Three-Dimensional Printed Polymer Lattice Structures with Spatially Distributed Vertical Struts," *Journal of Dynamic Behavior of Materials*, vol. 5, no. 4, pp. 387-395, 2019.
- [26] J. Wang and B. V. Sankar, "Fracture toughness of cellular materials using finite element based micromechanics," *Journal of Chemical Information and Modeling*, vol. 53, no. 9, pp. 1689-1699, 2013.
- [27] C. Yan, . L. Hao, A. Hussein and P. Young, "Ti – 6Al – 4V triply periodic minimal surface structures for bone implants fabricated via selective laser melting," *Journal of the Mechanical Behavior of Biomedical Materials*, vol. 51, pp. 61-73, 2015.
- [28] X. Zhang, X. Gu, J. Lv, Z. Zhu and X. Zou, "Numerical analysis of the rheological behaviors of basalt fiber reinforced asphalt mortar using ABAQUS," *Construction and Building Materials*, vol. 157, pp. 392-401, 2017.
- [29] T. Alwattar and A. Mian, "Developing an Equivalent Solid Material Model for BCC Lattice Cell Structures Involving Vertical and Horizontal Struts," *Journal of composites science*, vol. 4, no. 6, p. 74, 2020.
- [30] A. Mian, A. Hamad, S. Longstreth, A. Archacki, R. Aga, C. Bartsch and E. Heckman, "The effects of printed lattice cell structure superstrates on printed patch antennas," *International journal of RF and microwave computer-aided engineering* , no. 3, pp. 1-11, 2021.

- [31] X. Zhang, X. Jin, G. Xie and H. Yan, "Thermo-Fluidic Comparison between Sandwich Panels with Tetrahedral Lattice Cores Fabricated," *energies*, 2017.
- [32] M. Smith, W. J. Cantwell, Z. Guan, S. Tsopanos, M. D. Theobald, G. N. Nurick and G. S. Langdon, "The quasi-static and blast response of steel lattice structures," *Journal of Sandwich Structures and Materials*, vol. 13, pp. 479-501, 2011.
- [33] I. Ullah, J. Elambasseril, M. Brandt and S. Feih, "Performance of bio-inspired Kagome truss core structures under compression and shear loading," *COMPOSITE STRUCTURE*, vol. 118, pp. 294-302, 2014.
- [34] I. Ullah, M. Brandt and S. Feih, "Failure and energy absorption characteristics of advanced 3D truss core structures," *Materials and Design*, vol. 92, pp. 937-948, 2016.
- [35] G. W. Kooistra, D. . T. Queheillalt and H. N. Wadley, "Shear behavior of aluminum lattice truss sandwich panel structures," *Materials Science and Engineering*, vol. 472, pp. 242-250, 2008.
- [36] O. Cansizoglu, O. Harrysson, D. Cormier, H. West and T. Mahale, "Properties of Ti-6Al-4V non-stochastic lattice structures fabricated via electron beam melting," *Materials Science and Engineering A*, vol. 492, no. 1-2, pp. 468-474, 2008.
- [37] E. Cetin and C. Baykaso, "International Journal of Mechanical Sciences Energy absorption of thin-walled tubes enhanced by lattice structures," *International Journal of Mechanical Sciences*, vol. 158, pp. 471-484, 2019.
- [38] P. F. Egan, V. C. Gonella, M. Engensperger, S. J. Ferguson and K. Shea, "Computationally designed lattices with tuned properties for tissue engineering using 3D printing," *PLoS ONE*, vol. 12, pp. 1-20, 2017.
- [39] L. J. Gibson and M. F. Ashby, *Cellular solids: Structure and properties*, Cambridge, New York: Cambridge University Press, 1997.

- [40] R. Gümürük, S. Karadeniz and R. Mines, "Static mechanical behaviours of stainless steel micro-lattice structures under different loading conditions," *Materials Science and Engineering A*, vol. 586, pp. 392-406, 2013.
- [41] M. R. Karamooz and M. Kadkhodaei, "A Computationally Efficient Modeling Approach for Predicting Mechanical Behavior of Cellular Lattice Structures," *Journal of Materials Engineering and Performance*, vol. 24, p. 245–252, 2015.
- [42] J. Kadkhodapour, H. Montazerian and S. Raeisi, "Investigating internal architecture effect in plastic deformation and failure for TPMS-based scaffolds using simulation methods and experimental procedure," *Materials Science & Engineering C*, vol. 43, pp. 587-597, 2014.
- [43] S. L. Sing, J. An, W. Y. Yeong and F. E. Wiria, "Laser and electron-beam powder-bed additive manufacturing of metallic implants: A review on processes, materials and designs," *Journal of Orthopaedic Research*, vol. 34, no. 3, pp. 369-385, 2016.
- [44] M. Mazur, M. Leary, S. Sun, M. Vcelka, D. Shidid and M. Brandt, "Deformation and failure behaviour of Ti-6Al-4V lattice structures manufactured by selective laser melting (SLM)," *International Journal of Advanced Manufacturing Technology*, vol. 84, no. 5-8, pp. 1391-1411, 2016.
- [45] S. McKown, Y. Shen, W. K. Brookes, C. J. Sutcliffe, W. J. Cantwell, G. S. Langdon, G. N. Nurick and M. D. Theobald, "The quasi-static and blast loading response of lattice structures," *International Journal of Impact Engineering*, vol. 35, no. 8, pp. 795-810, 2008.
- [46] C. Qiu, S. Yue, N. J. E. Adkins, M. Ward, H. Hassani, P. D. Lee, P. J. Withers and M. M. Attallah, "Materials Science & Engineering A Influence of processing conditions on strut structure and compressive properties of cellular lattice structures fabricated by selective laser melting," *Materials Science & Engineering A*, vol. 628, pp. 188-197, 2015.

- [47] B. Gorny, T. Niendorf, J. Lackmann, M. Thoene, T. Troester and H. J. Maier, "In situ characterization of the deformation and failure behavior of non-stochastic porous structures processed by selective laser melting," *Materials Science & Engineering A*, vol. 528, no. 27, pp. 7962-7967, 2011.
- [48] C. Beyer and D. Figueroa, "Design and Analysis of Lattice Structures for Additive Manufacturing," *Journal of Manufacturing Science and Engineering*, vol. 138, no. 12, p. 121014, 2016.
- [49] I. Maskery, N. T. Aboulkhair, A. O. Aremu, C. J. Tuck, I. A. Ashcroft, R. D. Wildman and R. J. M. Hague, "A mechanical property evaluation of graded density Al-Si10-Mg lattice structures manufactured by selective laser melting," *Materials Science and Engineering A*, vol. 670, pp. 264-274, 2016.
- [50] K. Ushijima, W. Cantwell, R. Mines, S. Tsopanos and M. Smith, "An investigation into the compressive properties of stainless steel micro-lattice structures," *Journal of Sandwich Structures and Materials*, vol. 13, no. 3, pp. 303-329, 2011.
- [51] S. D. Sangle, *Design And Testing Of Scalable 3d-Printed Cellular Structures Optimized For Energy Absorption*, Dayton: Wright State University, 2016.
- [52] M. J. Al Rifaie, *Resilience And Toughness Behavior Of 3d-Printed Polymer Lattice Structures: Testing And Modeling*, Dayton: Wright State University, 2017.
- [53] StrataSys, "Stratasys F123 Series Printers," StrataSys, 17 Feb 2019. [Online]. Available: <https://www.stratasys.com/3d-printers/f123>.
- [54] S. A. Yadlapati, *Influence Of FDM Build Parameters On Tensile And Compression Behaviors Of 3d Printed Polymer Lattice Structures*, Dayton: Wright State University, 2018.
- [55] K. Ravari, N. Esfahani, T. Andani, M. Kadkhodaei, A. Ghaei, H. Karaca and M. Elahinia, "On the effects of geometry, defects, and material asymmetry on the

- mechanical response of shape memory alloy cellular lattice structures," *Smart Materials and Structures*, vol. 25, p. 14, 2016.
- [56] M. K. Ravari, M. Kadkhodaei, M. Badrossamay and R. Rezaei, "Numerical investigation on mechanical properties of cellular lattice structures fabricated by fused deposition modeling," *International Journal of Mechanical Sciences*, vol. 88, pp. 154-161, 2014.
- [57] M. Smith, Z. Guan and W. J. Cantwell, "Finite element modelling of the compressive response of lattice structures manufacture using the selective laser melting technique," *International Journal of Mechanical Sciences*, vol. 67, pp. 28-41, 2013.
- [58] A. J. Turner, . M. Al Rifaie, A. Mian and R. Srinivasan, "Low-Velocity Impact Behavior of Sandwich Structures with Additively Manufactured Polymer Lattice Cores," *Journal of Materials Engineering and Performance*, vol. 27, no. 5, pp. 2505-2512, 2018.
- [59] W. D. Callister and D. G. Rethwisch, *Materials Science and Engineering*, Danvers,MA: John Wiley & Sons, Inc, 2014.
- [60] R. G. Budynas and J. K. Nisbett, *Shigley's Mechanical Engineering Design*, 9th ed., New York: McGraw-Hill, 2011.
- [61] I. Hakim, R. Laquai, D. Walter, B. Mueller, P. Graja and N. Meyendorf, "The effect of manufacturing conditions on discontinuity population and fatigue fracture behavior in carbon/epoxy composites," *AIP Conference Proceedings*, vol. 1806, no. 1, p. 090017, 2017.
- [62] S. Mohsenizadeh, R. Alipour, A. F. Nejad, M. S. Rad and Z. Ahmad, "Experimental investigation on energy absorption of auxetic foam filled thin-walled square tubes under quasi-static loading," *2nd International Materials, Industrial, and Manufacturing Engineering Conference, MIMEC2015,4-6 February 2015, Bali Indonesia*, vol. 2, pp. 331-336, 2015.

- [63] H. D. Carlton, J. Lind, M. C. Messner, N. A. Volkoff-Shoemaker, H. S. Barnard, N. R. Barton and M. Kumar, "Mapping local deformation behavior in single cell metal lattice structures," *Acta Materialia*, vol. 129, pp. 239-250, 2017.
- [64] N. Contuzzi, S. . L. Campanelli, C. Casavola and L. Lamberti, "Manufacturing and Characterization of 18Ni Marage 300 Lattice Components by Selective Laser Melting," *Materials*, vol. 6, pp. 3451-3468, 2013.
- [65] K. R. Jagtap, S. Y. Ghorpade and A. L. Singh, "Finite Element Simulation of Low Velocity Impact Damage in Composite Laminates," *Materials Today: Proceedings*, vol. 4, no. 2, pp. 2464-2469, 2017.
- [66] S. K. Hashemi and M. A. Bradford, "The strain-rate effects on the numerical simulation of steel beams under blast loads," *WIT Transactions on the Built Environment*, vol. 141, no. 1743-3509, pp. 311-322, 2014.
- [67] Y. Bao and T. Wierzbicki, "On fracture locus in the equivalent strain and stress triaxiality space," *International Journal of Mechanical Sciences*, vol. 46, no. 1, pp. 81-98, 2004.
- [68] X. Wang and J. Shi, "Validation of Johnson-Cook plasticity and damage model using impact experiment," *International Journal of Impact Engineering*, vol. 60, pp. 67-75, 2013.
- [69] H. Hooputra, H. Gese, H. Dell and H. Werner, "A comprehensive failure model for crashworthiness simulation of aluminium extrusions," *International Journal of Crashworthiness*, vol. 9:5, pp. 449-464, 2004.
- [70] K. G. R. V. G. Anoop Vasu, "A computational methodology for determining the optimum re-peening schedule to increase the fatigue life of laser peened aircraft components," *International Journal of Fatigue*, vol. 70, pp. 395-405, 2015.
- [71] K. Gobal, *High-Fidelity Multidisciplinary Sensitivity Analysis for Coupled Fluid-Solid Interaction Design (Dessertation)*, Dayton: Wright State Univerity, 2016.

- [72] J. David Deaton, *Design of Thermal Structures Using Topology Optimization (Dissertation)*, Dayton: WSU, 2014.
- [73] L. V. Sy, *Modeling Of Single Point Incremental Forming Process For Metal And Polymeric Sheet*, Padua, Italy: Department Of Innovation In Mechanics And Management at university of Padua, Italy, 2009.
- [74] A. K. Kayode, *Effects of Defects and Reverse Bending on Tensile Properties of Tensile Armour Wires*, Newcastle, UK: University of Newcastle, 2011.
- [75] A. A. Saeid, *Modeling The Progressive Damage In Biomimetic Composite Sandwich T-Joints*, Dayton: University of Dayton, 2016.
- [76] A. Saeid and S. Donaldson, "Experimental and finite element evaluations of debonding in composite sandwich structure with core thickness variations," *Advances in Mechanical Engineering*, vol. 8, no. 9, p. 1687814016667418, 2016.
- [77] A. Saeid and S. Donaldson, "Experimental and finite element investigations of damage resistance in biomimetic composite sandwich T-joints," *Materials*, vol. 9, no. 7, p. 510, 2016.
- [78] Simulia, *ABAQUS 2016 Solidworks Associative Interface User's Guide*, Dassault System, 2016.
- [79] J. F. Shepherd and C. R. Johnson, "Hexahedral mesh generation constraints," *Engineering with Computers*, vol. 24, no. 3, pp. 195-213, 2008.
- [80] Simulia, "Simulia Abaqus Documentation 2016," Simulia, 18 March 2018. [Online]. Available: <http://localhost:2080/v2016/>. [Accessed 2016].
- [81] E. S. Benzley, E. Perry, K. Merkley and B. Clark, "A Comparison of All Hexagonal and All Tetrahedral Finite Element Meshes for Elastic and Elasto-plastic Analysis," Brigham Young University, Provo, Utah, 1995.

- [82] R. D. Cook, D. S. Malkus, M. E. Plesha and R. J. Witt, Concepts and applications of finite element analysis, Hoboken: John Wiley, 2002.
- [83] B. L. d. Oliveira and J. Sundnes, "Comparison Of Tetrahedral And Hexahedral Meshes For Finite Element Simulation Of Cardiac Electro-Mechanics," *VII European Congress on Computational Methods in Applied Sciences and Engineering*, pp. 5-10, 2016.
- [84] S. Yamakawa and K. Shimada, "Fully-automated hex-dominant mesh generation with directionality control via packing rectangular solid cells," *International Journal For Numerical Methods In Engineering*, vol. 57, p. 2099–2129, 2003.
- [85] J. Cantrell, S. Rohde, D. Damiani, R. Gurnani, L. DiSandro, J. Anton, A. Young, A. Jerez, D. Steinbach, C. Kroese and P. Ifju, "Experimental Characterization of the Mechanical Properties of 3D-Printed ABS and Polycarbonate Parts," *Rapid Prototyping Journal*, vol. 23, no. 4, pp. 811-824, 2016.
- [86] R. Zou, Y. Xia, S. Liu, P. Hu, W. Hou, Q. Hu and C. Shan, "Isotropic and anisotropic elasticity and yielding of 3D printed material," *Composites Part B*, vol. 99, pp. 506-513, 2016.
- [87] W. Wu, P. Geng, G. Li, D. Zhao, H. Zhang and J. Zhao, "Influence of Layer Thickness and Raster Angle on the Mechanical Properties of 3D-Printed PEEK and a Comparative Mechanical Study between PEEK and ABS," *Materials*, vol. 8, pp. 5834-5846, 2015.
- [88] J. J. Laureto and J. M. Pearce, "Anisotropic mechanical property variance between ASTM D638-14 type i and type iv fused filament fabricated specimens," *Polymer Testing*, vol. 68, pp. 294-301, 2018.
- [89] A. Fadeel, A. Mian, M. Al Refaie and R. Srinivasan, "Effect of Vertical Strut Arrangements on Compression Characteristics of 3D Printed Polymer Lattice Structures: Experimental and Computational Study," *Journal of Materials Engineering and Performance*, vol. 1, pp. 1-8, 2018.

- [90] F. P. Beer, E. R. Johnston, J. DeWolf and D. Mazurek, *Mechanics of material*, New York: McGraw-Hill, 2012.
- [91] A. C. Ugural and S. K. Fenster, *Advanced Mechanics of Materials and Applied Elasticity*, Boston: Pearson Education, Inc., 2011.
- [92] T. L. Anderson, *Fracture mechanics Fundamentals and Applications*, Boca Raton, FL: Taylor & Francis Group, 2005.
- [93] J. A. Harris, R. E. Winter and G. J. McShane, "Impact response of additively manufactured metallic hybrid lattice materials," *International Journal of Impact Engineering*, vol. 104, pp. 177-191, 2017.
- [94] M. Rezvani and A. Jahan, "Effect of initiator, design, and material on crashworthiness performance of thin-walled cylindrical tubes: A primary multi-criteria analysis in lightweight design," *Thin-Walled Structures*, vol. 96, pp. 169-182, 2015.
- [95] K. Matlack, A. Bauhofer, S. Krodel, A. Palermo and C. Daraio, "Composite 3D-Printed metastructures for low frequency and broadband vibration absorption," *PNAS*, vol. 113, pp. 8386-8390, 2016.
- [96] K. Ushijima, W. Cantwell and D. Chen, "Prediction of Mechanical properties of Micro-Lattice structure subjected to multi-axial loading," *International Journal of Mechanical Science*, vol. 68, pp. 47-55, 2013.
- [97] C. Hammett, R. Rinaldi and F. Zok, "Pyramidal Lattice Structure for High Strength and Energy Absorption.," *Journal of Applied Mechanics*, vol. 80, 2013.
- [98] M. Avallè, G. Belingardi and A. Ibba, "Mechanical models of cellular solids: Parameters identification from experimental tests," *International Journal of Impact Engineering*, vol. 34, no. 1, pp. 3-27, 2007.
- [99] P. Köhnen, C. Haase, J. Bültmann, S. Ziegler, H. J. Schleifenbaum and W. Bleck, "Mechanical properties and deformation behavior of additively manufactured

- lattice structures of stainless steel," *Materials and Design*, vol. 145, pp. 205-217, 2018.
- [100] I. Maskery, A. Hussey, A. Panesar, A. Aremu, C. Tuck, I. Ashcroft and R. Hague, "An investigation into reinforced and functionally graded lattice structures," *Journal of Cellular Plastics*, vol. 52, no. 2, pp. 151-165, 2017.
- [101] N. Fleck, *Metal Foams : a Design Guide Metal Foams : A Design Guide*, Madras-India: Butterworth-Heinemann, 2016.
- [102] J. Besson, "Continuum models of ductile fracture: A review," *International Journal of Damage Mechanics*, vol. 19, no. 1, pp. 3-52, 2010.
- [103] I. Hakim, S. Donaldson, N. Meyendorf and C. Browning, "Porosity effects on interlaminar fracture behavior in carbon fiber-reinforced polymer composites," *Materials Sciences and Applications*, vol. 8, no. 02, p. 170, 2017.
- [104] S. Adam and K. N. Premnath, "Numerical investigation of the cascaded central moment lattice Boltzmann method for non-Newtonian fluid flows," *Journal of Non-Newtonian Fluid Mechanics*, vol. 274, no. October, p. 104188, 2019.
- [105] Y. H. Gedik, H. Nakamura, Y. Yamamoto and M. Kunieda, "Evaluation of three-dimensional effects in short deep beams using a rigid-body-spring-model," *Cement and Concrete Composites*, vol. 33, no. 9, pp. 978-991, 2011.
- [106] H. K. Man and J. G. Van Mier, "Damage distribution and size effect in numerical concrete from lattice analyses," *Cement and Concrete Composites*, vol. 33, no. 9, pp. 867-880, 2011.
- [107] F. Schlangen and E. J. Garboczi, "Fracture simulations of concrete using lattice models: computational aspects," *Engineering Fracture Mechanics*, vol. 57, no. 2-3, pp. 319-332, 1997.

- [108] R. Hasana, R. Mines and P. Fox, "Characterization of selectively Laser Melted Ti-6Al-4V Micro-Lattice Struts," *Procedia Engineering*, vol. 10, pp. 536-541, 2011.
- [109] A. Fadeel, A. Hasanain, S. Raghavan and M. Ahsan, "A Computational Approach in Understanding the Low-Velocity Impact Behavior and Damage of 3D-Printed Polymer Lattice Structures," *Journal of Materials Engineering and Performance*, 2021.
- [110] ASTM, "Standard Test Method for Tensile Properties of Plastics," ASTM INTERNATIONAL, 10 August 2018. [Online]. Available: <https://www.astm.org/Standards/D638.htm>. [Accessed 25 May 2018].
- [111] B. Pavan Venkata Naga Sai, D. C. K. Agarapu and A. Eluru, "Assay of moment resisting precast and monolithic frames using ABAQUS software," *Materials Today: Proceedings*, p. XXX in press, 2020.
- [112] T. Kartheek and T. V. Das, "3D Modelling and analysis of encased steel-concrete composite column using abaqus," *Materials Today: Proceedings*, vol. 27, pp. 1545-1554, 2020.
- [113] G. S. da Silva, L. E. Kostascki and I. Iturrioz, "Analysis of the failure process by using the Lattice Discrete Element Method in the Abaqus environment," *Theoretical and Applied Fracture Mechanics*, vol. 107, no. October 2019, p. 102563, 2020.
- [114] X. Huang, Z. Bie, L. Wang, Y. Jin, G. Su and X. He, "Finite element method of bond-based peridynamics and its ABAQUS implementation," *Engineering Fracture Mechanics*, vol. 206, no. November 2018, pp. 408-426, 2019.
- [115] Simulia, *Micromechanics Plugin For Abaqus/CAE*, Dassault Systems, 2016.
- [116] H. Petter, *A Primer on Scientific Programming with Python*, Oslo: University of Oslo, 2014.

- [117] G. Puri, "Python Scripts for Abaqus," Simulia, 2011.
- [118] A. Jenab, I. Sari Sarraf, D. E. Green, T. Rahmaan and M. J. Worswick, "The Use of genetic algorithm and neural network to predict rate-dependent tensile flow behaviour of AA5182-sheets," *Materials and Design*, vol. 94, pp. 262-273, 2016.
- [119] H. Fangohr, Introduction to Python for Computational Science and Engineering, Southampton, England: Faculty of Engineering and the Environment University of Southampton, 2015.
- [120] M. Nesládek and M. Španiel, "An Abaqus plugin for fatigue predictions," *Advances in Engineering Software*, vol. 103, pp. 1-11, 2017.
- [121] L. Távara, L. Moreno, E. Paloma and V. Mantič, "Accurate modelling of instabilities caused by multi-site interface-crack onset and propagation in composites using the sequentially linear analysis and Abaqus," *Composite Structures*, vol. 225, no. May, p. 110993, 2019.
- [122] iMechanica, "partitioning or selecting faces in ABAQUS using scripting techniques," iMechanica, 2 May 2016. [Online]. Available: <https://imechanica.org/node/15852>. [Accessed 21 July 2020].
- [123] Remy, "Abaqus: script to select elements on a surface," Stack OverFlow, 1 July 2019. [Online]. Available: <https://stackoverflow.com/questions/37048689/abaqus-script-to-select-elements-on-a-surface>. [Accessed 20 July 2020].
- [124] E. R. Denlinger and P. Michaleris, "Effect of stress relaxation on distortion in additive manufacturing process modeling," *Additive Manufacturing*, vol. 12, pp. 51-59, 2016.
- [125] T. Tancogne-dejean, C. Roth, U. Woy and D. Mohr, "Probabilistic fracture of Ti-6Al-4V made through additive layer manufacturing," *International Journal of Plasticity*, vol. 78, pp. 145-172, 2016.

- [126] J. Kadkhodapour, H. Montazerian, A. C. Darabi and A. P. Anaraki, "Failure mechanisms of additively manufactured porous biomaterials : Effects of porosity and type of unit cell," *Journal of the Mechanical Behavior of Biomedical Materials*, vol. 50, pp. 180-191, 2015.
- [127] F. N. Habib, . P. Iovenitti, S. H. Masood and M. Nikzad, "Fabrication of polymeric lattice structures for optimum energy absorption using Multi Jet Fusion technology," *Materials and Design*, vol. 155, pp. 86-98, 2018.
- [128] C. Pan, Y. Han and J. Lu, "Design and Optimization of Lattice Structures: A Review," *Applied science*, vol. 10(18), p. 6374, 2020.
- [129] S. K. Moon, Y. E. Tan, J. Hwang, J. Hwang and Y. J. Yoon, "Application of 3D printing technology for designing light-weight unmanned aerial vehicle wing structures," *International Journal of Precision Engineering and Manufacturing - Green Technology*, vol. 1, no. 3, pp. 223-228, 2014.
- [130] L. Magerramova, M. Volkov, A. Afonin, M. Svinareva and D. Kalinin, "Application of light lattice structures for gas turbine engine fan blades," *31st Congress of the International Council of the Aeronautical Sciences, ICAS 2018*, pp. 1-10, 2018.

Appendix A: Debugging The BCC with Geometric Decomposition

```
# -*- coding: mbc -*-  
from abaqus import*  
from abaqusConstants import*  
from part import *  
from material import *  
from section import *  
from assembly import *  
from step import *  
from interaction import *  
from load import *  
from mesh import *  
from optimization import *  
from job import *  
from sketch import *  
from visualization import *  
from connectorBehavior import *  
  
def createPart  
(X,Y,Z,R,NX,NY,NZ,SL,ZH,Material,Pyr_SL,NTZ,RadL,Pyr_Z,NPH,NPX,NPY,HFrame3,Com  
boBox1,Mat_Name,Den,Young,Poiss,Table):#X=X Dim , Y=Y_Dim, Z=Z_Dim , r is the strut  
radius  
  
    mdb.models['Model-1'].Part(dimensionality=THREE_D, name='Part-1', type=  
        DEFORMABLE_BODY)  
  
    M=mdb.models['Model-1']  
  
    P=M.parts['Part-1']  
  
    P.ReferencePoint(point=(0.0, 0.0, 0.0))  
  
    P.DatumPointByCoordinate(coords=(X, 0.0,
```

```

    0.0))
P.DatumPointByCoordinate(coords=(0.0, Y,
    0.0))
P.DatumPointByCoordinate(coords=(0.0, 0.0,
    Z))
P.DatumPointByCoordinate(coords=(X, Y,
    0.0))
P.DatumPointByCoordinate(coords=(X, 0.0,
    Z))
P.DatumPointByCoordinate(coords=(X, Y,
    Z))
P.DatumPointByCoordinate(coords=(0.0, Y,
    Z))
P.DatumAxisByTwoPoint(point1=
    P.referencePoints[1], point2=
    P.datums[7])
P.DatumAxisByTwoPoint(point1=
    P.datums[4], point2=
    P.datums[6])
P.DatumPlaneByPointNormal(normal=
    P.datums[9], point=
    P.datums[7])
M.ConstrainedSketch(gridSpacing=25.47, name='__profile__',
    sheetSize=1018.95, transform=
    P.MakeSketchTransform(
    sketchPlane=P.datums[11],
    sketchPlaneSide=SIDE1,
    sketchUpEdge=P.datums[10],
    sketchOrientation=RIGHT, origin=(X, Y, Z)))

```

```

P.projectReferencesOntoSketch(filter=
    COPLANAR_EDGES, sketch=M.sketches['__profile__'])
M.sketches['__profile__'].CircleByCenterPerimeter(center=(
    0.0, 0.0), point1=(R, 0.0))
P.SolidExtrude(depth=sqrt(X**2.+Y**2.+Z**2.),
    flipExtrudeDirection=ON, sketch=
    M.sketches['__profile__'], sketchOrientation=RIGHT,
    sketchPlane=P.datums[11],
    sketchPlaneSide=SIDE1, sketchUpEdge=
    P.datums[10])
del M.sketches['__profile__']
P.DatumPlaneByPrincipalPlane(offset=Z/2.,
    principalPlane=XYPLANE)
P.DatumPlaneByPrincipalPlane(offset=X/2.,
    principalPlane=YZPLANE)
P.DatumPlaneByPrincipalPlane(offset=Y/2.,
    principalPlane=XZPLANE)
P.Mirror(keepOriginal=ON, mirrorPlane=
    P.datums[14])
P.Mirror(keepOriginal=ON, mirrorPlane=
    P.datums[13])
P.DatumPlaneByOffset(flip=SIDE1, offset=8.0
    , plane=P.datums[13])
M.ConstrainedSketch(gridSpacing=25.47, name='__profile__',
    sheetSize=1018.95, transform=
    P.MakeSketchTransform(
    sketchPlane=P.datums[18],
    sketchPlaneSide=SIDE1,
    sketchUpEdge=P.datums[10],

```

```

        sketchOrientation=RIGHT, origin=(X/2., Y/2., 10.5)))
P.projectReferencesOntoSketch(filter=
        COPLANAR_EDGES, sketch=M.sketches['__profile__'])
M.sketches['__profile__'].rectangle(point1=(10, X/2.0)
        , point2=(-10, 10+Y/2.0))
M.sketches['__profile__'].rectangle(point1=(
        10, -X/2.0), point2=(-10,
        -10))
P.CutExtrude(flipExtrudeDirection=OFF,
        sketch=M.sketches['__profile__'], sketchOrientation=
        RIGHT, sketchPlane=P.datums[18],
        sketchPlaneSide=SIDE1, sketchUpEdge=
        P.datums[10])
del M.sketches['__profile__']
M.ConstrainedSketch(gridSpacing=0.89, name='__profile__',
        sheetSize=35.92, transform=
        P.MakeSketchTransform(
        sketchPlane=P.datums[18],
        sketchPlaneSide=SIDE1,
        sketchUpEdge=P.datums[10],
        sketchOrientation=RIGHT, origin=(X/2., Y/2., 10.5)))
P.projectReferencesOntoSketch(filter=
        COPLANAR_EDGES, sketch=M.sketches['__profile__'])
M.sketches['__profile__'].rectangle(point1=(-Y/2.0, 10),
        point2=(-10, -10))
M.sketches['__profile__'].rectangle(point1=(Y/2.0, 10),
        point2=(10, -10))
P.CutExtrude(flipExtrudeDirection=OFF,
        sketch=M.sketches['__profile__'], sketchOrientation=

```



```

        RIGHT, sketchPlane=P.datums[18],
        sketchPlaneSide=SIDE1, sketchUpEdge=
        P.datums[10])
del M.sketches['__profile__']
P.DatumAxisByTwoPoint(point1=
        P.datums[6], point2=
        P.datums[2])
P.DatumPlaneByOffset(flip=SIDE1, offset=8.0
        , plane=P.datums[14])
M.ConstrainedSketch(gridSpacing=0.95, name='__profile__',
        sheetSize=38.33, transform=
        P.MakeSketchTransform(
        sketchPlane=P.datums[22],
        sketchPlaneSide=SIDE1,
        sketchUpEdge=P.datums[21],
        sketchOrientation=RIGHT, origin=(10.5, Y/2., Z/2.)))
P.projectReferencesOntoSketch(filter=
        COPLANAR_EDGES, sketch=M.sketches['__profile__'])
M.sketches['__profile__'].rectangle(point1=(10, Z/2.0),
        point2=(-10, 10))
M.sketches['__profile__'].rectangle(point1=(10, -Z/2.0),
        point2=(-10, -10))
P.CutExtrude(flipExtrudeDirection=OFF,
        sketch=M.sketches['__profile__'], sketchOrientation=
        RIGHT, sketchPlane=P.datums[22],
        sketchPlaneSide=SIDE1, sketchUpEdge=
        P.datums[21])
del M.sketches['__profile__']
P.PartitionCellByDatumPlane(cells=

```

```

        P.cells.getSequenceFromMask(('[#1 ]',
        ), ), datumPlane=P.datums[14])
P.PartitionCellByDatumPlane(cells=
        P.cells.getSequenceFromMask(('[#3 ]',
        ), ), datumPlane=P.datums[15])
P.PartitionCellByDatumPlane(cells=
        P.cells.getSequenceFromMask(('[#f ]',
        ), ), datumPlane=P.datums[13])
P.PartitionCellByPlaneThreePoints(cells=
        P.cells.getSequenceFromMask(('[#ff ]',
        ), ), point1=P.datums[6], point2=
        P.datums[3], point3=
        P.datums[7])
P.PartitionCellByPlaneThreePoints(cells=
        P.cells.getSequenceFromMask(('[#fff ]',
        ), ), point1=P.datums[4], point2=
        P.datums[8], point3=
        P.datums[5])
P.PartitionCellByPlaneThreePoints(cells=
        P.cells.getSequenceFromMask((
        '[#ffff ]', ), ), point1=P.datums[4],
        point2=P.datums[7], point3=
        P.datums[5])
P.PartitionCellByPlaneThreePoints(cells=
        P.cells.getSequenceFromMask((
        '[#ffffff ]', ), ), point1=P.datums[6],
        point2=P.datums[8], point3=
        P.datums[3])
P.PartitionCellByPlaneThreePoints(cells=

```

```

        P.cells.getSequenceFromMask((
        ['#ffffff ], ), ), point1=
        P.vertices[37], point2=
        P.datums[7], point3=
        P.datums[8])
P.PartitionCellByPlaneThreePoints(cells=
        P.cells.getSequenceFromMask((
        ['#ffffff #ff ], ), ), point1=
        P.datums[4], point2=
        P.datums[3], point3=
        P.datums[5])
        ## For Partitions Here *****
if ComboBox1 == 'BCC':
    print('BCC')

```

Appendix B: Assigning the Ti-6Al-4V Alloy Debugging

```
elif Material=='Titanume Alloy (Ti-6AL-4V)':
    print 'Titanume Alloy (Ti-6AL-4V)'
    mdb.models['Model-1'].Material(name='Ti-6Al-4V')
    mdb.models['Model-1'].materials['Ti-6Al-4V'].Elastic(table=((104000.0,
0.35),
    ))
    mdb.models['Model-1'].materials['Ti-6Al-4V'].Plastic(table=((
    915.30261031580562, 0.0), (923.7823056199893,
0.0025252525252525255), (
    931.85801905960648, 0.0050505050505050509),
(939.56732324251197,
    0.007575757575757576), (946.94222001986213,
0.010101010101010102), (    0.22727272727272729),
(1192.2643610707344, 0.22979797979797981), (
    1193.5174046893969, 0.23232323232323235),
(1194.7578616535106,
    0.23484848484848486), (1195.9860073237644,
0.2373737373737374), (
    1197.2021088609936, 0.23989898989898992),
(1198.4064255114668,
    0.24242424242424243), (1199.5992088810019,
0.24494949494949497), (
    1200.7807031984069, 0.24747474747474749),
(1201.9511455687166, 0.25)))
    mdb.models['Model-1'].materials['Ti-6Al-4V'].Expansion(table=((8.6e-06,
), ))
    mdb.models['Model-1'].materials['Ti-6Al-4V'].Density(table=((4.429e-09,
), ))
    mdb.models['Model-1'].HomogeneousSolidSection(material='Ti-6Al-4V',
name=
```

```
        'Ti-6Al-4V', thickness=None)
mdb.models['Model-1'].HomogeneousSolidSection(material='Ti-6Al-4V',
name=
        'Ti-6Al-4V', thickness=None)
PP4.Set(cells=
        PP4.cells.getByBoundingBox(-50,-50,-50,50,50,50), name='Set-2')
PP4.SectionAssignment(offset=0.0,
        offsetField="", offsetType=MIDDLE_SURFACE, region=
        PP4.sets['Set-2'], sectionName=
        'Ti-6Al-4V', thicknessAssignment=FROM_SECTION)
```

Appendix C: Assigning Undefined Materials Debugging

```
elif Material=='Other Material (Need to be defiened)':  
    print Mat_Name  
    mdb.models['Model-1'].Material(name=Mat_Name)  
    mdb.models['Model-1'].materials[Mat_Name].Elastic(table=((Young,  
Poiss),  
    ))  
    mdb.models['Model-1'].materials[Mat_Name].Plastic(table=((Table)))  
    mdb.models['Model-  
1'].materials[Mat_Name].Density(table=((Den*1.1023113109244E-12, ), )) # convert the  
density kg/m3 to Ton/mm3  
    mdb.models['Model-1'].HomogeneousSolidSection(material=Mat_Name,  
name=  
    Mat_Name, thickness=None)  
    mdb.models['Model-1'].HomogeneousSolidSection(material=Mat_Name,  
name=  
    Mat_Name, thickness=None)  
    PP4.Set(cells=  
    PP4.cells.getByBoundingBox(-50,-50,-50,50,50,50), name='Set-2')  
    PP4.SectionAssignment(offset=0.0,  
    offsetField="", offsetType=MIDDLE_SURFACE, region=  
    PP4.sets['Set-2'], sectionName=  
    Mat_Name, thicknessAssignment=FROM_SECTION)
```

Appendix D: Assigning the Boundary Conditions

Set the BOUNDARY Conditions

#####

```
mdb.models['Model-1'].rootAssembly.Set(name='Set-3', referencePoints=(
    mdb.models['Model-1'].rootAssembly.instances['Part-3-
2'].referencePoints[2],
    ))
mdb.models['Model-1'].EncastreBC(createStepName='Initial', localCsys=None,
    name='Fixed', region=mdb.models['Model-1'].rootAssembly.sets['Set-3'])
mdb.models['Model-1'].SmoothStepAmplitude(data=((0.0, 0.0), (0.01, 1.0)),
name=
    'Amp-1', timeSpan=STEP)
mdb.models['Model-1'].rootAssembly.Set(name='Set-4', referencePoints=(
    mdb.models['Model-1'].rootAssembly.instances['Part-3-
1'].referencePoints[2],
    ))
FD=1
mdb.models['Model-1'].DisplacementBC(amplitude='Amp-1',
createStepName='Step-1'
    , distributionType=UNIFORM, fieldName="", fixed=OFF,
localCsys=None, name=
    'Movable_Plate', region=mdb.models['Model-1'].rootAssembly.sets['Set-
4'],
    u1=0.0, u2=0.0, u3=FD*0.5, ur1=0.0, ur2=0.0, ur3=0.0)
```

Appendix E: Assigning the Mesh

```
# ***** For Mesh only
*****

PP4.seedPart(deviationFactor=0.1,
             minSizeFactor=0.1, size=0.35)

PP4.setElementType(elemTypes=(ElemType(
    elemCode=C3D8R, elemLibrary=EXPLICIT,
secondOrderAccuracy=OFF,
    kinematicSplit=AVERAGE_STRAIN, hourglassControl=DEFAULT,
    distortionControl=DEFAULT), ElemType(elemCode=C3D6,
elemLibrary=EXPLICIT),
    ElemType(elemCode=C3D4, elemLibrary=EXPLICIT)), regions=(
    PP4.cells.getByBoundingBox(-50,-50,-50,50,50,50), ))

PP4.generateMesh()
```


Appendix F: Assigning the Job

```
# ***** For the job *****  
mdb.Job(activateLoadBalancing=False, atTime=None, contactPrint=OFF,  
description="", echoPrint=OFF, explicitPrecision=SINGLE, historyPrint=OFF,  
memory=90, memoryUnits=PERCENTAGE, model='Model-1', modelPrint=OFF,  
multiprocessingMode=DEFAULT, name='Job-e1', nodalOutputPrecision=SINGLE,  
numCpus=1, numDomains=1, parallelizationMethodExplicit=DOMAIN, queue=None,  
resultsFormat=ODB, scratch="", type=ANALYSIS, userSubroutine="", waitHours=  
0, waitMinutes=0)
```